VŠB TECHNICKÁ UNIVERZITA OSTRAVA | FAKULTA ELEKTROTECHNIKY A INFORMATIKY

CENTRUM DOPRAVNÍHO VÝZKUMU

AVISON (Analýza viditelnosti účastníků silničního provozu za účelem zvýšení jejich bezpečnosti za soumraku a v noci)

*je projektem soutěže VI - Bezpečnostní výzkum České republiky 2015-2022 (2015 - 2022) vyhlášeného MV0 - Ministerstvem vnitra (MV) s identifikačním číslem **VI20172019071** řešeným v období: 01.01.2017- 31.12.2019. Jeho hlavní příjemcem je Vysoká škola báňská - Technická univerzita Ostrava / Fakulta elektrotechniky a informatiky, dalším účastníkem projektu je Centrum dopravního výzkumu, v. v. i. v roli dalšího účastníka projektu.*

MINISTERSTVO VNITRA ČESKÉ REPUBLIKY

V Příloze č. 1 Smlouvy – Projekt, v části 5. 4. Vedlejší výsledky projektu:

DEFINICE DRUHŮ VÝSLEDKŮ

(Metodiky hodnocení výzkumných organizací a programů účelové podpory výzkumu, vývoje a inovací schválené usnesením vlády dne 8. února 2017 č. 107)

J_{imp} - recenzovaný odborný článek

Obsah:

VITÁSEK, J., J. JARGUS, T. STRATIL, J. LÁTAL and J. KOLÁŘ. Illumination and Communication Characteristics of White Light Created by Laser Excitation of YAG:Ce Phosphor Powders. Optical Materials. 2018, vol. 83, pp. 131-137. ISSN 0925-3467. DOI: 10.1016/j.optmat.2018.05.084.

LATAL, J., VITASEK, J., HAJEK, L., VANDERKA, A., MARTINEK, R. and V. VASINEK. Influence of simulated atmospheric effect combined with modulation formats on FSO systems. Optical Switching and Networking. 33 (2019). pp. 184–193. DOI: 10.1016/j.osn.2018.01.001.

BÍL, M., R. Andrášik, J. Sedoník. A detailed spatiotemporal analysis of traffic crash hotspots. Applied Geography 107 (2019), pp. 82–90. DOI: 10.1016/j.apgeog.2019.04.008.

VITASEK, J. T. STRATIL, J. LATAL J. KOLAR A Z. WILCEK. Indoor illumination imitating optical parameters of sunny summer daylight. Optics & Laser Technology, 124, April 2020, ISSN 0030-3992. DOI: 10.1016/j.optlastec.2019.105965.

Optical Materials 83 (2018) 131–137

Contents lists available at ScienceDirect

Optical Materials

journal homepage: www.elsevier.com/locate/optmat

Illumination and communication characteristics of white light created by laser excitation of YAG:Ce phosphor powders

Jan Vitasek*[,1], Jan Jargus, Tomas Stratil, Jan Latal, Jakub Kolar

Department of Telecommunications, Faculty of Electrical Engineering and Computer Science, VSB–Technical University of Ostrava, 17. listopadu 15, 708 33, Ostrava, Czech Republic

ARTICLE INFO

Keywords:
Correlated colour temperature
Laser light source
PDMS
VLC
White light
YAG:Ce

ABSTRACT

We tested four YAG:Ce phosphor powders to use for illumination and communication. The illumination and communication function could be put together and create a multifunctional light source. The Visible Light Communication (VLC) technology is based on this principle. The VLC will be engaged in 5G networks. The tested phosphor powders were mixed with Poly-Di-Methyl-Siloxane (PDMS) and hardened in a parabolic reflector. A blue laser diode was used for excitation of the phosphor powders. The measured illumination characteristics were colour coordinates *x* and *y* and Correlated Colour Temperature (CCT). The measured communication characteristics were rise time, fall time and photoluminescence decay time. The experimental results showed that one of the four phosphor powders can be used for illumination and communication purposes.

1. Introduction

A photoluminescence phosphor powder was a part of the first white Light Emitting Diode (LED) which was constructed in 1996 [1]. This type of white LEDs is labelled pc-LED (LED (phosphor converted LED). The base is a blue emitting chip (GaN, InGaN) and a layer of phosphor powder Yttrium Aluminium Garnet doped by Cerium ($Y^3Al^5O^{12}:Ce^{3+}$) [2–14]. A part of the blue light is spectrally converted in phosphor powder into yellow light, the rest of blue light creates with the converted yellow light a white light. The other type of the white LEDs are RGB-LEDs which are a compound of three colour chips (red, green and blue). Correct intensity setting of chips creates a white light. The pc-LEDs are cheaper and therefore more extended than the RGB-LEDs. The pc-LEDs began to gradually replace the traditional sources of white light (light bulbs and fluorescent tubes) thanks to their better technical properties. Generally, LEDs reach much higher efficiency, and their further improvements are expected. The other advantages of LEDs are their longer lifetime, higher tolerance to humidity, a smaller and compact size, minimum heat generation compared with the traditional illumination sources, and lower power consumption. LEDs are more ecological because they are mercury free [2–5].

The other advantage of LEDs is their possible use for communication purposes. LEDs can be switched on and off instantly in comparison to the traditional light bulbs and fluorescent tubes. Thanks to this feature white LEDs can be used in Visible Light Communication (VLC) technology. This technology merges two functions together, illumination and communication. The cost is a key factor today, therefore pc-LEDs are preferred. The disadvantage of pc-LEDs is a photoluminescence (PL) decay of converted light which limits the bit rate [2], [12–19]. There are several techniques how to eliminate the PL decay. The best known is using a colour filter which suppresses the yellow component of light (500 nm and more) [20–22]. This filter is placed on the receiver, so that the photodetector catches and processes only the blue light. The disadvantage of this technique is the requirement of the colour filter and also a power fall. The original power of the blue light is reduced to a half (and less) because a part of the blue light was converted in a phosphor powder into the yellow light, therefore the original blue light is considerably decreased. Another technique uses pre and post-equalization of data signal [23–27]. As has been mentioned above, LEDs can be modulated. Their modulation ability is much better than that of light bulbs and fluorescent tubes, but LEDs lag behind lasers. Improvement of modulation ability with regards to the power supply is solved by Bias-T, when the data (modulation) current is superimposed to supply forward current [28]. Another possibility is to use a laser excitation source instead of a LED excitation source.

Probably the world's best known combination of laser light and phosphor powders is BMW Laserlight Technology [29]. BMW constructed a car headlamp with a set of laser diodes and series of mirrors

* Corresponding author.
E-mail address: jan.vitasek@vsb.cz (J. Vitasek).
URL: http://optice.vsb.cz (J. Vitasek).
[1] 17. listopadu 15, 708 33 Ostrava, Czech Republic.

https://doi.org/10.1016/j.optmat.2018.05.084
Received 23 March 2018; Received in revised form 22 May 2018; Accepted 30 May 2018
Available online 14 June 2018
0925-3467/

located within the headlamp assembly, which reflects and focuses the light into a lens. The lens is filled with a yellow phosphor powder. Once the laser light is reflected into the lens, it interacts with the yellow phosphor powder, which in turn creates a bright, highly intense white light. Finally, this light is diffused to reduce its intensity and then reflected out of the front of the headlamp. The light is 10 times brighter than LED created light. The correlated colour temperature is between 5500 and 6000 K. BMW says that compared to traditional systems, Laserlight is about 30% more efficient, and since the lights can create bright light in a smaller housing. In comparison, a LED low beam covers 100 m, a LED high beam 300 m and a laser light beam 600 m. The described properties are very excellent, but major problem arises in case of a car accident. Because the laser light beam illumines a road at a long distance, the used laser diodes have to emit a high power. In the case of a car accident, the headlamp could be broken, laser beams could be tilted, and the high power lasers could injure a car crew or rescuers. Nevertheless, this system showed that it is possible to use a blue exciting laser diode and a phosphor powder for the creation of white light.

A similar headlamp named Matrix Laser Technology was also presented by Audi. Blue laser light is aimed at a set of individually adjustable micro mirrors. Reflected blue light goes through a phosphor element where white light is created. This white light then goes through a lens and illuminates a road [30].

The laser diodes are easily modulated and therefore can send data. The laser diode can also be used for white light creation. The car-to-car communication does not need high data rates for at present, but the same principle can be used for indoor communication. The power of emitted light does not have to be high because the light trace is short (units of meters) in comparison to the car headlamp. This intended use depends on illumination and communication characteristics of the used phosphor powder [31–36].

The following text deals with the laboratory testing of illumination and communication characteristics of white light created by blue laser light excitation of the phosphor powders. The next chapter generally describes the conversion of light in the phosphor powder. Chapter 3 explains the experimental arrangement. Chapter 4 shows the results of illumination characteristics measurements. The results of communication characteristics measurements are summarized in Chapter 5. Chapter 6 deals with the influence of concentration (amount) of phosphor powder on the illumination and communication characteristics. In chapter 6, only one phosphor powder was tested and its properties were found to be the best. It is usable for both mentioned functions at the same time. The last chapter concludes this article.

2. Photoluminescence in a phosphor powder

After correct light excitation, the electron transitions 5d-4f happen in YAG:Ce phosphor powders with large emission spectrum. The Ce^{3+} has a valence electron configuration of $4f^1$, which gives rise to the $^2F_{5/2}$and $^2F_{7/2}$ low-lying energy states. Consequently, the visible emission is a composite of two bands due to an electronic transition from the lowest lying 5d energy level down to the $^2F_{5/2}$ and $^2F_{7/2}$ states. Since the emission is due to an orbitally allowed 5d-4f electronic transition, it has a short radiative lifetime of ca. 20 ns The Ce^{3+} activator ions substitute some of the Y^{3+} ions which are coordinated by eight O^{2-} anions in the host lattice of YAG. The Ce^{3+} ions consequently occupy sites of D_2 point group symmetry and the resulting crystal field causes the energies of the 5d orbitals to be split. Five absorption bands at 204.6, 225.4, 261, 339.7 and 457.5 nm were observed in the absorption spectrum of YAG:Ce by Tomiki et al. [37] which were assigned to transitions from the $^2F_{5/2}$ ground state to each of the 5d levels [6–10]. YAG:Ce phosphors can contain together with yttrium Y also gadolinium Gd. The Gd^{3+} ions are larger than Y^{3+} which causes a red shift of the Ce^{3+} emission due to the increased crystal field that results from the decrease in a Ce-O distance that leads to a larger splitting of the 5d energy levels. Conversely, substitution of Al^{3+} ions for the larger Gd^{3+} ions on the octahedral sites gives a blue shift due to a weaker crystal field for the Ce^{3+} ions [38,39].

Table 1
Phosphor powders.

Phosphor powder	Chemical composition	Median particle sizes (μm)
QMK58/F-U1	$Y_3Al_5O_{12}:Ce^{3+}$	4.0
QMK58/F-U2	$Y_3Al_5O_{12}:Ce^{3+}$	3.5
QMK58/N-U6	$Y_3Al_5O_{12}:Ce^{3+}$	11.0
QUMK58/F-D1	$(Y,Gd)_3Al_5O_{12}::Ce^{3+}$	4.0

3. Experimental arrangement

The phosphor powder samples for our experiments were provided by Phosphor Technology Ltd. We used four types of YAG:Ce phosphor powders, their labels and properties are summarized in Table 1. This information was emailed.

3.1. Poly-Di-Methyl-Siloxane polymer

We used Poly-Di-Methyl-Siloxane (PDMS) named Sylgard 184 [40] as a carrier of the phosphor powders. The Sylgard 184 has two components, a PDMS base and a curing agent. Both these components are mechanically mixed in the weight ratio 10:1. During the mechanical mixing, some bubbles can appear. The bubbles can be removed by cooling in a refrigerator or in an ultrasonic bath or in both. The phosphor powders were added to the Sylgard 184 in weight ratio 1:35 for all phosphor samples. The mixture PDMS base-curing agent-phosphor was then put in the laboratory shaker for the uniform distribution of all components before the heat hardening. The heat hardening happens at a temperature of around 85 °C and it takes 30 min.

The PDMS is optically transparent from the near UV up to NIR region of the spectra [40]. Further, it is possible to shape the PDMS into any form and size which extends its use.

3.2. PDMS + phosphor powders in reflector

We also solved the problem of how to suitably connect the PDMS + phosphor powder with the blue laser diode. We used a reflector [41] for this purpose. At the output aperture of the reflector, there was a 2 mm layer of PDMS + phosphor powder, see Fig. 1. The procedure of preparation was as follows. The mixture of PDMS + phosphor powder was poured into the Petri dish and it created a uniform layer. After that, the reflector was put in the dish. The output aperture (wider) of the reflector was superimposed on the bottom of the Petri dish. The dish was then put in the furnace. After the heat hardening, the excess edges were removed. We repeated this procedure with all four phosphor powders.

3.3. Illumination characteristics measurements

We used the blue laser diode L450P1600 MM (Osram) [42] as a source of excitation. Peak wavelength 450 nm, FWHM 9.5 nm by forward current 800 mA, a threshold current 200 mA and beam divergence 23° respective 7°. The measurement was done in the continual supply mode. The Benchtop LD current controller LDC240C (Thorlabs) supplied the laser diode forward current from 200 mA to 800 mA with the

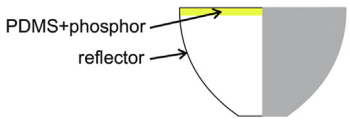

Fig. 1. PDMS + phosphor powder in reflector.

step of 200 mA. The total optical spectrum, colour coordinates x, y and CCT were recorded for each forward current. We used the spectrometer Avantes HS2048XL together with an integrating sphere for this measurement. The calibration was performed using a tungsten halogen light source. The problem of using the laser diode for illumination purposes is a narrow beam of laser. Therefore, we put a glass diffuser (Edmund Optics 43–725) between the laser diode and the reflector with PDMS for laser beam diffusion.

3.4. Communication characteristics measurements

The phosphor powders have effect on excitation pulse and cause its extension in the time domain. The time changes of pulses affect communication possibilities. The time extension of pulse decreases the frequency of pulses and thus limits the possible bit rate. We therefore measured time properties of pulses.

The laser diode had to be modulated for the communication characteristics measurements. The signal generator HMF2550 was a source of the square signal (150 kHz, amplitude 10 V, duty cycle 50%). The output of this generator was connected to the high power mount TCLDM9 (Thorlabs). This power mount has the RF input (SMA, 50 Ω) including Bias-T for RF modulation of the laser current from 100 kHz to 500 MHz. The frequency of the excitation square signal have to be greater than 100 kHz due to Bias-T. However, the time properties can be measured with lower frequency of the square signal. Further, the laser diode was supplied by the Benchtop LD Current Controller LDC240C (300 mA). The high power mount TCLDM9 with the laser diode lay on the table (laser beam aimed at the ceiling). Because the emitted laser beam is narrow, we used the glass diffuser, which has been mentioned in previous Subchap. 3.3. This diffuser was put on the power mount and each reflector with PDMS + phosphor powder was put on the diffuser. Above the reflectors, there was the Si photodetector PDA36A-EC (Thorlabs) which converted received optical signal into the electrical signal. The photodetector output was connected to the oscilloscope LeCroy 204Xi, which automatically detected and measured rise and fall edges of white light pulses.

The rise time is the time, in which the intensity of signal rises from 10% to 90%. Likewise, fall time is the time, in which the intensity of signal falls from 90% to 10%. In addition, photoluminescence (PL) decay times were also measured. For the two-level system [38], the emission rate is given by

$$I_{em} = -\frac{dN_2}{dt} = A_{21}N_2, \tag{1}$$

where N_2 is the number of emitters populating higher level at time t, and A_{21} is the spontaneous emission rate coefficient. After integration:

$$N(t) = N(0)\exp(-A_{21}t). \tag{2}$$

The number of emitters at any given time could be expressed in intensity

$$I(t) = I(0)\exp(-A_{21}t). \tag{3}$$

Substituting the emission lifetime $\tau = 1/A_{21}$ gives

$$I(t) = I(0)\exp(-t/\tau). \tag{4}$$

Thus after a time $t = \tau$ the emission intensity has decreased to $1/e$ (=0.368) value in time $t = 0$. τ is then $1/e$ emission lifetime [38].

The PL decay times were obtained after data processing. The waveforms of the measured signals were saved by the oscilloscope as a set of values (time and voltage). These values were then processed in Matlab, when the low level of saved signals was set to zero and the high level was set to one. Then the time differences between level ”1″ and level ”0.368″ were manually read from each waveform. This time is the PL decay time.

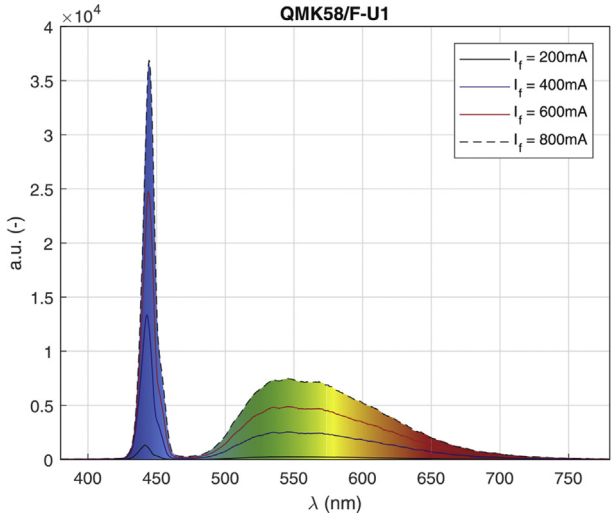

Fig. 2. Final spectra after excitation of phosphor powder QMK58/F-U1 by different forward currents.

4. Results of illumination characteristics measurements

The procedure of the illumination characteristics measurement has been described in Subchap. 3.3. The laser diode L450P1600 MM was in the continual supply mode. The measured results are in the following subchapters.

4.1. Phosphor powder QMK58/F-U1

Fig. 2 shows results of measured spectra with the phosphor powder QMK58/F-U1. As has been mentioned above, the forward current was gradually increased from 200 mA to 800 mA with the step of 200 mA. The measured values are summarized in Table 2.

4.2. Phosphor powder QMK58/F-U2

The same measurement was also done with the phosphor powder QMK58/F-U2. Measured spectra are shown in Fig. 3, the colour coordinates and CCT values are in Table 3.

4.3. Phosphor powder QMK58/N-U6

The measurement was repeated with the phosphor powder QMK58/N-U6. Measured spectra are shown in Fig. 4, the colour coordinates and CCT values are in Table 4.

4.4. Phosphor powder QUMK58/F-D1

The last measured phosphor powder was QUMK58/F-D1. Measured spectra are shown in Fig. 5, the colour coordinates and CCT values are in Table 5.

4.5. CIE1931 diagram

Measured values x and y of the all four phosphor powders for

Table 2
Colour coordinates and CCT of the phosphor powder QMK58/F-U1.

I_f (mA)	200	400	600	800
x (−)	0.3001	0.3008	0.3020	0.3026
y (−)	0.2852	0.2897	0.2944	0.2968
CCT (K)	8090.6	7896.7	7682.2	7580.4

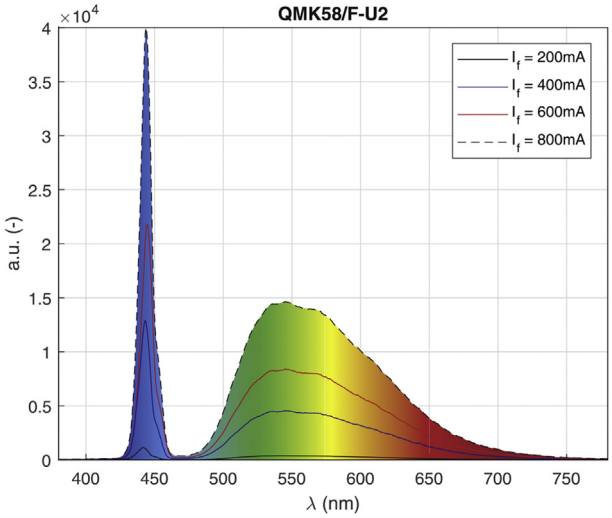

Fig. 3. Final spectra after excitation of phosphor powder QMK58/F-U2 by different forward currents.

Table 3
Colour coordinates and CCT of the phosphor powder QMK58/F-U2.

I_f (mA)	200	400	600	800
x (−)	0.3335	0.3374	0.3413	0.3445
y (−)	0.3568	0.3670	0.3764	0.3815
CCT (K)	5462.2	5318.5	5196.4	5085.8

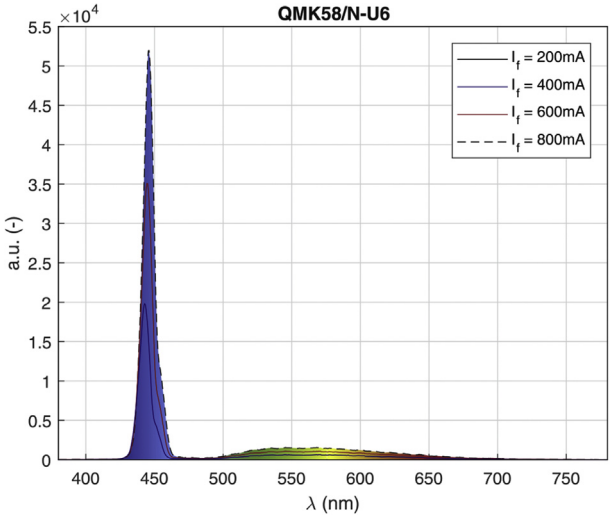

Fig. 4. Final spectra after excitation of phosphor powder QMK58/N-U6 by different forward currents.

Table 4
Colour coordinates and CCT of the phosphor powder QMK58/N-U6.

I_f (mA)	200	400	600	800
x (−)	0.2170	0.2069	0.2036	0.2017
y (−)	0.1122	0.0975	0.0951	0.0942
CCT (K)	1752.3	1652.3	1651.3	1654.4

forwards currents from 200 mA to 800 mA are presented in the CIE1931 diagram, see Fig. 6 and Fig. 7. Differences between the measured values (for each phosphor powder) are not significant. The values can be compared by the relation, which is derived from the relative error [43]:

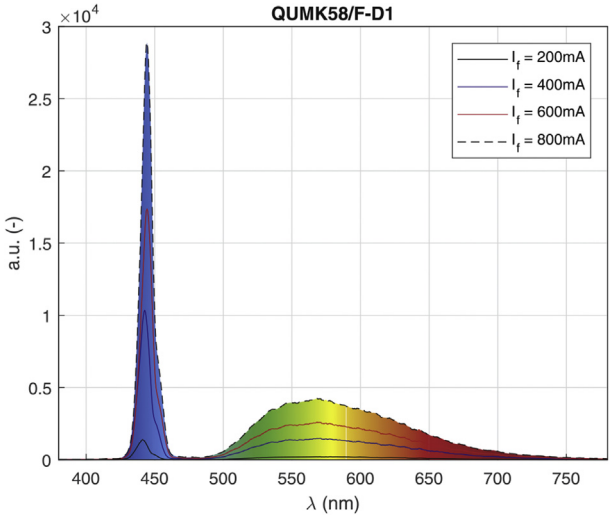

Fig. 5. Final spectra after excitation of phosphor powder QUMK58/F-D1 by different forward currents.

Table 5
Colour coordinates and CCT of the phosphor powder QUMK58/F-D1.

I_f (mA)	200	400	600	800
x (−)	0.3043	0.3019	0.3034	0.3017
y (−)	0.2430	0.2435	0.2483	0.2461
CCT (K)	10105.0	9711.2	9887.6	9425.2

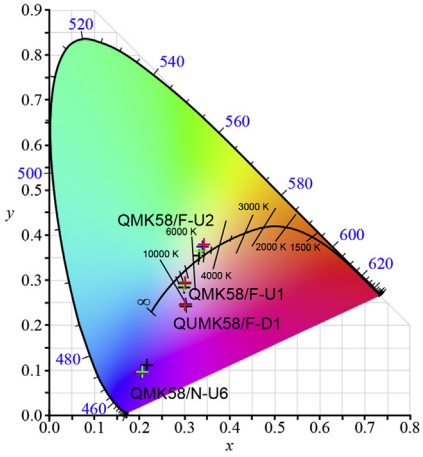

Fig. 6. CIE1931 diagram with measured colour coordinates. (For interpretation of the references to colour in this figure legend, the reader is referred to the Web version of this article.)

$$\Delta(\%) = \frac{x_{I_f=200\text{mA}} - x_{I_f=800\text{mA}}}{x_{I_f=800\text{mA}}} \cdot 100, \tag{5}$$

where $x_{I_f=200\text{mA}}$ is the value of colour coordinate x measured by forward current 200 mA and $x_{I_f=800\text{mA}}$ is the value of colour coordinate x measured by forward current 800 mA. This relation can also be applied on the CCT.

As regards the phosphor powders QMK58/F-U1 and QMK58/F-U2 we can claim that the colour coordinates x and y increase with increasing forward current and CCT decreases. The percentage difference of CCT values of these two phosphor powders changed by 6.73% and 7.40% respectively. These changes are not recognizable by the human eye. Moreover, the human eye is not able to perceive the very quick changes of excitation pulses given by modulation.

It was observed for the phosphor powders QMK58/N-U6 and

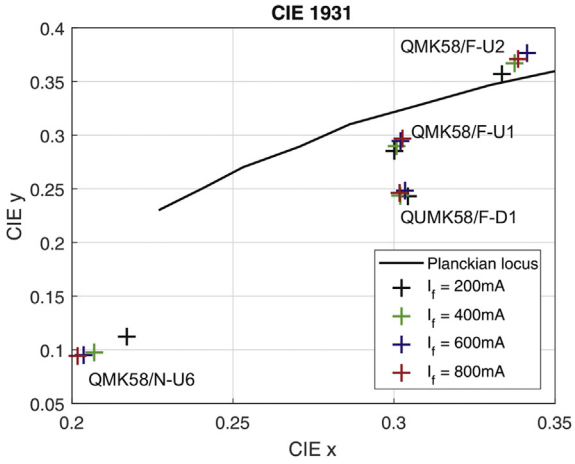

Fig. 7. Detailed CIE1931 diagram.

Table 6
Measured times of the white light pulses excited by the laser diode.

	rise time t_r (ns)	fall time t_f (ns)	decay time t_d (ns)
Square signal	6.6	6.8	–
QMK58/F-U1	33.7	35.2	32.8
QMK58/F-U2	35.6	35.9	33.4
QMK58/N-U6	36.1	36.3	33.1
QUMK58/F-D1	36.0	36.8	33.8

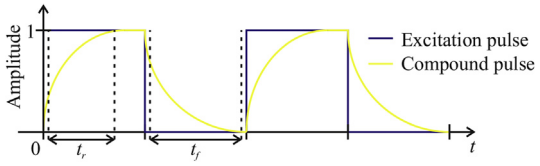

Fig. 8. Exciting pulses.

Table 7
Measured illumination characteristics of different concentrations of the phosphor powder QMK58/F-U2.

QMK58/F-U2 1:40	200 mA	400 mA	600 mA	800 mA
x (−)	0.3198	0.3244	0.3274	0.3285
y (−)	0.3310	0.3427	0.3504	0.3531
CCT (K)	6119.4	5859.5	5712.4	5665.9
QMK58/F-U2 1:35	200 mA	400 mA	600 mA	800 mA
x (−)	0.3335	0.3374	0.3413	0.3445
y (−)	0.3568	0.3670	0.3764	0.3815
CCT (K)	5462.2	5318.5	5196.4	5085.8
QMK58/F-U2 1:30	200 mA	400 mA	600 mA	800 mA
x (−)	0.3388	0.3410	0.3432	0.3434
y (−)	0.3679	0.3749	0.3805	0.3814
CCT (K)	5270.9	5204.2	5139.3	5133.0
QMK58/F-U2 1:25	200 mA	400 mA	600 mA	800 mA
x (−)	0.3420	0.3472	0.3470	0.3490
y (−)	0.3717	0.3843	0.3848	0.3897
CCT (K)	5162.7	5018.1	5027.0	4974.7

QUMK58/F-D1 that all measured values decreased with increasing forward current. The percentage difference of CCT values of these two phosphor powders changed by 5.92% and 7.21% respectively.

Generally, it is safe to say that in the case of all four phosphor powders the changing forward current does not have any important influence on the CCT of white light because the differences are small. It is very suitable for communication purposes, because the CCT does not change with the change of the intensity of excitation pulse. The excitation pulse can be modulated by some amplitude modulation.

The main result is that the most suitable phosphor powder for the creation of white light is the QMK58/F-U2, its average CCT was 5265 K. This light is usable for illumination purposes. Further, we measured the communication characteristics of all phosphor powders. This measurement is described in the following chapter.

5. Results of communication characteristics measurements

The procedure of the communication characteristics measurement has been described in Subchap. 3.4. The laser diode was switched on and off for measurement of time parameters. At first, we measured the rise and fall times of a square pulse from the signal generator. Then we gradually measured the rise, fall and PL decay times of the white light pulses created by the laser excitation of the PDMS + phosphor powders. The amplitude of this signal was 500 mA in on-state and 100 mA in off-state. The frequency was 150 kHz.

Table 6 shows the measured results of rise, fall and PL decay times. Presence of phosphor powders causes extension of the rise and fall edge and the pulse is thereby extended in the time domain.

We can calculate the maximal frequency of excitation pulses from the measured values. The following excitation pulse cannot appear earlier than the previous pulse stops shining. That means the time delay between the end of the exciting pulse and the beginning of the following pulse has to be longer than the fall time of the phosphor powder emission, see Fig. 8 (the blue curve is the excitation pulse and the yellow curve is the compound white light pulse). Otherwise, the Intersymbol Interference (ISI) can appear. The maximum frequency of the blue exciting laser diode is determined by the relation:

$$f_{max} = \frac{1}{2t_f}, \tag{6}$$

on condition that the duty cycle is 50%. In case of a smaller duty cycle, the frequency can be higher. However, the type of exciting pulse was not carried out in this measurement.

Maximum frequency of the excitation pulses for the phosphor powder QMK58/F-U1 is 14.2 MHz, for QMK58/F-U2 13.9 MHz, for QMK58/N-U6 13.8 MHz and QUMK58/F-D1 13.6 MHz. The bandwidth of VLC systems based on phosphor-converted LEDs reach the bandwidth approximately 2 MHz [44], [45]. If the excitation source is the laser diode instead the LED, the frequency of excitation pulses can increase. The phosphor powder QMK58/F-U1 showed the highest possible frequency, but its illumination characteristics are not usable for VLC. Therefore the QMK58/F-U2 is preferable.

It can be said that according to Table 6 that the communication properties of the tested phosphor powders are very similar. From the communication point of view, it does not matter which phosphor powder is used for white light creation. The phosphor powder QMK58/F-U2 showed the best illumination characteristics (the communication characteristics are very similar). Further, we got an idea to test another concentrations of the PDMS + phosphor powder which is described in the next chapter.

6. Influence of concentration of QMK58/F-U2 on illumination and communication characteristics

The previous measured phosphor powders were prepared in weight ratio 1:35 (phosphor powder:PDMS). The illumination characteristics of all four phosphor powders were different. In contrast, the communication parameters were very similar. The best illumination characteristics with regard to the CCT of created white light were observed

Table 8
Measured times of different concentrations of the phosphor powder QMK58/F-U2.

	rise time	fall time	decay time
	t_r (ns)	t_f (ns)	t_d (ns)
QMK58/F-U2 1:40	37.2	37.6	34.8
QMK58/F-U2 1:35	35.6	35.9	33.4
QMK58/F-U2 1:30	33.9	34.2	32.2
QMK58/F-U2 1:25	33.1	33.4	31.6

with the phosphor powder QMK58/F-U2, we therefore tested the influence of its concentration on the illumination and communication parameters. We created samples with concentrations 1:40, 1:30 and 1:25 as a supplement to the concentration 1:35.

These measurements showed that the illumination characteristics depend on the concentration of the phosphor powder. The more of phosphor powder in PDMS, the more of the exciting light is spectrally shifted and the final light is warmer. In comparison, natural daylight has CCT around 6500 K. The results of the colour coordinates and CCT are in Table 7.

The communication characteristics are summarized in Table 8. The PL decay times of all four concentrations of the phosphor powder QMK58/F-U2 were very similar and therefore their influence on the communication characteristics is similar as well.

It is evident, that the concentration of phosphor powder only affects the illumination characteristics. The measured times tend to shorten with the lower concentration, but the changes are not significant.

7. Conclusion

In this article, we evaluated the illumination and communication characteristics of four phosphor powders (QMK58/F-U1, QMK58/F-U2, QMK58/N-U6 and QUMK58/F-D1) to use in the VLC. The phosphor powders QMK58/F-U1, QMK58/F-U2, QMK58/N-U6 have the same chemical composition (Table 1), the last phosphor powder QUMK58/F-D1 additionally contains gadolinium Gd which causes the red shift of the Ce^{3+} emission. The tested phosphor powders were mixed in PDMS and hardened in a reflector. This makes it possible to test more phosphor powders or change their concentration. At the beginning, all phosphor powders were prepared in concentration 1:35. The results of the illumination characteristics measurements showed that the amount of forward current does not have a significant influence on spectral properties of the created white light. This is very beneficial for communication purposes because the intensity of excitation pulse can change without having any significant effect on the CCT. The excitation pulse can be modulated by some amplitude modulation. The phosphor powder QMK58/F-U1 excited by the blue laser light created the white light with CCT around 7800 K, CCT of the phosphor powder QMK58/F-U2 was around 5200 K. CCT of phosphor QMK58/N-U6 was around 1700 K and CCT of the last phosphor powder QUMK58/F-D1 was approximately 9800 K. The results of the communication characteristics showed that there are minimal differences between the phosphor powders and all have similar influence on signal pulses. The conclusion is that the most suitable phosphor powder is QMK58/F-U2 for illumination and communication purposes. Therefore, we also tested the other samples with the different concentrations of this phosphor powder. The other concentrations were 1:40, 1:30 and 1:25 as a supplement to the concentration 1:35. The illumination and communication characteristics were measured again. The results of the illumination and communication characteristics with different concentrations of the phosphor powder QMK58/F-U2 are similar. Further, we will deal with optical design for a better connection of the laser diode and the phosphor powder layer and the use of the higher modulation formats than On-Off Keying.

Acknowledgment

The authors would like to acknowledge the financial support of the Ministry of Education, Youth and Sports of the Czech Republic under Projects No. SP2018/117 and SP2018/184 of VŠB - Technical University of Ostrava, Czech Republic. Our research was also supported by Projects No. MP1401, TG01010137, VI20172019071, VI20152020008 and TA04021263. The work has been partially supported by projects CZ.1.07/2.3.00/20.0217 and CZ.02.1.01/0.0/0.0/16_019/0000867.

References

[1] S. Nakamura, G. Fasol, The Blue Laser Diode GaN Based Light Emitters and Lasers, first ed., Springer, Berlin, 1997.
[2] E.F. Schubert, Light-emitting Diodes, second ed., Cambridge University Press, Cambridge, 2006.
[3] S. Wang, Y. Li, L. Feng, L. Zhang, Y. Zhang, X. Su, W. Ding, F. Yun, Laser patterning of $Y_3Al_5O_{12}$:Ce^{3+} ceramic phosphor platelets for enhanced forward light extraction and angular color uniformity of white LEDs, Optic Express 24 (2016) 17522–17531.
[4] K.T. Bicanic, X. Li, R.P. Sabatini, N. Hossain, C.-F. Wang, F. Fan, H. Liang, S. Hoogland, E.H. Sargent, Design of phosphor white light systems for high-power applications, ACS Photonics 3 (2016) 2243–2248.
[5] X. Xiao, H. Tang, T. Zhang, W. Chen, W. Chen, D. Wu, R. Wang, K. Wang, Improving the modulation bandwidth of LED by CdSe/ZnS quantum dots for visible light communication, Optic Express 24 (2016) 21577–21586.
[6] F. Armetta, M.A. Sibeko, A.S. Luyt, D.F. Chillura Martino, A. Spinella, M.L. Saladino, Influence of the Ce:YAG amount on structure and optical properties of Ce:YAG-PMMA composites for white LED, Z. Phys. Chem. 230 (2016) 1219–1231.
[7] N.D.Q. Anh, T.H.Q. Minh, N.H.K. Nhan, Enhancing lighting performance of white LED lamps by green emitting Ce,Tb phosphor, Adv. Electr. Electron. Eng. 14 (2016) 609–614.
[8] J. Li, J.-G. Li, X. Li, X. Sun, Photoluminescence properties of phosphors based on Lu^{3+}-stabilized $Gd_3Al_5O_{12}$:Tb^{3+}/Ce^{3+} garnet solid solutions, Opt. Mater. 62 (2016) 328–334.
[9] M.S. Jang, Y.H. Choi, S. Wu, T.G. Lim, J.S. Yoo, Material properties of the Ce^{3+}-doped garnet phosphor for a white LED application, J. Infect. Dis. 17 (2016) 117–123.
[10] Y. Du, C. Shao, Y. Dong, Q. Yang, Electroluminescent properties of WLEDs with the structures of Ce:YAG single crystal/blue chip and $Sr_2Si_5N_8$:Eu^{2+}/Ce:YAG single crystal/blue chip, J. Disp. Technol. 12 (2016) 323–327.
[11] W. Macherzynski, J. Gryglewicz, A. Stafiniak, J. Prazmowska, R. Paszkiewicz, Formation process and properties of ohmic contacts containing molybdenum to AlGaN/GaN heterostructures, Adv. Electr. Electron. Eng. 14 (2016) 83–88.
[12] S.V. Nizhankovskyi, A.V. Tan'ko, Y.N. Savvin, S.I. Krivonogov, A.T. Budnikov, A.V. Voloshin, Single crystalline YAG: Ce phosphor for powerful solid-state sources of white light. The influence of production conditions on luminescence properties and lighting characteristics, Optic Spectrosc. 120 (2016) 915–921.
[13] J.-S. Li, J.-X. Chen, L.-W. Lin, Z.-T. Li, Y. Tang, B.-H. Yu, X.-R. Ding, A detailed study on phosphor-converted light-emitting diodes with multi-phosphor configuration using the finite-difference time-domain and ray-tracing methods, IEEE J. Quant. Electron. 51 (2015) 1–10.
[14] S. Hu, C. Lu, G. Zhou, X. Liu, X. Qin, G. Liu, S. Wang, Z. Xu, Transparent YAG: Ce ceramics for WLEDs with high CRI: Ce^{3+} concentration and sample thickness effects, Ceram. Int. 42 (2016) 6935–6941.
[15] S.A. Hassanzadeh-Tabrizi, Synthesis and luminescence properties of YAG: Ce nanopowder prepared by the Pechini method, Adv. Powder Technol. 23 (2012) 324–327.
[16] S. Nishiura, S. Tanabe, K. Fujioka, Y. Fujimoto, Properties of transparent Ce:YAG ceramic phosphors for white LED, Opt. Mater. 33 (2011) 688–691.
[17] D.E. Kuznetsova, G.A. Dosovitskiya, A.E. Dosovitskiy, Transparency and microstructure of YAG: Ce phosphor particles, Opt. Mater. 66 (2017) 547–551.
[18] R. Perez-Jimenez, J. Rufo, C. Quintana, J. Rabadan, F.J. Lopez-Hernandez, Visible light communication systems for passenger in-flight data networking, IEEE International Conference on Consumer Electronics (ICCE), IEEE, Las Vegas, 2011, pp. 445–446.
[19] J. Park, J. Kim, H. Kwon, Phosphor-aluminum composite for energy recycling with high-power white lighting, advanced, Opt. Mater. 5 (2017) 1–6.
[20] J.R. Oh, S.H. Cho, Y.H. Lee, Y.R. Do, Enhanced forward efficiency of $Y_3Al_5O_{12}$:Ce^{3+} phosphor from white light-emitting diodes using blue-pass yellow-reflection filter, Optic Express 17 (2009) 7450–7457.
[21] A. van Os, M.J.C. Stassen, M.J. Tassignon, J.J. Rozema, Influence of yellow filters on straylight measurements, J. Cataract Refract. Surg. 43 (2017) 1077–1080.
[22] G. Owczarek, G. Gralewicz, N. Skuza, P. Jurowski, Light transmission through intraocular lenses with or without yellow chromophore (blue light filter) and its potential influence on functional vision in everyday environmental conditions, Int. J. Occup. Saf. Ergon. 22 (2016) 66–70.
[23] T. Stratil, P. Koudelka, R. Martinek, T. Novak, Active pre-equalizer for broadband over visible light, Adv. Electr. Electron. Eng. 15 (2017) 553–560.
[24] X. Huang, J. Shi, J. Li, Y. Wang, N. Chi, A Gb/s VLC transmission using hardware preequalization circuit, IEEE Photon. Technol. Lett. 27 (2015) 1915–1918.

[25] X. Huang, Z. Wang, J. Shi, Y. Wang, N. Chi, 1.6 Gbit/s phosphorescent white LED based VLC transmission using a cascaded pre-equalization circuit and a differential outputs PIN receiver, Optic Express 23 (2015) 22034–22042.
[26] Y. Wang, N. Chi, Investigation of advanced pre- and post-equalization schemes in high-order CAP modulation based high-speed indoor VLC transmission system, in: X. Zhang, B. Li, C. Yu (Eds.), Proceedings of SPIE: Optoelectronic Devices and Integration VI, SPIE, Beijing, 2016, pp. 1–9.
[27] X. Li, B. Hussain, L. Wang, J. Jiang, C. Patrick Yue, Design of a 2.2-mW 24-Mb/s CMOS VLC receiver SoC with ambient light rejection and post-equalization for Li-Fi applications, J. Lightwave Technol. 36 (2018) 2366–2375.
[28] T. Stratil, P. Koudelka, J. Jankovych, V. Vasinek, R. Martinek, T. Pavelek, Broadband over Visible Light: high power wideband bias-T solution, 10th International Symposium on Communication Systems, Networks and Digital Signal Processing (CSNDSP), IEEE, Prague, 2016, pp. 1–5.
[29] BMW, BMW Laserlight technology: how it works and benefits, https://www.bmwoffreeport.com/blogs/827/how-bmw-lasterlight-work-and-what-are-benefits/, (2017) , Accessed date: 21 January 2018.
[30] Audi Technology Portal, Matrix laser technology, https://www.audi-technology-portal.de/en/electrics-electronics/lighting-technology/matrix-laser-technology1, (2015) , Accessed date: 23 January 2018.
[31] S. Li, Q. Zhu, D. Tang, X. Liu, G. Ouyang, Liangliang Cao, N. Hirosaki, T. Nishimura, Z. Huanga, R.-J. Xie, Al_2O_3YAG: Ce composite phosphor ceramic: a thermally robust and efficient color converter for solid state laser lighting, J. Mater. Chem. C 37 (2016) 8648–8654.
[32] M. Cantore, N. Pfaff, R.M. Farrell, J.S. Speck, S. Nakamura, S.P. DenBaars, High luminous flux from single crystal phosphor-converted laser-based white lighting system, Optic Express 24 (2016) A215–A221.
[33] T.-C. Wu, Y.-C. Chi, H.-Y. Wang, C.-T. Tsai, C.-H. Cheng, J.-K. Chang, L.-Y. Chen, W.-H. Cheng, G.-R. Lin, White-Lighting communication with a $Lu_3Al_5O_{12}:Ce^{3+}$/$CaAlSiN_3:Eu^{2+}$ glass covered 450-nm InGaN laser diode, J. Lightwave Technol. 36 (2017) 1634–1643.
[34] Y.H. Song, E.K. Ji, B.W. Jeong, M.K. Jung, E.Y. Kim, C.W. Lee, D.H. Yoon, Design of laser-driven high-efficiency Al_2O_3/YAG: Ce^{3+} ceramic converter for automotive lighting: fabrication, luminous emittance, and tunable color space, Dyes Pigments 139 (2017) 688–692.
[35] O.R. Abdullaev, A.V. Aluev, Y.L. Akhmerov, N.V. Kourova, M.V. Mezhennyi, A.A. Chelny, White light source with laser-excited phosphor, Quant. Electron. 47 (2017) 927–931.
[36] K.A. Denault, M. Cantore, S. Nakamura, S.P. DenBaars, R. Seshadri, Efficient and stable laser-driven white lighting, AIP Adv. 3 (2013) 1–6.
[37] T. Tomiki, H. Akamine, M. Gushiken, Y. Kinjoh, M. Miyazato, T. Miyazato, N. Toyokawa, M. Hiraoka, N. Hirata, Y. Ganaha, T. Futemma, Ce^{3+} centres in $Y_3Al_5O_{12}$ (YAG) single crystals, J. Phys. Soc. Jpn. 60 (1991) 2437–2445.
[38] R. Withnall, J. Silver, Luminescence of phosphors, in: J. Chen, W. Cranton, M. Fihn (Eds.), Handbook of Visual Display Technology, Springer, Berlin, 2012, pp. 1013–1028.
[39] S. Hirano, G. Okada, N. Kawaguchi, H. Yagi, T. Yanagitani, T. Yanagida, Scintillation properties of Ce-doped $(Gd_{0.32}Y_{0.68})_3Al_5O_{12}$ transparent ceramics, Opt. Mater. 66 (2017) 410–414.
[40] Dow Corning, Sylgard 184 silicone elastomer kit, http://www.dowcorning.com/applications/search/default.aspx?R=131EN, (2016) , Accessed date: 12 July 2017.
[41] Roithner LaserTechnik, CLP series reflectors for lambertian, http://www.roithner-laser.com/datasheets/led_optics/clp17cr_clp20cr.pdf, (2012) , Accessed date: 21 January 2017.
[42] Thorlabs, L450P1600MM. https://www.thorlabs.de/thorproduct.cfm?partnumber=L450P1600MM, 2016 (accessed 15 March 2017).
[43] R.S. Witte, J.S. Witte, Statistics, ninth ed., Wiley, Hoboken, 2009.
[44] W.O. Popoola, E. Poves, H. Haas, Error performance of generalised space shift keying for indoor visible light communications, IEEE Trans. Commun. 61 (2013) 1968–1976.
[45] M. Biagi, T. Borogovac, T.D.C. Little, Adaptive receiver for indoor visible light communications, J. Lightwave Technol. 31 (2013) 3676–3686.

Optical Switching and Networking 33 (2019) 184–193

Contents lists available at ScienceDirect

Optical Switching and Networking

journal homepage: www.elsevier.com/locate/osn

Influence of simulated atmospheric effect combined with modulation formats on FSO systems

Jan Latal [a,*], Jan Vitasek [a], Lukas Hajek [a], Ales Vanderka [a], Radek Martinek [b], Vladimir Vasinek [a]

[a] VSB–Technical University of Ostrava, Faculty of Electrical Engineering and Computer Science, Department of Telecommunications, 17. listopadu 15/2172, Ostrava-Poruba, Czech Republic

[b] VSB–Technical University of Ostrava, Faculty of Electrical Engineering and Computer Science, Department of Cybernetics and Biomedical Engineering, 17. listopadu 15/2172, Ostrava-Poruba, Czech Republic

ARTICLE INFO

Keywords:
OWC
FSO
Modulation format
USRP
EVM
MER

ABSTRACT

This article describes the possibility of using the Software Defined Radio (SDR) for modulation of the optical laser beam by advanced m-PSK and m-QAM modulations with regard to influence of simulated atmospheric effect, in our case rain in simulation acrylate box. There were tested the laser sources emitting the wavelengths 650 and 850 nm for comparison their behaviour in simulated atmospheric effect: rain (heavy, light, drizzle). By the help of the equipment NI USRP 2920 we could flexibly and sophisticated change the modulation formats without a necessity of creating complex electronic circuits ensuring modulation and demodulation of communication wireless signal. To make conclusions regarding the use of SDR for OWC, we performed a variety of tests in order to determine the resistance of the modulation formats to the simulated atmospheric effect with the aid of the Error Vector Magnitude (EVM) and Modulation Error Ratio (MER) parameters.

1. Introduction

The Free Space Optical (FSO) systems became the one of the main pillar of alternative communication in the modern telecommunication networks because thanks them we can provide high data rates between network nodes. Nowadays, mobile operators as well as Internet Service Providers (ISP) search for new methods to provide pervasive (anytime, anywhere) access to mobile Internet end users. Conventional wireless technologies based on radio waves (Wi-Fi, WiMAX or mobile networks 4G or 5G) are burdened by the strict regulation of the frequency bands imposed by the national telecom regulators as well as international regulators [1–3]. This disunity of frequency band, elimination of free band, and reduced possibilities in increasing transmission speeds have led to the search for new means of communication technologies. Most recently, more attention is being dedicated to taking advantage of optical wireless systems, namely Free Space Optical (FSO) communication, for outdoor static usage [4]. The FSO communication systems use laser diode or LEDs to produce a signal in near infrared range, i.e., they are operating at 780–900 nm and 1500–1600 nm for their working [5]. The wavelength 1550 nm is generally preferable to use in FSO system because the human eyesight is more resistant against the damage. However the wavelength 850 nm is also used. This wavelength is used due to good transmission features of the atmosphere. Laser diodes used in FSO communication systems are: vertical cavity surface emitting laser (VCSEL) at 850 nm, Fabry-Perot at 1550 nm, distributed feedback lasers (DFB) at 1550 nm and Nd: YAG at 1064 nm, which systems TESAT use [6–8].

The FSO connection offers obvious advantages over other communication systems and allows for the possibility of using non-licensed frequency bands in the visible or invisible parts of the spectrum also potential large bandwidth, license-free operation, high security and interference immunity [9]. At the same time these systems are joinable to the current data networks (there is protocol transparency to the other network types) and there is not any need of special protocol convertors. The advantage of wireless optical systems is their possibilities of network topology, namely Point to Point (P2P) connection or Point to Multipoint (P2MP) connection, which is in principle the analogy of wireless radio networks. The FSO is realized in the troposphere, which is 7 km high in the Polar Regions and 17 km around the Equator [10,11].

* Corresponding author.
E-mail address: jan.latal@vsb.cz (J. Latal).

https://doi.org/10.1016/j.osn.2018.01.001
Received 1 August 2017; Received in revised form 30 November 2017; Accepted 2 January 2018
Available online 6 January 2018
1573-4277/

The atmosphere is the medium of transmission for both radio and FSO telecommunications technologies, it is essential to consider a variety of physical atmospheric effects, including rain, fog, turbulences (air, thermal), smog, snow, haze, and others [12–16]. The inherent characteristics of some of these effects cause complete disconnectivity for the whole duration of their presence and activity. Therefore the most of outdoor FSO links has a system based on radio waves, which compensates a possible downgrade of the atmosphere as a backup communication. While rain, which decreases the power level of the transmitted signal, causes the biggest problem for radio systems, fog or heavy snow can also produce considerable complication for FSO communication systems [17]. With temperature and pressure fluctuations, the refractive index changes on the trace between two optical heads of FSO system.

These fluctuations in signal intensity, known as scintillations, could dramatically reduce the intensity of modulation with direct detection (IM/DD) in FSO communication systems even during clear weather [18]. The early phases of construction and development of the FSO communication systems necessitated searching for a link code, or a modulation of proper format, which would be resistant to several types of atmospheric effects. The On-Off Keying (OOK) format in combination with Return-to-Zero (RZ) or Non-Return-to-Zero (NRZ) coding was selected as the easiest modulation format.

The FSO communication systems are now well placed in commercial space primarily due to their simplicity of fabrication, relatively sensible bandwidth usage, and effectiveness as well as the simplicity of their peripherals. It is advantageous to use OOK modulation with RZ coding rather than with NRZ coding because the former scheme makes it possible to synchronize lower power transmission in the receiving part of the FSO. Although, the OOK is the simplest modulation format, it is very sensitive to atmospheric turbulences during, which the receiving optical power fluctuates greatly, and this significantly impacts the decision-making level of the FSO system [19–22]. The other types of modulation formats that have been considered for communication in FSO systems are Pulse Position Modulation (PPM), Phase-Shift Keying (PSK), Differential Phase-Shift Keying (DPSK), Differential Quadrature Phase Shift Keying (DQPSK) and Frequency Shift Keying (FSK) schemes [23–25,27]. The advantage of these types of modulation formats is mainly their better utilization of optical beam power during turbulences, as compared to the OOK. At the same time, opportunities for using the Polarization Shift Keying (PolSK) modulation format have arisen. This alternative scheme, by presenting high resistance to laser phase noise, is less susceptible to frequency chirp. PPM is excellent alternative modulation format but with poor bandwidth-efficiency. The main outputs from measurements of PPM against atmospheric turbulences were done in research [30]. At Subcarrier Intensity Modulation (SIM) we use several digital input streams modulated by various sub carrying radio frequencies (RF) [26]. Thanks to this arrangement, the adaptive voltage threshold is not as necessary as it is in the OOK modulation in FSO communications systems. With the utilization of SIM we can achieve better capacity in FSO systems and to mitigate turbulence-induced signal scintillation [28]. Diversity, forward error checking, and Subcarrier Time Delay Diversity (STDD) techniques decrease the impact of scintillation on the optical beam [29]. Many research teams have dealt with development and using of different types of modulation formats with the aim of achieving of better parameters: increasing of power efficiency, increasing of bandwidth, increasing of data rate, decreasing of BER, resistance against the atmospheric effects etc. [31–35]. The most of articles focus on measurement or simulation of atmospheric turbulences, which have together with a fog absolutely the greatest influence on FSO systems [36–52]. As well the possibilities of using xWDM systems for suppression of undesirable atmospheric effects on FSO systems were studied [53].

However, some articles deal with problem of influence of rainfall on radio or optical systems, which is the main contribution of this article. Maha Achour have dealt with rainfall simulation in 2002, he set models for attenuation caused by rainfall, rainfall totals, he defined a velocity of falling drops with different sizes [54]. Fatin Hamimi Mustafa et al. dealt with influence of rainfall on FSO systems in Kuala Lumpur region, they analyzed data for heavy rain and light rain or drizzle from 2001 [55]. Another team [56] studied some different models of attenuation of rainfall at the same place during one year. From the measured of rainfall totals they made models predicted behaviour of FSO in comparison with models according to ITU-R P.838, R. Based on measurement [57] and Mie theory it was observed that the attenuation does not depend on the wavelength. Zvanovec's article [58] studied the influence of rainfall on diversity of FSO systems. Based on data obtained from Czech Hydrometeorological Institute (CHMI) the simulations of behaviour for different rainfall totals were done. The influence of rain drops on wavelengths 532 and 655 nm was studied in Ref. [59]. It was found that the attenuation increases nonlinear with linear increasing velocity of rain drops. It was also found that the rainfall more effects on wavelength 532 nm. Influence of velocity of rain drops for region Changsha, China was studied in Ref. [60]. There was used Spectrum Sliced Wavelength Division Multiplex (SS-WDM) for heavy rain. The results of simulations showed that using of SS-WDM, data rate 1.56 Gb s^{-1}, laser diode 1550 nm, optical power 0 dB can reach distance 2.5 km with BER = $9.816 \cdot 10^{-11}$. WDM without Spectrum Sliced technique reached BER = 10^{-3} equal to in simulations, optical power 10 dBm at the same distance.

This article focuses on behaviour of optical wireless link, which was created in laboratory conditions under effect of rain drops sprayed from three types of calibrated nozzles. These nozzles can create heavy and light rain and drizzle, which effect on the optical modulated beam passing through the acrylate box. In our experiment we tested the following modulation formats: QPSK, 8PSK, 16PSK, $\frac{\pi}{4}$ DQPSK, 4QAM, 16QAM, 32QAM and 64QAM. The communication quality and influence of rainfall/drops is evaluated for different types of modulation formats together with parameters MER and EVM. For more detail understanding of done experiments and their evaluations we applied the statistical tools on measured data.

This article is composed from the sections, which describe experimental works: Section 2 describes basic mathematical relations, which define the attenuation caused the rain drops defined by recommendation ITU-R P.838-2. Next Section 3 describes measuring arrangement and used components. The Section 4 describes used types of modulation formats and defines parameters EVM and MER. Following Section 5 deals with practical measurement and obtained results, which are worked up in dependence for MER for different wavelengths, modulation formats together with setting of rain. The next to the last Section 6 deals with statistical evaluation of measured data (EVM and MER) and their mutual correlation between modulation formats and other parameters. The last Section 7 describes conclusions of experiments.

2. Mathematical definition of rainfall attenuation

The rain is water-fall falling from cloud in drop shape with diameter from 0.2 to 7 mm, greater drops are unstable and decay. The rain consists of hydrometeors, which are classified as liquid vertical waterfall. The rainfall is very often meteorological effect, which significantly effect on transmission. However, the rain above all causes decreasing of FSO range and has smaller influence than fog. This is caused that the diameter of drops is considerably greater than wavelength of light. Laser beam can pass through rain drops with smaller scatter against particles making fog, which are very small and stay longer in the atmosphere. Each drop become a new source of secondary radio waves (Huygens principle), the energy dissipates in undesirable directions and also it happens the deploy the polarization plane, it is origin of direct polarization or depolarization of passing electromagnetic wave.

By the calculation of rainfall attenuation it is taken into account the attenuation factor calculated on unit of length. The attenuation factor of rainfall was analyzed and studied during the data transmission through the FSO system. Models of rainfall attenuation are defined by the help

of experimental methods or objective method. Especially for higher frequencies above 10 GHz it is spoken about the real atmosphere (fog, rain, snow, …) where appears influence of rain drops for radio links (RF). As well the rain drops change polarization of electromagnetic waves in RF, which leads to power loss [61,62].

The rainfall for FSO has a character of non-selective scatter. It happens on particles much larger than wavelength (size parameter where $x_0 = \frac{a}{\lambda} >> 1$). These particles are great particles of fog, rain, snow or hailstones. The non-selective scatter can be expressed by relation:

$$\beta_{rain} = \pi \cdot a^2 \cdot N_a \cdot Q_{scattering} \cdot \left(\frac{a}{\lambda}\right), \tag{1}$$

where: a - radius of rain drop (0.001–0.1 cm), $Q_{scattering}$ - scattering coefficient (=2) sometimes defined as Mie attenuation coefficient, N_a - distribution of rain drops (cm^{-3}), λ - wavelength of laser source (m). Distribution of rain drops can be calculated by following relation [54]:

$$N_a = \frac{R}{1.33 \cdot \pi \cdot a^3 \cdot V_a}, \tag{2}$$

where: R - rainfall intensity (cm s^{-1}), V_a - rainfall velocity given by relation [54]:

$$V_a = \frac{2 \cdot a \cdot \rho \cdot g}{9 \cdot \eta} = 1.210^6 a^2, \tag{3}$$

where: ρ - water density ($\rho = 1$ gr cm^{-3}), g - gravitational constant ($g =$ 980 cm s^{-2}), η - air viscosity ($\eta = 1.8 \cdot 10^{-4}$ gr (cm s)$^{-1}$). According to above mentioned values we can say that exists $\rho\, z_a$ gram of water fall per cm per second, and that the number of drops in V_a cm^3 is given by the following equation [54]:

$$X_a = \frac{z_a}{\frac{4}{3} \cdot \pi \cdot a^3}, \tag{4}$$

where z_a is the rainfall rate (cm s^{-1}) of a drop size of radius a (mm). The final rain attenuation expressed by attenuation can be calculated by relation [54]:

$$\tau = \exp(-\beta_{rain} L). \tag{5}$$

The rain attenuation can be modelled by following relation called Carbonnean relation defined in ITU-R P.838-2 [63]:

$$\alpha_{rain} = kR^{\alpha} = 1.076\, R^{2/3} \quad (\mathrm{dB} \cdot \mathrm{km}^{-1}), \tag{6}$$

where: R - rainfall (mm hr^{-1}). Above mentioned relation Eq. (6) has the same coefficients for all values of rainfall totals. Article [63] defines a similar model but its coefficients also depend on rainfall intensity. This model in comparison to Eq. (6) has smaller error of estimated attenuation against measured attenuation. These coefficients are in Table 1.

In ITU-R [64] methods, it is recommended that the rainfall needs to be measured at interval of 1 min in order to determine the rain rate [9]. Values k and α in Carbonnean model are predicted according to measurements done in France. However, the measurements are based on very low rainfall intensity in comparison to rainfall in tropic regions. The regions have different rainfall intensity. In UK, heavy rain means 5 mm hr^{-1} whereas heavy rain in tropic region is 200 mm hr^{-1}. Many raindrop-size distributions have been proposed. Marshall and Palmer [2] proposed the following well known empirical expression by fitting their data and the Laws and Parsons data. Their data was taken in Ottawa, Canada in 1946 using the filter paper method. The fit of this distribution to the experimental points was not very good for drops less than $D = 1$ mm [65]. Parameters k and α according to Marshal-Palmer and Joss distribution are based on drop size. For this we have to know negative exponential approximation of drop spectrum $N(D)$ [66]:

$$N(D) = N_0 \exp(-\Lambda D)\ \mathrm{mm}^{-1-\mu}\ \mathrm{m}^{-3}, \tag{7}$$

where D is the diameter in mm, N_0 (mm^{-1} m^{-3}) and Λ (mm^{-1}) are empirical parameters. The typical value N_0 for average rain is 8000 m^{-3} mm^{-1}) [66]:

$$\Lambda = 4.1 \cdot R^{-0.21}\ \mathrm{mm}^{-1}. \tag{8}$$

Λ decreases with increasing rainfall intensity R (mm hr^{-1}). The rainfall intensity R can be calculated as:

$$R = 60 \cdot \frac{\Delta H}{\Delta t}. \tag{9}$$

The rain intensity that has the integration time t minutes i.e. R, is also called “the (average) t - minute rain intensity”, ΔH is the rainfall amount increment (mm). Further for calculation of Marshal-Palmer and Joss distribution we use relation Eq. (8) put in Eq. (7) and final formula is given by relation [66]:

$$N(D,R) = 8000 \cdot \exp\left(\frac{-4.1 \cdot D}{R^{0.21}}\right). \tag{10}$$

where then $N(D,R)$ sets the account of drops with effective drop diameter in interval (D to $D + dD$) in unit of volume. It is given in units cm^{-4}. If we know the distribution and size of rain drops in space we then know what happens by interaction of one drop with electromagnetic wave. We are able to set the attenuation or wave scattering. The total attenuation A is given by integration of attenuation factor on trace [58]:

$$A = \int_0^L \alpha(l)\mathrm{d}l, \tag{11}$$

where L is length of an optical link. This model for calculation of attenuation is mostly used for statistical calculations usually for yearly or in worse case monthly attenuation predictions.

Table 1
Coefficients for relation Eq. (6) according rainfall totals [64].

Rainfall totals R (mm hr^{-1})	k	α
120 to 160	11.296	0.1683
103 to 120	0.2961	0.9300
70 to 103	0.2791	0.9471
12 to 70	0.4195	0.8486

3. Experimental workplace for simulation of rainfall

We constructed a system for creating a rainfall with special calibrated nozzles. In this system we studied behaviour of the modulated optical beam affected by rainfall. There were used three nozzles with spray of full cone. The nozzles spray particles with different sizes but this information is not given by manufacturer. The nozzles are labelled 90B2FP6.5, 90B1FP3.5 and 90B1FP1.0.

Thanks to the three different nozzles we can observe how the parameters change according size of sprayed particles. The measurements were done in acrylate box with sizes $0.5 \times 0.5 \times 2.5$ m (thickness of the acrylate box is 0.5 cm). In this acrylate box there was placed a supporting structure for mounting the nozzles. The water was pumped from tank by pump Gardena type 5000/5 in a water distribution, which leads water to the nozzles. The water distribution includes a regulator Siemens SSD31, which is controlled by a program created in LabVIEW. The regulator controls the flow of water a thereby sets the rainfall. Water from regulator passes through a flowmeter for monitoring the water flow. The flowmeter Biotech 150189 sends square pulses. The program set the water flow according to the account of pulses. Further the water goes through splitter in four lines. These lines were same long for the same pressure in the each nozzle. Three lines are ended by nozzle, the last fourth serves for control pressure measurement ensuring stable conditions in lines. The nozzles are mounted on adjustable holder therefore the positions of nozzles could be changed. The distance between nozzles was 0.6 m, distance to the ends was 0.65 m. The whole system is in Fig. 1.

We have mentioned above that we did not know the sizes of drops therefore we measured it by the help of the high-speed camera. In the experiment we measured the droplets from one nozzle. The following

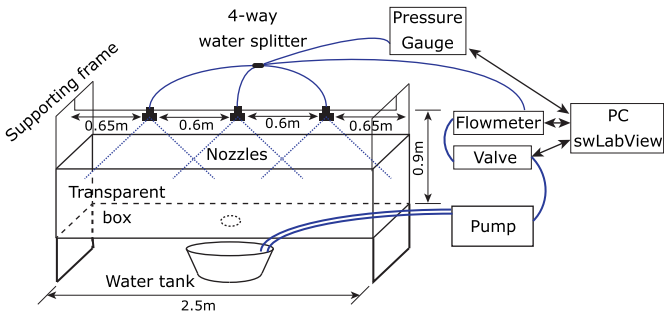

Fig. 1. Scheme of system for rain simulation.

Fig. 2 shows the nozzle type 90B1FP1.0. Software Fiji can measure sizes by the help of reference distance. The software analyzed 20 drops in figure, the average size of drop was 460 μm. The drizzle is defined for drop size smaller than 0.5 mm, which answers the measured nozzle.

Above we presented the parameters, which describe the workplace for simulation of rainfall. In the following text we present information about the whole experimental arrangement for measurement of rainfall on modulated optical beam. The laser diode with drivers and photodetector were placed outside the acrylate box. The laser diode was aligned in the center of the acrylate box. The scheme is in the following Fig. 3.

The modulation of laser diode was done by the help of USRP NI 2920, which sent data signal to the laser diode. There were used two laser sources emitting 650 and 850 nm (type U-LD-650543A and L850P010), detail information in Table 2. Laser beam passes through

Fig. 2. View of rain in high-speed camera.

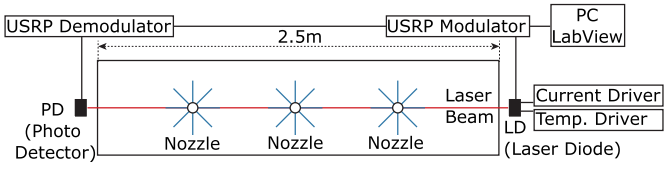

Fig. 3. Scheme of measurement.

acrylate box in, which was affected by the rainfall. Based on measurement of the water flow through the flowmeter Biotech 150189 for our prepared system of rain simulator we then used by calculation of rainfall totals for different types of nozzles and valve openings (50 or 100%). There were set two water flows (100% and 50% valve opening) for each nozzle and for each modulation. The water flow and pressure were following by 100% valve opening: 8.3 l min^{-1} (498 mm hr^{-1}) 0.7 bar for heavy rain, 6.3 l min^{-1} (378 mm hr^{-1}) 2.3 bar for light rain and 1.6 l min^{-1} (96 mm min^{-1}) 4.1 bar for drizzle. For 50% valve opening: 5.3 l min^{-1} (318 mm hr^{-1}) 0.4 bar for heavy rain, 3.6 l hr^{-1} (216 mm hr^{-1}) 1.8 bar for light rain and 1 l min^{-1} (60 mm hr^{-1}) 3.7 bar for drizzle. Totally there were 6 measuring steps for each wavelength. Affected modulated laser beam impacted on the photodetector Thorlabs PDA10A-EC (with technical parameters: Si Fixed Gain Detector, detection of light signals ranging 200–1100 nm, 150 MHz Bandwidth, active detection area 0.8 mm^2) [67]. Electrical signal from the photodetector went to the second USRP NI 2920 unit.

We have mentioned that the modulations were created in USRP units controlled by LabVIEW. We created a program for PSK and QAM modulations and demodulations. Further we set communication parameters: center frequency, pre-filter gain and symbol rate. After the demodulation the program shows constellation diagram, eye diagram and numeric parameters MER and EVM.

The setting for measurement was following:

- IP address: 192.168.10.2 (modulator) and 192.168.10.3 (demodulator).
- Center frequency: 50 MHz.
- Gain: 0 dB.
- Symbol rate: 500 kHz.
- Shape filter: none.
- Number of symbols: 500.

The measurement was following. We used both wavelengths. The measurement of each modulation took 5 min. By the help of exploration analyse it was calculated the mean values of MER and EVM.

4. Types of modulation formats and description of qualitative parameters of modulations

We used several types of modulation formats in our experiment: QPSK, 8PSK, 16PSK, $\frac{\pi}{4}$ DQPSK, 4QAM, 16QAM, 32QAM and 64QAM for testing their features against rainfall in point of view MER, EVM and constellation diagrams. Below there is a description of M-PSK and M-QAM modulations together with explanation of qualitative parameters MER and EVM.

4.1. Phase modulation (M-PSK)

Phase shift keying is a technique, which changes the phase of carrier wave. BPSK modulation has two changes of phase, the first change means log. 1 and other log. 0. If the input signal changes from one level to the other, the phase of output signal is changed into value π. The demodulator has to detect the phase change and these changes convert to the original symbols. This is possible by two ways. The first

Table 2
Parameters of used laser sources.

Laser type	Power (mW)	Wavelength (nm)	Beam divergence for parallel emitting	Beam divergence for perpendicular emitting	Operation Current (mA)
U-LD-650543A	max. 5	650	12	42	max. 25
L850P010	max. 10	850	8	30	max. 70

way is comparison of received signal with reference signal. This way is called as coherent detector. BPSK has only two states. That means that one symbol equals one bit and therefore this modulation is called as 2PSK. There are also more state M-PSK modulations, which carry in one symbol more bits. These more state modulations are less robust than BPSK. Very often used more state modulations with phase shift keying is QPSK or 8PSK. Variant QPSK uses four states, each state maps two bits in one symbol. QPSK has double bit rate in comparison to BPSK with the same bandwidth. Differential phase shift keying has an advantage that receiver does not need any reference signal for demodulation. It demodulates on basis previous state of input signal. Using of differential keying at transmitter means that a bit with log. 1 will be transmit with phase shift π regard to previous phase and bit with log. 0 will be transmit without phase change [68]. More state phase shift keying M-PSK assumes carrier signal, which phase can have M different values [68]:

$$s_i(t) = \sqrt{\frac{2E}{T}} \cos\left(2\pi f_c t + \frac{2\pi i}{M}\right) \qquad i = 0, 1, \ldots, M-1. \tag{12}$$

Because these signals could be resolved into two orthogonal parts, the base is made by two signals [68]:

$$\phi_1(t) = \sqrt{\frac{2}{T}} \cos(2\pi f_c t), \qquad 0 \le t \le T, \tag{13}$$

and

$$\phi_2(t) = \sqrt{\frac{2}{T}} \sin(2\pi f_c t), \qquad 0 \le t \le T, \tag{14}$$

where $\|\cos(2\pi f_c t)\| = \sqrt{\frac{T_b}{2}}$ is relation for norm of harmonic signal, harmonic signals with phase 0 and π represent bits 1 and 0 and they are then normed and multiplied by a factor $\sqrt{E_b}$, where E_b answers energy of signal for one bit, T_b is period of one bit. The period T and time of one bit T_b are given by relation $T = mT_b$, m bit word. The other possibility is modification of basis QPSK in $\frac{\pi}{4}$ DQPSK (Differential Quadriphase (Quadrature) Shift Keying). It has two advantages: the information is hidden in phase change, which enables non-coherent receiving. Moreover, it limits effect of parasitic amplitude modulation. For nth symbol the phase is defined by relation [68]:

$$\phi(n) = \phi(n-1) + \Delta\phi(n), \tag{15}$$

where possible phase changes are $\Delta\phi(n) = \{\pi/4, -\pi/4, 3\pi/4, -3\pi/4\}$, which answers dibits {0 0, 0 1, 1 0, 1 1}.

4.2. Quadrature amplitude modulation (M-QAM)

This modulation combines the principle of phase and amplitude shift keying when each symbol is composed of several carrier periods and is determined by amplitude and phase. Plentifully, this modulation is above all used in radio technique with large orders M. It is also possible to look two independent amplitude modulations: in phase and quadrature part. Generally, it is possible to use two types of constellation diagrams: square or circle. Mathematically, the QAM signal can be written as [69]:

$$s_i(t) = \sqrt{\frac{2E_0}{T}} a_i \cos(2\pi f_c t) + \sqrt{\frac{2E_0}{T}} b_i \sin(2\pi f_c t), \qquad 0 \le t \le T, \tag{16}$$

where E_0 is energy of signal with the lowest amplitude, a_i, b_i are the integral number determine position of points in constellation diagram. It has been mentioned, M-QAM can be understood as two L-ASK modulations (in I a Q part), whereas $L = \sqrt{M}$. Position of points in constellation diagram with values can be expressed in matrix [69]:

$$\{a_i, b_i\} = \begin{pmatrix} (-L+1, L-1) & (-L+3, L-1) & \cdots & (L-1, L-1) \\ (-L+1, L-3) & (-L+3, L-3) & \cdots & (L-1, L-3) \\ \vdots & \vdots & & \vdots \\ (-L+1, -L+1) & (-L+3, -L+1) & \cdots & (L-1, -L+1) \end{pmatrix}. \tag{17}$$

4.3. Qualitative parameters of modulations

We have some parameters, which enables us to evaluate how the modulated optical wave was affected by negative effects from transmission environment. These parameters are Modulation Error Ratio (MER) and Error Vector Magnitude (EVM). Both these parameters are related to constellation diagram. In ideal constellation diagram there are only two ideal points. In real there are plenty of points around ideal point therefore the point seems to be spread, see Fig. 4.

4.3.1. Parameter MER

Parameter MER is defined as a ratio of sum of amplitude square of ideal symbol vectors to sum of amplitude square of error symbol vectors. This parameter is analog to SNR in digital modulated signal and it is usually expressed in dB unit. It could be seen in Fig. 4 [70]:

$$MER = \frac{\sum_{j=1}^{N} \left(\widetilde{I}_j^2 + \widetilde{Q}_j^2\right)}{\sum_{j=1}^{N} \left[(I_j - \widetilde{I}_j)^2 + (Q_j - \widetilde{Q}_j)^2\right]}, \tag{18}$$

where: $\widetilde{I}_j$ is component size of ideal symbol on axis I of constellation diagram, I_j is component size of real symbol on axis I of constellation diagram, $\widetilde{Q}_j$ is component size of ideal symbol on axis Q of constellation diagram, Q_j is component size of real symbol on axis Q of constellation diagram.

4.3.2. Parameter EVM

Parameter EVM defines distance between actually measured symbol vector and ideally symbol vector. EVM means Root Mean Square (RMS) of error values of separates states. The result can be also expressed in dB like MER, but more frequent is expression in % [70]:

$$EVM_{RMS} = \frac{\sqrt{\frac{1}{N}\left[(I_j - \widetilde{I}_j)^2 + (Q_j - \widetilde{Q}_j)^2\right]}}{s_{\max}^2} \cdot 100\ (\%), \tag{19}$$

where: $s_{\max}$ is amplitude of vector in constellation diagram, $\widetilde{I}_j$ is component size of ideal symbol on axis I of constellation diagram, I_j is component size of real symbol on axis I of constellation diagram, $\widetilde{Q}_j$ is component size of ideal symbol on axis Q of constellation diagram, Q_j is component size of real symbol on axis Q of constellation diagram.

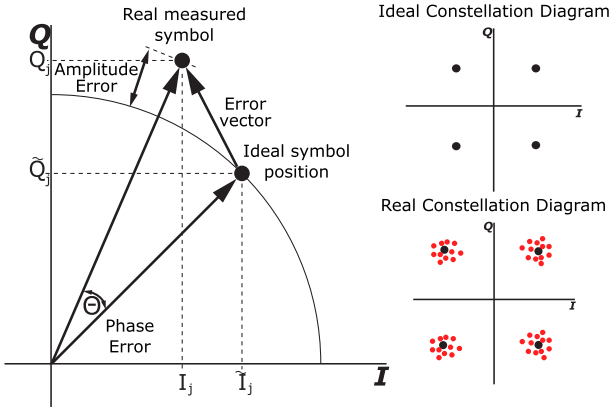

Fig. 4. Graphics representation of error vector [70].

5. Measurement results of rainfall simulation by the help of different nozzles on modulated optical beam evaluated by qualitative parameter MER

The measurement was performed according to the scheme shown in the Fig. 3. With the help of explanation analysis were are created graphs of the MER dependence on the different modulation formats and rainfall intensity (heavy, light, drizzle) for visual comparison.

Fig. 5 shows graph of PSK modulations according to rainfall type for valve opening 100%. From our performed experimental measurement, we have found that most significant influence on the communication quality had light rain for wavelength of 650 nm. It is caused by two effects, firstly, smaller sizes of water droplets during light rain, which scatter light beam with given wavelength more than rain with bigger droplets in case of other used jets. These results are corresponding with theoretical expectations, which are saying that electromagnetic wave is scattered more on obstacles with dimensions similar to used wavelength. Secondly it is necessary to take in to account that on smaller droplets is light beam more bended and deflected then in case of larger droplets. This effect causes for the part of light beam its deflection, thus power loss and communication parameters degradation. In our case it was observed by worsening of MER for different PSK modulation types during our experiment. It seems that wavelength 850 nm is more resistant. For the light rain, the most resistant modulation was $\frac{\pi}{4}$ DQPSK. Further were QPSK and 8PSK modulations. Modulation 16PSK reached the worst values. Heavy intensive rain had lower influence, MER values were steady for all modulations and also there is not a great difference between used wavelengths. Drizzle had the lowest influence. There was the best modulation QPSK and 8PSK and the worst was $\frac{\pi}{4}$ DQPSK, which was the most resistant on the contrary to previous two types of rainfalls.

Fig. 6 shows graph of QAM modulations according to the type of rainfall for valve opening 100%. The same like PSK modulations also there the wavelength 850 nm is less influenced than 650 nm. Also the light rain was the worst for QAM modulation. The most resistant was 4QAM modulation. Interesting is that 64QAM obtained better results than 16 and 32QAM. The most resistant was duly 4QAM and further according to account of states from lowest to highest.

Figs. 7 and 8 show results for valve opening 50%. The water flow decreases therefore the optical beam was less influenced and MER improved. The behaviours of modulations are comparable with results, which were obtained for valve opening 100%.

From the point of view of difference between reference state and heavy rain the lowest influence had 16QAM for 650 nm and QPSK for 850 nm and for light rain QPSK for 650 nm and 850 nm for 4QAM.

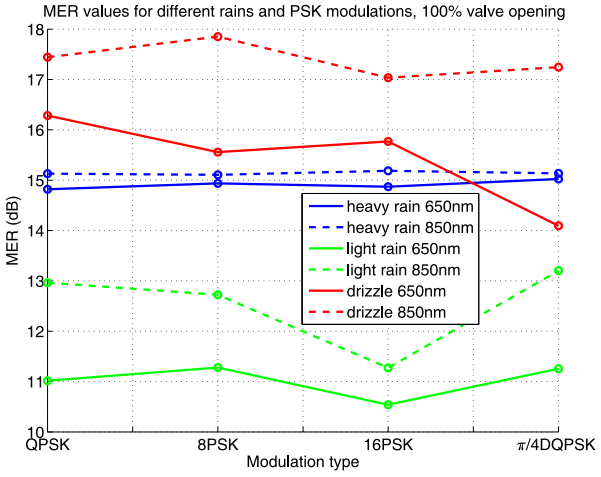

Fig. 5. MER according to rainfall type and modulation PSK, valve opening 100%.

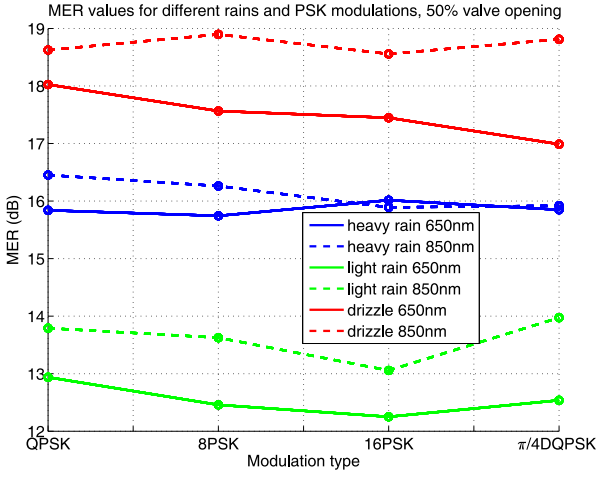

Fig. 7. MER according to rainfall type and modulation PSK, valve opening 50%.

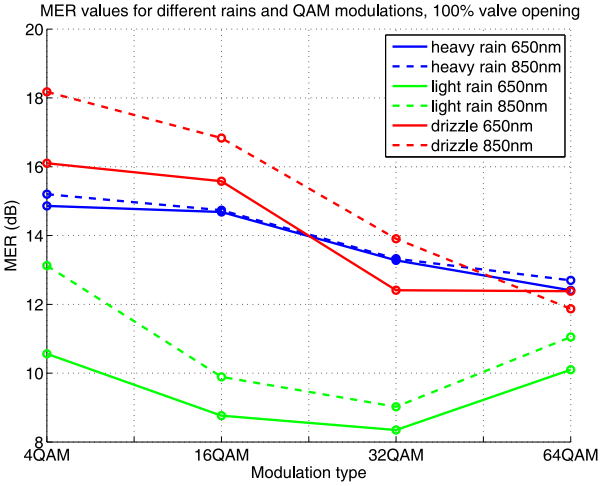

Fig. 6. MER according to rainfall type and modulation QAM, valve opening 100%.

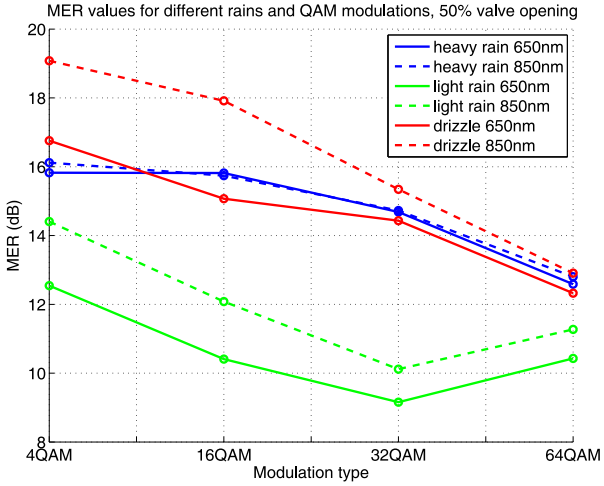

Fig. 8. MER according to rainfall type and modulation QAM, valve opening 50%.

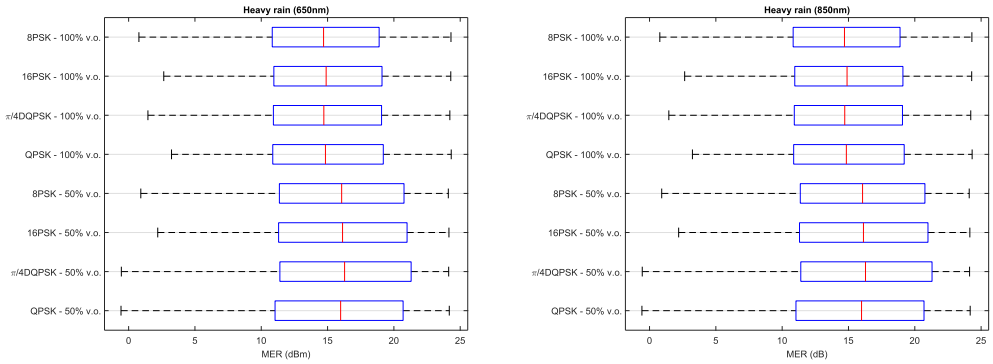

Fig. 9. Visualization of MER measured data through box diagram.

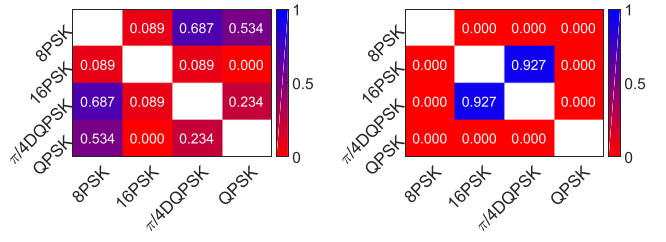

(a) Comparison of MER measured values for PSK modulations for valve opening 50% at wavelength 650 nm

(b) Comparison of MER measured values for PSK modulations for valve opening 50% at wavelength 850 nm

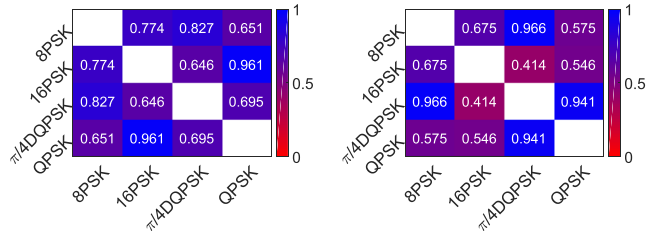

(c) Comparison of MER measured values for PSK modulations for valve opening 100% at wavelength 650 nm

(d) Comparison of MER measured values for PSK modulations for valve opening 100% at wavelength 850 nm

Fig. 10. Comparison of MER measured values for PSK modulations by statistical method ANOVA.

For drizzle deals the same as for light rain. The most influenced modulations were 32QAM and 64QAM. The best MER values were obtained for 650 nm and QPSK modulation. Further 8PSK, 16PSK and then 4QAM and $\frac{\pi}{4}$ DQPSK. According the results, PSK modulations are more resistant than QAM. The best for 850 nm was QAM modulation, further 8PSK, QPSK and $\frac{\pi}{4}$ DQPSK.

6. Statistical analysis

The following section deals with data analyse and description by the help of statistical methods. The basic visualization of measured data was done through box and whiskers plot for groups of measurements, which embody statistically significant dependence. Figs. 9–12 show MER resp. EVM measurements for wavelengths 650 nm and 850 nm. We used method Analysis of variance ANOVA for comparison of modulations, valve openings and wavelengths [71].

The result of the analyse was a finding that the statistically significant group was simulation of heavy rain. At first, the normality of data was tested in analyse. This test showed that in the data did not come from normal distribution in 95%. Further we tested a zero hypothesis of equality of mean values:

$$H_0 : \mu_1 = \mu_2, \quad H_A : \mu_1 \neq \mu_2 \tag{20}$$

The result is origin of dependence groups, which were further tested on equality of variance (data homoscedasticity):

$$H_0 : \sigma_1 = \sigma_2, \quad H_A : \sigma_1 \neq \sigma_2 \tag{21}$$

The measured data do not come from normal distribution we had to use non-parametric type of ANOVA, so-called Kruskall - Wallis test. For the groups of modulation formats, which embodied statistical equal, we can say that size of rainfall (Heavy rain, light rain and drizzle) has not any influence on quality of transmitted signal. In this case we did the Kolmogorov-Smirnov test for comparison of distribution of separate groups.

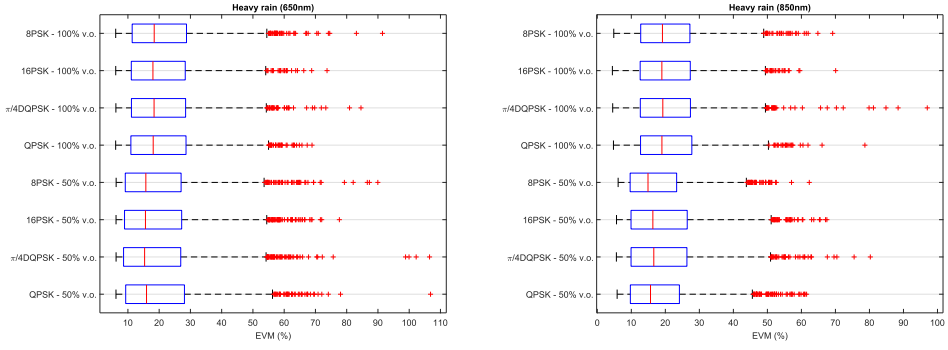

Fig. 11. Visualization of EVM measured data through box diagram.

(a) Comparison of EVM measured values for heavy rain, PSK modulations at wavelength 650 nm

(b) Comparison of EVM measured values for heavy rain, PSK modulations at wavelength 850 nm

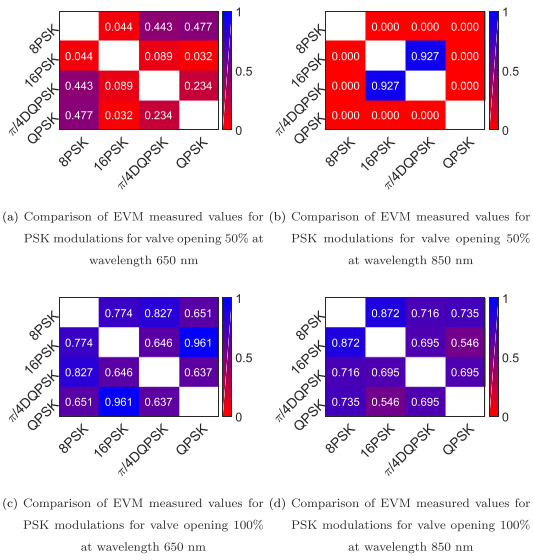

(a) Comparison of EVM measured values for PSK modulations for valve opening 50% at wavelength 650 nm

(b) Comparison of EVM measured values for PSK modulations for valve opening 50% at wavelength 850 nm

(c) Comparison of EVM measured values for PSK modulations for valve opening 100% at wavelength 650 nm

(d) Comparison of EVM measured values for PSK modulations for valve opening 100% at wavelength 850 nm

Fig. 12. Comparison of EVM measured values for PSK modulations by statistical method ANOVA.

Fig. 10(a)–(d) and Fig. 12(a)–(d) show comparison of modulation formats for Heavy rain. p-values given in constellation tables describe a congruency of distributions for separate modulation formats. It is obviously from the results that the best values were reached by valve opening 100%. By valve opening 50% the correlated values were very low or zero except several cases.

The results of EVM testing are comparable with MER testing. We can say according the results that the influence has the valve opening. The valve opening is related to pressure, which effect on nozzle, which determines size and distribution of rain drops. A similarity between groups was reached only in case of heavy rain for modulation format PSK (8PSK, 16PSK, QPSK and $\frac{\pi}{4}$ DQPSK). In case of QAM (4QAM, 8QAM, 16QAM, 32QAM and 64QAM) modulation formats we did not find any statistically significant agreement of measured data.

7. Conclusion and future work

Experimental measurements with different types of modulation formats were performed within the article to highlight the impact of simulated atmospheric rainfall phenomena on the free-space optical links. In addition to the modulation formats, rainfall parameters were also changed. The same basic parameters of modulation settings and measurement schemes were retained for the future comparison and correlation. Before the actual measurement of the rainfall influence on the free-space optical link, an experimental measurement of the raindrop size was made using one of the three nozzles used, namely 90B1FP1.0. A total of twenty drops were measured from the images, giving an average raindrop size of 460 μm, which then corresponds to the drizzle raindrop as it is smaller than 0.5 mm. This experimental measurement using a high-speed camera should point out the possibility of future droplet size measurements generated by simulation nozzles or similar devices that could eventually lead to the more accurate prediction of the attenuation due to the different droplet size, precipitation totals, or to develop new types of prediction models.

In the next part of the article, the attention was paid to free-space optical link operating at two selected wavelengths of 650 or 850 nm with several types of modulation formats namely QPSK, 8PSK, 16PSK, $\frac{\pi}{4}$ DQPSK, 4QAM, 16QAM, 32QAM and 64QAM and the verification of their properties such as MER, EVM and constellation diagrams against simulated rainfall. Several measurements were performed using three different types of nozzles simulating different types of precipitation total (drizzle, light and heavy rain) and their influence on modulated optical beam. The conclusions from these experimental measurements are of the following nature. For the simulated rainfall through the drizzle generating nozzle, the results are very similar to the rainfall simulated using a light rain nozzle. The durable types of modulations are those made up of fewer states with less risk of symbol interchange. On the contrary, the highest impact was on the 32QAM and 64QAM as expected. Averaging the resulting MER values from all three rain types, QPSK performed the best at the wavelength of 650 nm. The free-space optical link working at the wavelength of 850 nm it came out as the best 4QAM modulation.

For a deeper understanding of the rainfall, an amount of water and modulation formats influence, statistical analysis of the measured data was performed. After applying the statistical methods to the data, it was found that the greatest impact on the qualitative EVM and MER parameters of the modulation formats had a heavy rain. Also, it has been found that the water flow and the change of pressure had a significant effect on the quality of the communication through the EVM and MER parameters against all tested modulation formats for both chosen wavelengths. Major statistically significant changes between groups then have modulations with lesser states ie PSK (8PSK, 16PSK, QPSK and $\frac{\pi}{4}$ DQPSK). In the case of m-QAM modulation formats, no statistically significant difference was found.

In the future it would be also necessary to study different wavelengths e.g. 1550 nm, 1064 nm and their dependency on type of modulation format for communication including rainfall totals. Also, we want to focus on evaluation of other qualitative communication parameters such as Eb/No, SER, BER, SNR, CNR etc. as well. Our further aim is also testing the real-time services in form of real data transmission, video stream or voice, which have another qualitative parameters. In future we would like to deal with a deeper involvement of telecommunication technologies and a system for mutual operability and cooperation through 5G networks. Currently we can see strong development of Visible Light Communication into traffic systems (V2I, V2V, C2C C2I etc.) and traffic control (traffic lights, motorway light road sings, tunnel systems controls etc.). At border points of networks is under consideration utilization of different types of communication systems, which could be fibreless links working in near infrared area, which have short response and quick communication (bandwidth. [72] Other thing is also fact that 5G networks came with bit rates that reach 10 Gb s^{-1} or higher, therefore with increase of bit rates are connected also limits of accessible types of modulation formats and their dependencies on used communication technology. Processing of high-speed data streams is demanding for evaluation device that must be able to detect correct bit sequence in data traffic. This communication must be error-less as possible or with possibility of error corrections. Atmospheric phenomena that are dynamic and stochastic then have fundamental influence on free space types communication systems. Our proposed system can help with better understanding of rain rate influence on these communication links and with possible solutions of this inconvenience. However, it is generally known that FSO systems are sensitive on this atmospheric phenomenon whereas radio links are very sensitive on the droplets size and rain rate. Therefore, this problem is usually overcome by utilization of hybrid FSO/RF link.

Acknowledgement

We thank the two anonymous reviewers for their constructive comments, which helped us to improve the article. The research described in this article could be carried out thanks to the active support of the projects no. SP2017/79, SP2017/97, SP2018/117, SP2018/184, CZ.02.1.01/0.0/0.0/16019/0000867, VI20172019071, VI20152020008, TA03020439 and TA04021263. The work has been partially supported by Project No. CZ.1.07/2.3.00/20.0217.

References

[1] R. Ramirez-Iniguez, S.M. Idrus, Z. Sun, Optical Wireless Communications: IR for Wireless Connectivity, first ed., Auerbach Publications, 2008.
[2] S. Arnon, J. Barry, G. Karagiannidis, R. Schober, M. Uysal, Advanced Optical Wireless Communication Systems, first ed., Cambridge University Press, 2012.
[3] H. Henniger, O. Wilfert, An introduction to free-space optical communications, Radioengineering, 19 (2) (2011) 203–212. ISSN: 1805-9600.
[4] S. Hranilovic, Wireless Optical Communication Systems, first ed., Springer-Verlag, New York, 2005.
[5] Z. Ghassemlooy, W.O. Popoola, Terrestrial free-space optical communications, in: S. Ait Fares, F. Adachi (Eds.), Mobile and Wireless Communications Network Layer and Circuit Level Design, IN TECH, Rijeka, 2010, pp. 355–392, https://doi.org/10.5772/7698.
[6] X. Guoliang, X. Zhang, W. Junwei, F. Xiaoyong, Influence of atmospheric turbulence on FSO link performance, Optical Trans. Switch. Subsyst. (2004) 816–823, https://doi.org/10.1117/12.523470.
[7] A. Vats, H. Kaushal, Analysis of free space optical link in turbulent atmosphere, Optik-Int. J. Light Electron. Optic. 125 (12) (2014) 2776–2779, https://doi.org/10.1016/j.ijleo.2013.11.066.
[8] H. Henniger, B. Epple, D. Giggenbach, Mobil FSO activities in Europe and fading mitigation approaches, in: 17th International Conference Radioelektronika, IEEE, 2007, pp. 1–6, https://doi.org/10.1109/RADIO-ELEK.2007.371452.
[9] X. Yin, Z. Liu, P. Yue, Optical scintillations and fade statistics for FSO communications through moderate-to-strong non-Kolmogorov turbulence, Optic Laser. Technol. 47 (2013) 199–207, https://doi.org/10.1016/j.optlastec.2012.08.008.
[10] T. Plank, M. Czaputa, E. Leitgeb, S. Muhammad, N. Djaja, B. Hillbrand, P. Mandl, M. Schonhuber, Wavelength selection on FSO-links, in: Proceedings of the 5th European Conference on European Association on Antennas and Propagation, Antennas and Propagation (EUCAP), IEEE, 2011, pp. 2508–2512, ISBN: 9781457702501.
[11] I. Kim, E.J. Korevaar, Availability of free-space optics (FSO) and hybrid FSO/RF systems, Optical Wireless Communications IV (2001) 84–95, https://doi.org/10.1117/12.449800.
[12] A.K. Majumdar, J.C. Ricklin, Free-space Laser Communications, second ed., Springer-Verlag, New York, 2008.
[13] M.S. Awan, P. Brandl, E. Leitgeb, F. Nadeem, T. Plank, C. Capsoni, Results of an optical wireless ground link experiment in continental fog and dry snow conditions, in: 10th International Conference on Telecommunications, 2009, pp. 45–49.
[14] D. Kedar, S. Arnon, Urban optical wireless communication networks: the main challenges and possible solutions, IEEE Commun. Mag. 42 (5) (2004) S2–S7, https://doi.org/10.1109/MCOM.2004.1299334.
[15] S. Karp, R.M. Gagliardi, S.E. Moran, L.B. Stotts, Optical Channels: Fibers, Clouds, Water and the Atmosphere, Springer, 1988.
[16] S. Bloom, E. Korevaar, J. Schuster, H. Willebrand, Understanding the performance of free-space optics, J. Opt. Netw., 2 (6) (2003) 178–200. ISSN: 1943-0639.
[17] A. Akbulut, A practical approach to improve optical channel utilization period for hybrid FSO/RF systems, Adv. Electr. Electron. Eng. 12 (6) (2014) 599–603, https://doi.org/10.15598/aeee.v12i6.1234.
[18] A.K. Majumdar, J.C. Ricklin, Free-space Laser Communications: Principles and Advances, second ed., Springer-Verlag, New York, 2010.
[19] T.Y. Elganimi, Studying the BER performance, power-and bandwidth-efficiency for FSO communication systems under various modulation schemes, Jordan Appl. Electr. Eng. Comp. Technol. IEEE (2013) 1–6, https://doi.org/10.1109/AEECT.2013.6716426.
[20] N. Chand, J.J. Loriz, A.J. Hunton, B.M. Eteson, Performance comparison of NRZ and RZ modulations with and without forward error corrections for free-space optical communication, Free-Space Laser Communications V (2005) https://doi.org/10.1117/12.621393. 58920U-1–58920U-8.
[21] B. Barua, S.P. Majumder, Free space optical communication with OOK and BPSK modulation under different turbulent condition, in: International Conference on Informatics, Electronics and Vision, 2013, pp. 1–5, https://doi.org/10.1109/ICIEV.2013.6572720.
[22] A. Vanderka, L. Hajek, J. Latal, J. Vitasek, P. Koudelka, Design, simulation and testing of the OOK NRZ modulation format for free space optic communication in a simulation box, Adv. Electr. Electron. Eng. 12 (6) (2014) 604–616, https://doi.org/10.15598/aeee.v12i6.1255.
[23] W.O. Popoola, Z. Ghassemlooy, BPSK subcarrier intensity modulated free-space optical communications in atmospheric turbulence, J. Lightwave Technol. 27 (8) (2009) 967–973, https://doi.org/10.1109/JLT.2008.2004950.
[24] K. Prabu, D.S. Kumar, T. Srinivas, Performance analysis of FSO links under strong atmospheric turbulence conditions using various modulation schemes, Optik-Int. J. Light Electron. Optic. 125 (19) (2014) 5573–5581, https://doi.org/10.1016/j.ijleo.2014.07.028.
[25] J. Li, J.Q. Liu, D.P. Taylor, Optical communication using subcarrier PSK intensity modulation through atmospheric turbulence channels, IEEE Trans. Commun. 55 (8) (2007) 1598–1606, https://doi.org/10.1109/TCOMM.2007.902592.
[26] T. Ohtsuki, Multiple-subcarrier modulation in optical wireless communications, IEEE Commun. Mag. 41 (3) (2003) 74–79, https://doi.org/10.1109/MCOM.2003.1186548.
[27] W. Huang, J. Takayanagi, T. Sakanaka, M. Nakagawa, Atmospheric optical communication system using subcarrier PSK modulation, in: International Conference on Communications, IEEE, 1993, pp. 1597–1601, https://doi.org/10.1109/ICC.1993.397553.
[28] Z. Chen, S. Yu, T. Wang, G. Wu, H. Guo, W. Gu, Spatial correlation for transmitters in spatial MIMO optical wireless links with Gaussian-beam waves and aperture effects, Optic Commun. 287 (2013) 1218, https://doi.org/10.1016/j.optcom.2012.09.022.
[29] W.O. Popoola, et al., Error performance of terrestrial free space optical links with subcarrier time diversity, Commun. IET 6 (5) (2012) 499–506.
[30] K. Kiasaleh, Performance of APD-based, PPM free-space optical communication systems in atmospheric turbulence, IEEE Trans. Commun. 53 (9) (2005) 1455–1461, https://doi.org/10.1109/TCOMM.2005.855009.
[31] X. Liu, S. Chandrasekhar, T.H. Wood, R.W. Tkach, P.J. Winzer, E.C. Burrows, A.R. Chraplyvy, M-ary pulse- position modulation and frequency shift keying with additional polarization/phase modulation for high-sensitivity optical transmission, Optic Express 19 (26) (2011) B868–B881, https://doi.org/10.1364/OE.19.00B868.
[32] H. Selmy, H.M.H. Shalaby, Z.I. Kawasaki, Proposal, Performance, Evaluation of a hybrid BPSK-modified MPPM technique for optical fiber communications systems, J. Lightwave Technol. 31 (22) (2013) 3535–3545, https://doi.org/10.1109/JLT.2013.2284605.
[33] M. Karlsson, E. Agrell, Multilevel pulse-position modulation for optical power-efficient communication, Optic Express 19 (26) (2011) B799–B804, https://doi.org/10.1364/OE.19.00B799.
[34] M. Sjodin, P. Johannisson, H. Wymeersch, P.A. Andrekson, M. Karlsson, Comparison of polarization-switched QPSK and polarization-multiplexed QPSK at 30 Gbit/s, Optic Express 19 (8) (2011) 7839–7846, https://doi.org/10.1364/OE.19.007839.
[35] S. Wenxiao, W. Pengxia, Wei Liu, Hybrid polarization-division-multiplexed quadrature phase-shift keying and multi-pulse pulse position modulation for free space optical communication, Optic Commun. 334 (2015) 63–73, https://doi.org/10.1016/j.optcom.2014.08.015.
[36] A. Vats, H. Kaushal, Analysis of free space optical link in turbulent atmosphere, Optik 125 (12) (2014) 2776–2779, https://doi.org/10.1016/j.ijleo.2013.11.066.
[37] R.L. Fante, Electromagnetic beam propagation in turbulent media, Proc. IEEE 63 (12) (1975) 1669–1692, https://doi.org/10.1109/PROC.1975.10035.
[38] J.W. Strohbehn, Line-of-sight wave propagation through the turbulent atmosphere, Proc. IEEE 56 (8) (1968) 1301–1318, https://doi.org/10.1109/PROC.1968.6572.
[39] S.F. Clifford, G.R. Ochs, R.S. Lawrence, Saturation of optical scintillation by strong turbulence, J. Opt. Soc. Am. 64 (2) (1974) 148–154, https://doi.org/10.1364/JOSA.64.000148.
[40] A.M. Prokhorov, F.V. Bunkin, K.S. Gochelashvily, V.I. Shishov, Laser irradiance propagation in turbulent media, Proc. IEEE 63 (5) (1975) 790–811, https://doi.org/10.1109/PROC.1975.9828.
[41] J.W. Strohbehn, Laser Beam Propagation in the Atmosphere, first ed., Springer, Berlin, 1978.
[42] R.L. Fante, Electromagnetic beam propagation in turbulent media: an update, Proc. IEEE 68 (11) (1980) 1424–1443, https://doi.org/10.1109/PROC.1980.11882.
[43] J.H. Churnside, Aperture averaging of optical scintillations in the turbulent atmosphere, Appl. Optic. 30 (15) (1991) 1982–1994, https://doi.org/10.1364/AO.30.001982.
[44] I.I. Kim, H. Hakakha, P. Adhikari, E. Korevaar, A.K. Majumdar, Scintillation reduction using multiple transmitters, Free-Space Laser Commun. Technol. IX (2990) (1997) 102–113, https://doi.org/10.1117/12.273685.
[45] T. Landolsi, A.F. Elrefaie, Performance of single and dual-polarized optically preamplified M-ary PPM systems with finite extinction ratios over FSO fading channels, Optic Commun. 367 (2016) 316–324, https://doi.org/10.1016/j.optcom.2016.01.064.
[46] K. Prabu, D.S. Kumar, R. Malekian, BER analysis of BPSK-SIM-based SISO and MIMO FSO systems in strong turbulence with pointing errors, Optik - Int. J. Light Electron. Optic. 125 (21) (2014) 6413–6417, https://doi.org/10.1016/j.ijleo.2014.08.006.
[47] S. Chaudhary, A. Amphawan, K. Nisar, Realization of free space optics with OFDM under atmospheric turbulence, Optik - Int. J. Light Electron. Optic. 125 (18) (2014) 5196–5198, https://doi.org/10.1016/j.ijleo.2014.05.036.
[48] W.O. Popoola, Z. Ghassemlooy, E. Leitgeb, Free-space Optical Communication in Atmospheric Turbulence Using DPSK Subcarrier Modulation, 2007.
[49] N. Kumar, A.L.J. Teixeira, 10 Gbit/s OFDM based FSO communication system using M-QAM modulation with enhanced detection, Opt. Quant. Electron. 48 (1) (2016) 1–7, https://doi.org/10.1007/s11082-015-0272-5.
[50] J. Libich, S. Zvanovec, Influences of turbulences in near vicinity of buildings on free-space optical links, IET microwaves, Antenn. Propagat. 5 (9) (2011) 1039–1044, https://doi.org/10.1049/iet-map.2010.0630.
[51] J. Perez, Z. Ghassemlooy, S. Rajbhandari, M. Ijaz, H.L. Minh, Ethernet FSO communications link performance study under a controlled fog environment, IEEE Commun. Lett. 16 (3) (2012) 408–410, https://doi.org/10.1109/LCOMM.2012.012412.112072.
[52] Z.N. Chaleshtory, A. Gholami, Z. Ghassemlooy, M. Sedghi, Experimental investigation of environment effects on the FSO link with turbulence, IEEE Photon. Technol. Lett., ISSN: 1041-1135 29 (17) (2017) 1435–1438, https://doi.org/10.1109/LPT.2017.2723569.
[53] N. Badar, R.K. Jha, Performance comparison of various modulation schemes over free space optical (FSO) link employing Gamma-Gamma fading model, Opt. Quant. Electron. 49 (5) (2017) 1–10, https://doi.org/10.1007/s11082-017-1025-4.
[54] M. Achour, Simulating atmospheric free-space optical propagation: rainfall attenuation, in: Proceedings of SPIE 4635, Free-space Laser Communication Technologies, XIV, 2002, pp. 192–201, https://doi.org/10.1117/12.464100.

[55] F.H. Mustafa, A.S.M. Supaat, N. Charde, Effect of rain attenuations on free space optic transmission in Kuala Lumpur, Int. J. Adv. Sci. Eng. Inf. Technol. 1 (4) (2011) 337–341, https://doi.org/10.18517/ijaseit.1.4.70.
[56] S.A. Zabidi, I.M. Rafiqul, W. Al-Khateeb, A.W. Naji, Analysis of rain effects on terrestrial free space optics based on data measured in tropical climate, IIUM Eng. J., ISSN: 1511-788X 12 (5) (2011) 45–51.
[57] V. Brazda, V. Schejbal, O. Fiser, Rain impact on FSO link attenuation based on theory and measurement, in: 6th European Conference on Antennas and Propagation (EUCAP), Prague, 2012, pp. 1239–1243, https://doi.org/10.1109/EuCAP.2012.6206120.
[58] S. Zvanovec, Diversity statistics of free space optical links affected by rain, Piers Online, ISSN: 1931-7360 7 (7) (2011) 637–640.
[59] P. Singh, M.L. Singh, Experimental determination and comparison of rain attenuation in free space optic link operating at 532 nm and 655 nm wavelength, Optik - Int. J. Light Electron. Optic. 125 (17) (2014) 4599–4602, https://doi.org/10.1016/j.ijleo.2014.04.096.
[60] F. Rashidi, J. He, L. Chen, Spectrum slicing WDM for FSO communication systems under the heavy rain weather, Optic Commun. 387 (2017) 296–302, https://doi.org/10.1016/j.optcom.2016.11.070.
[61] A.G. Alkholidi, K.S. Altowij, Free space optical communications - theory and practices, in: Contemporary Issues in Wireless Communications, Rijeka, 2014, pp. 160–212, https://doi.org/10.5772/58884.
[62] S.S. Muhammad, P. Kohldorfer, E. Leitgeb, Channel modeling for terrestrial free space optical links, in: Proceedings of 7th International Conference Transparent Optical Networks, IEEE, 2005, pp. 407–410, https://doi.org/10.1109/ICTON.2005.1505832.
[63] S.A. Zabidi, I.M. Rafiqul, A.K. Wajdi, Rain attenuation prediction of optical wireless system in tropical region, in: IEEE International Conference on Smart Instrumentation, Measurement and Applications (ICSIMA), IEEE, 2013, pp. 1–5, https://doi.org/10.1109/ICSIMA.2013.6717965.
[64] ITU-R P.838–2, R, Specific Attenuation Model for Rain for Use in Prediction Methods, 2003.
[65] S. Ishii, S. Sayama, K. Mizutani, Rain attenuation at Terahertz, Wireless Eng. Technol. 1 (2) (2010) 92–95, https://doi.org/10.4236/wet.2010.12014.
[66] P. Pechac, S. Zvanovec, Zaklady sireni vln pro planovani pozemnich radiovych spoju, 2007, ISBN: 978-80-7300-223-7.
[67] Thorlabs PDA10A-EC, https://www.thorlabs.de/newgrouppage9.cfm?objectgroup_id=3257&pn=PDA10A-EC.
[68] A.K. Majumdar, Advanced Free Space Optics (FSO), first ed., Springer-Verlag, New York, 2014.
[69] W.T. Webb, Modern Quadrature Amplitude Modulation: Principles and Applications for Fixed and Wireless Channels, IEEE Press Piscataway, 1995.
[70] National Instruments, Modulation Error Ratio (MER) and Error Vector Magnitude (EVM). http://www.ni.com/white-paper/3652/en/.
[71] Inc StatSoft, Electronic Statistics Textbook, StatSoft, Tulsa, 2013. http://www.statsoft.com.
[72] Z. Huang, et al., Hybrid optical wireless network for future SAGO-integrated communication based on FSO/VLC heterogeneous interconnection, IEEE Photon. J. 9 (2) (2017) 1–10, https://doi.org/10.1109/JPHOT.2017.2655004.

Applied Geography 107 (2019) 82–90

Contents lists available at ScienceDirect

Applied Geography

journal homepage: www.elsevier.com/locate/apgeog

A detailed spatiotemporal analysis of traffic crash hotspots

Michal Bíl*, Richard Andrášik, Jiří Sedoník

CDV – Transport Research Centre, Lisenska 33a, 636 00, Brno,Czech Republic

ARTICLE INFO

Keywords:
Traffic crash
Hotspot
Kernel density estimation
KDE+
Road network
Spatiotemporal analysis

ABSTRACT

A number of traffic crash databases at present contain the precise positions and dates of these events. This feature allows for detailed spatiotemporal analysis of traffic crash patterns.

We applied a clustering method for identification of traffic crash hotspots to the rural parts of primary roads in the Czech road network (3,933 km) where 55,296 traffic crashes occurred over 2010 – 2018. The data were analyzed using a 3-year time window which moved forward with a one-day step as an elementary temporal resolution. The spatiotemporal behavior of hotspots could therefore be analyzed in great detail.

All the identified hotspots, during the monitored nine-year period, covered between 6.8% and 8.2% of the entire road network length in question. The percentage of traffic crashes within the hotspots remained stable over time at approximately 50%. Three elementary types of hotspots were identified when analyzing spatiotemporal crash patterns: hotspot emergence, stability and disappearance. Only 100 hotspots were stable (remained in approximately the same position) over the entire nine-year period. This approach can be applied to any traffic-crash time series when the precise positions and date of crashes are available.

1. Introduction

Traffic crashes and the related injuries and fatalities pose a safety issue across the globe (WHO, 2015). Researchers are focusing on identification of factors causing traffic crashes, as well as identification of places where crashes occur more frequently than elsewhere. Geographic information systems play an important role in these activities (Steenberghen, Dufays, Thomas, & Flahaut, 2004).

Databases of traffic crashes at present usually contain precise (GPS) locations which make studying their spatial distribution possible (e.g., Gundoglu, 2010; Li, Zhu, & Sui, 2007). A number of approaches have been developed recently to study spatial distribution of crashes. We focused here on a method based on Kernel Density Estimation (KDE) (Silverman, 1986, p. 176) which overcomes the need for spatial aggregation of crash data and is able to identify spatial clustering along roads. Statistically significant clusters (e.g., Bíl, Andrášik, & Janoška, 2013) usually represent traffic crash hotspots (Elvik, 2008). These places are of a great interest to traffic engineers, road administrators and traffic-safety researchers, but also to drivers. The KDE method, or its modifications, has already been applied a number of times to traffic crash data (e.g., Anderson, 2009; Bíl et al., 2013; Dai & Jaworski, 2016; Erdogan, Yilmaz, Baybura, & Gullu, 2008; Xie & Yan, 2008).

1.1. Spatial and temporal analyses of crash data

Spatial and temporal dimensions of crashes were often investigated separately. Temporal parts of crashes were visualized using crash time-series or on graphs, where months and hours of crashes were displayed (e.g., Rodríguez-Morales, Díaz-Varela, & Marey-Pérez, 2013) or spider plots to visualize intraday crash variability (e.g., Plug, Xia, & Caulfield, 2011). Hotspots were often computed for a time-series available with no consideration of their temporal evolution. The primary reason for this was a lack of time-series of a sufficient length.

Only a limited number of studies have considered both the spatial and temporal dimensions of traffic crash data, e.g. Liu and Sharma (2017) investigated the temporal evolution of fatal crashes in order to identify long-term regional trends in the change of traffic crash frequencies in Iowa (USA) for the respective counties. Kingham, Sabel, and Bartie (2011) studied temporal evolution and spatial clustering of road traffic accidents, aggregated to census area units, in Christchurch (New Zealand) related to school travel of children between 1980 and 2004.

Hotspots, as places within individual roads, were often computed on a yearly basis, allowing thus a comparison of hotspot patterns among the respective years (e.g., Kaygisiz, Düzgün, Yildiz, & Senbil, 2015; Olsen, Mitchell, Ogilvie, & on behalf of the M74 study team, 2017) or within a day (Plug et al., 2011). These approaches are sufficient in many cases, but sometimes a more detailed temporal segmentation can

* Corresponding author.
E-mail address: michal.bil@cdv.cz (M. Bíl).

https://doi.org/10.1016/j.apgeog.2019.04.008
Received 22 August 2018; Received in revised form 28 February 2019; Accepted 18 April 2019
Available online 09 May 2019

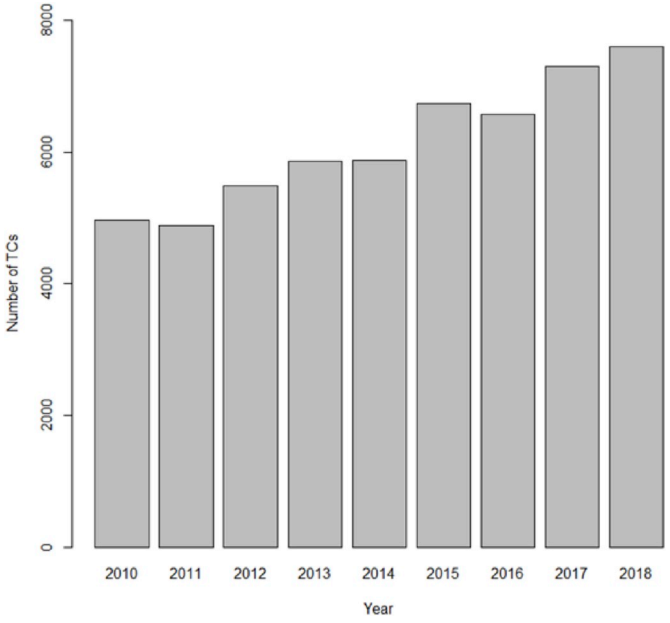

Fig. 1. Number of traffic crashes (TCs) on primary roads registered by the Police in period 2010–2018.

be requested. The above-mentioned standard approaches would be, however, too computationally demanding when a more flexible temporal segmentation is requested.

The aim of this study is to present an approach for a detail spatio-temporal analysis of traffic crash hotspots. We analyzed traffic crashes which occurred on rural parts of primary roads in the Czech road network (3933 km) between 2010 and 2018. We applied the KDE+ clustering method which allowed us to identify both the spatial crash pattern along the individual road segments and three basic forms of hotspot temporal behavior: emergence, stability and disappearance. We also present, on selected road segments, typical cases of all three elementary hotspot patterns.

2. Data

Traffic crashes (55,296 records) from the database of Police, which took place on rural parts of the primary roads in the Czech Republic between 2010 and 2018, were analyzed in this study (Fig. 1). The road network was split at intersections into 2908 road segments, as we focused merely on detecting and analyzing hotspot patterns outside intersections. The overall length of these segments was 3933 km. There were 2701 (93%) between-intersection segments with at least one crash within the period in question.

3. Methods

3.1. KDE+ clustering method

The KDE+ method is an approach which currently assists researchers and road administrators in many countries in rapid identification of the most hazardous places within transportation networks (Bíl, Andrášik, Nezval, & Bílová, 2017, 2019, 2013; Alberta Wildlife Watch, 2017; Bartonička, Andrášik, Duľa, Sedoník, & Bíl, 2018; Favilli et al., 2018; Heigl, Horvath, Laaha, & Zahler, 2017; Périquet at al., 2018; Sjölund, 2016). All the data needed for this kind of analysis are the positions of the crashes along the road segments and the lengths of the respective road segments or GIS layers of both crashes and the

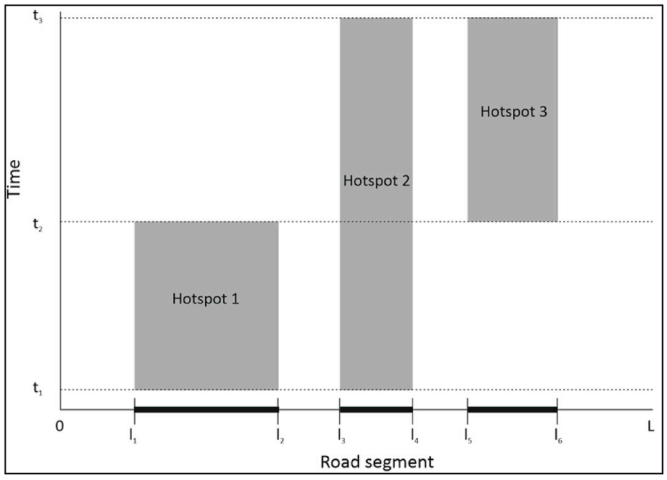

Fig. 2. A sketch of the three elementary forms of hotspots in relation to their temporal behavior: disappearance (hotspot 1, h1), stability (h2) and emergence (h3).

respective roads. Additional information on the crash type (e.g., single-vehicle crash, etc.) and crash consequences (e.g., without injuries, fatal crashes, etc.) can also be considered in the analysis, but they are not necessary if only a general crash pattern overview is the primary aim of the study.

The KDE+ method is based on the standard kernel density estimation approach enriched by statistical tests of cluster significance. The KDE+ produces a relative measure, cluster strength, by which it is possible to rank the hotspots prioritizing the most hazardous ones. The cluster strength is directly connected to the number of records (crashes) in a cluster and the length of a road section, and indirectly related to the number of other records (located out of the cluster) and the length of the cluster. A comparison of the KDE+ method with other methods, currently used for the same purpose, was published in Bíl et al. (2013). The KDE+ toolbox for ArcGIS (Bíl et al., 2018) or standalone JAVA app (Bíl, Andrášik, Svoboda, & Sedoník, 2016), can be downloaded free of charge from www.kdeplus.cz.

3.2. Temporal evolution of hotspots

Three elementary forms of hotspots, in terms of their temporal behavior, can be defined (Fig. 2): The first one (Hotspot 1) indicates a hotspot which is only present between time 1 (t_1) and 2 (t_2). It consequently disappears. Another form of hotspot exists over the entire period (Hotspot 2), i.e. between t_1 and t_3. The last elementary form is Hotspot 3, which emerges at t_2 and then endures over the rest of the period ($t_2 - t_3$). These three very basic types of hotspots reflect the following safety conditions along roads:

- Hotspot 1 indicates places where a safety measure was successfully applied in t_2 or traffic conditions changed substantially (e.g., a drop in traffic flow due to a newly built road),
- Hotspot 2 indicates dangerous places with no or unsuccessfully applied safety measures,
- Hotspot 3 indicates a place on a road segment where safety conditions worsened in comparison with the previous period.

There can also be identified other types of hotspot temporal patterns, as combinations of the above-mentioned (e.g., a hotspots which emerges and disappears several times or moves along a road segment), but for the sake of simplicity, we only focused on these three elementary ones.

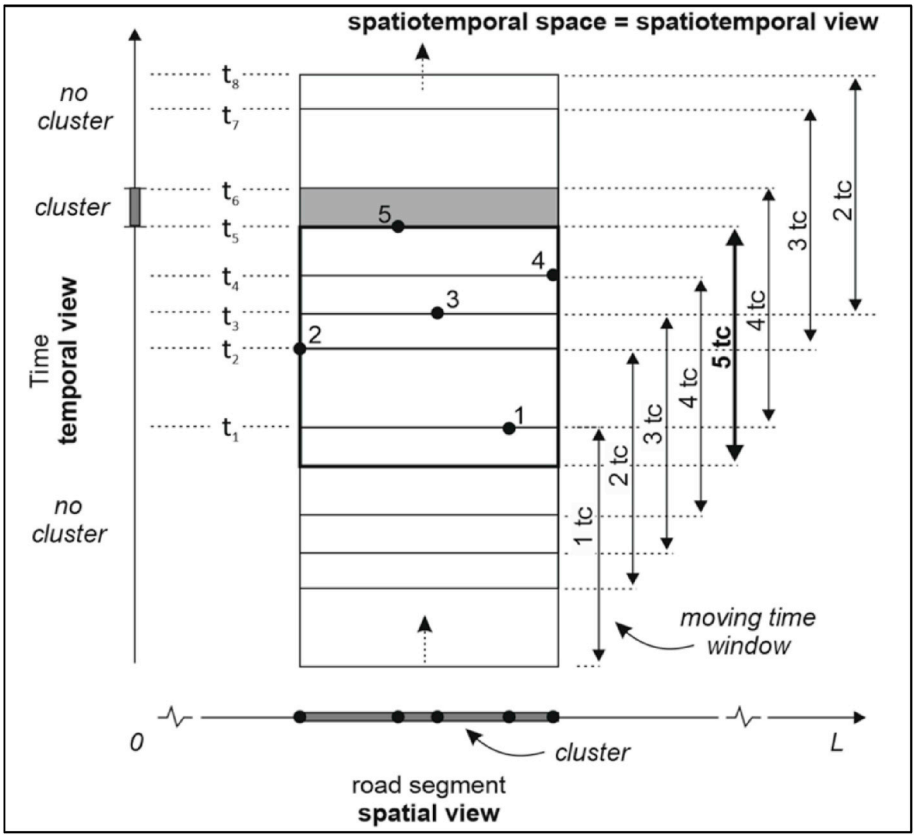

Fig. 3. An example of spatiotemporal analysis using the KDE+ method (STKDE+) and a temporal moving window. The spatial position of the hotspot was maintained as stable here, but it can also move.

3.3. Construction of a moving window for analyses of clustering over time

The core part of this contribution is the application of a moving window when KDE+ clustering is consecutively computed in a number of recurrent steps throughout the entire time series. This automatic and objective procedure for spatiotemporal analysis of traffic crashes reduces the subjectivity of defining temporal and spatial segments and, at the same time, increases the accuracy of such analysis as much as possible. The KDE+ method can be run every day in order to obtain a complete view of the traffic crash pattern from both spatial and temporal perspectives. An actual list of hotspots can thus be received at any time within the time period in question. The results can be depicted in a two-dimensional spatiotemporal graph (see Fig. 3) highlighting the hotspot.

Let us imagine the time window for which the clustering is computed. The first position of the window is placed when a first traffic crash occurred (Figs. 3 and 1). At this time the overall number of traffic crashes in this window is also one. Then the window is moved forward with a one day step. Let us assume, for the sake of simplicity, that 5 crashes will form a hotspot. The bold solid lines will then represent the position of the time window when 5 traffic crashes (TC) were present within the selected time interval (from t_5 to t_6). Less than 5 TC occurred in other time intervals and therefore no other hotspots were detected.

Table 1
Clustering results obtained using a three-year window for all traffic crashes which occurred on the Czech primary roads network between 2010 and 2018.

	10–12	11–13	12–14	13–15	14–16	15–17	16–18
No of hotspots	2242	2362	2369	2434	2482	2491	2561
Overall length [km]	266	274	283	296	303	307	323
Overall length [%]	6.8	7.0	7.2	7.5	7.7	7.8	8.2
No of TC within hotspots	7315	7775	8140	8719	9092	9417	9990
No of TC within hotspots [%]	47.7	47.9	47.3	47.2	47.3	45.6	46.5

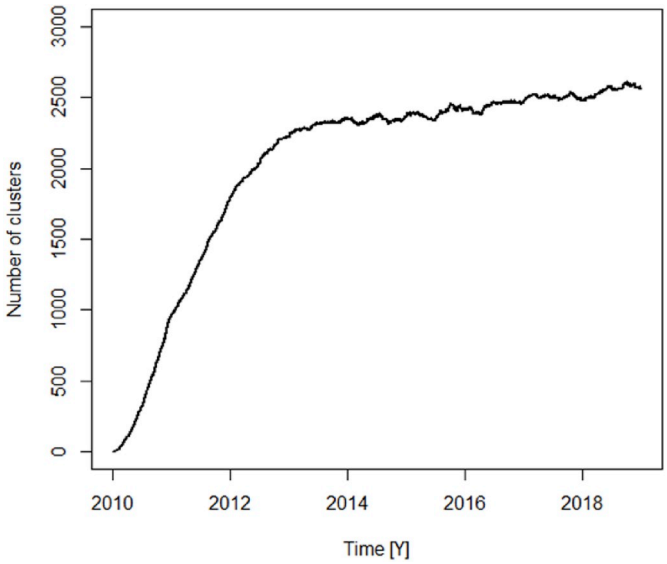

Fig. 4. Number of hotspots on the rural parts of first road class each day over the entire period 2010–2018.

3.4. An algorithm for the spatiotemporal analysis

The algorithm for the spatiotemporal analysis of traffic crashes can be symbolically described as follows:

```
STKDE+ algorithm
  input: road network, data on TCs, time range T = [T1, T2], window width w
  output:graphical representation of clusters in spatiotemporal space
  for each road segment in road network do
    plot a new graph
    for each day in T do
      subTCs ← subset TCs according to time period [day – w, day] and road segment
      clusters ← run the KDE+ method with subTCs
      plot clusters (x-axis) at day (y-axis) into the graph
    end
    save the graph
  end
```

TCs – traffic crashes.

Although the spatiotemporal KDE+ (STKDE+) algorithm is straightforward and easily understandable, it is not suitable for practical use. It would be time-demanding to run the KDE+ method every day. Since the following algorithm launches the KDE+ method only when the set of crashes changes, it is more effective than the straight forward implementation of the STKDE + algorithm above.

```
Effective implementation of the STKDE+ algorithm
  input: data on TCs, time range T = [T1, T2], window width w
  output:graphical representation of clusters in spatiotemporal space
  for each road segment in road network do
    day ← date of a TC (from TCs) which occurred the second* on the selected road
    segment
    plot a new graph
    while day ≤ T2 do
      subTCs ← subset TCs according to time period [day – w, day] and road segment
      clusters ← run the KDE+ method with subTCs
      shift ← 0
      while there is no change in subTCs do
        day ← day + 1
        shift ← shift + 1
        subTCs ← subset TCs according to time period [day – w, day]
      end
      plot clusters (x-axis) at [day – shift, day] (y-axis) into the resulting graph
    end
    save the graph
  end
```

*A single TC cannot form a cluster. Therefore, the analysis starts when the second TC enters the analysis.

It took approximately 12 h to run the entire spatiotemporal analysis for the Czech primary roads network consisting of 2908 between-intersection segments. Computations were performed in R 3.4.2 (R Core Team, 2014) on PC Intel Core i7 (2.7 GHz) with 8 GB RAM.

4. Results

4.1. General overview

Table 1 presents an overview of hotspot statistics for seven periods (3-year time window). Crashes within the hotpots represented almost 50% of all crashes and were concentrated within 6.8–8.2% of the road network length. Only 100 hotspots were stable for the entire period 2010–2018 (9 years). They represent dangerous locations within the road network which persisted over the long run.

4.2. Detailed view

Table 1 only approximately describes the results as the time was segmented there into respective years. The proposed spatiotemporal approach allows for one day time step, however, and therefore a more detailed temporal overview can be obtained (see Fig. 4 and Fig. 5). The number of clusters over the entire period can be computed for each day.

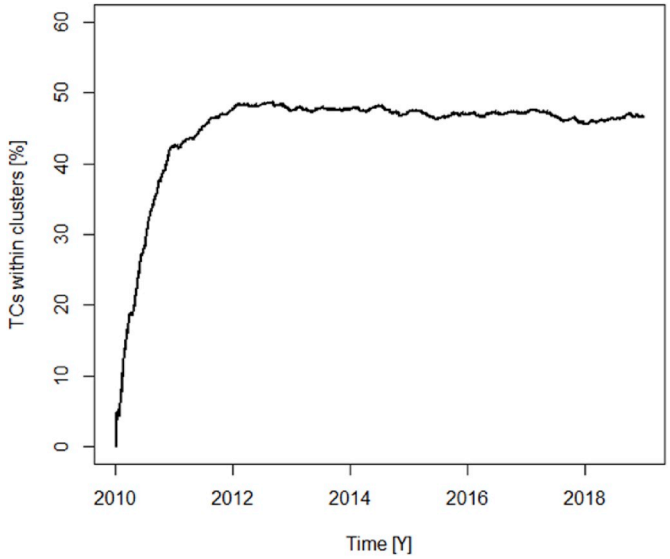

Fig. 5. Percentage of TCs within hotspots on the rural parts of first road class on each day over the entire period 2010–2018.

A steep increase in the number of clusters can be observed at the beginning of the time series (Fig. 4, between 2010 and 2013). This was caused by the fact that the time window starts on the date of the first traffic crash (see Fig. 2 moving window at t_1), i.e., it starts with only one crash and moves forward when the sum of crashes changes. Afterwards, the number of clusters steadily increased from 2369 to 2561 (see Fig. 4). This trend reflects the same trend in the overall number of crashes (see Fig. 1).

The ratio of crashes in clusters to all crashes can also be displayed for each day (Fig. 5). The percentage of crashes within the clusters remains stable as of 1 Jan 2012 (Fig. 5). In average, there were 47.2% of crashes within the clusters. The standard deviation accounts for only 0.7%. It is worth mentioning that the percentage of crashes within the clusters seems to be independent from the increasing (or decreasing) number of TCs entering the analysis (compare with Fig. 1). This means that the spatial pattern remains consistent.

4.3. Specific examples of the three elementary hotspots types

Below we demonstrate, using several current examples from the analyzed data, three elementary hotspots types in terms of their spatiotemporal behavior. All the following 8 examples of hotspots can also be viewed on the supplementary KML file.

4.3.1. Hotspot disappearance

The first example is a hotspots disappearance (see Hotspot 1 in Fig. 2, left side). This situation occurred at road segment no. 16935 (Fig. 6) where a hotspot was detected between 2010 and 2013. “No overtaking” traffic signs (white lines) were placed at that location in 2013. The hotspot consequently disappeared. Hotspot disappearance was also detected after the installation of a warning sign (Fig. 7) or as a result of the above-mentioned or more complex safety measures (Fig. 8).

4.3.2. Hotspot emergence

Hotspots also emerge as a result of sudden worsening of traffic conditions. Fig. 9 presents such a case when part of a new bypass was

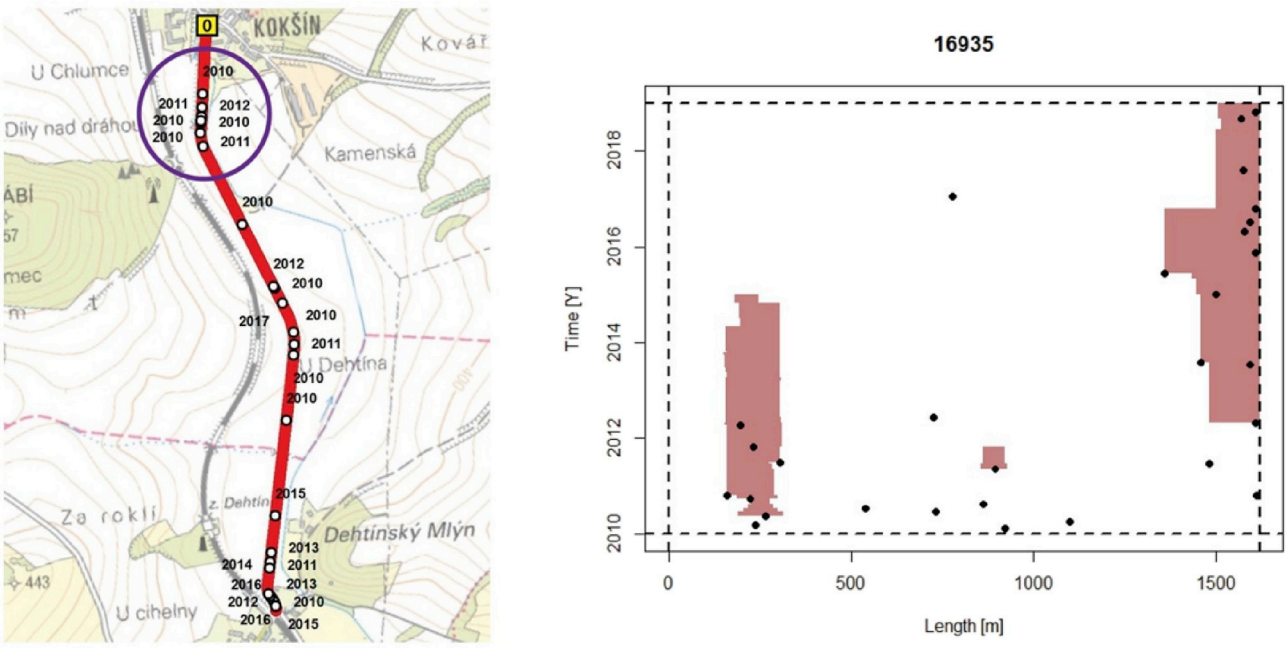

Fig. 6. A map depicting the road and the respective crashes together with the spatiotemporal (ST) graph of traffic crash pattern and hotspots on a road segment no. 16935.

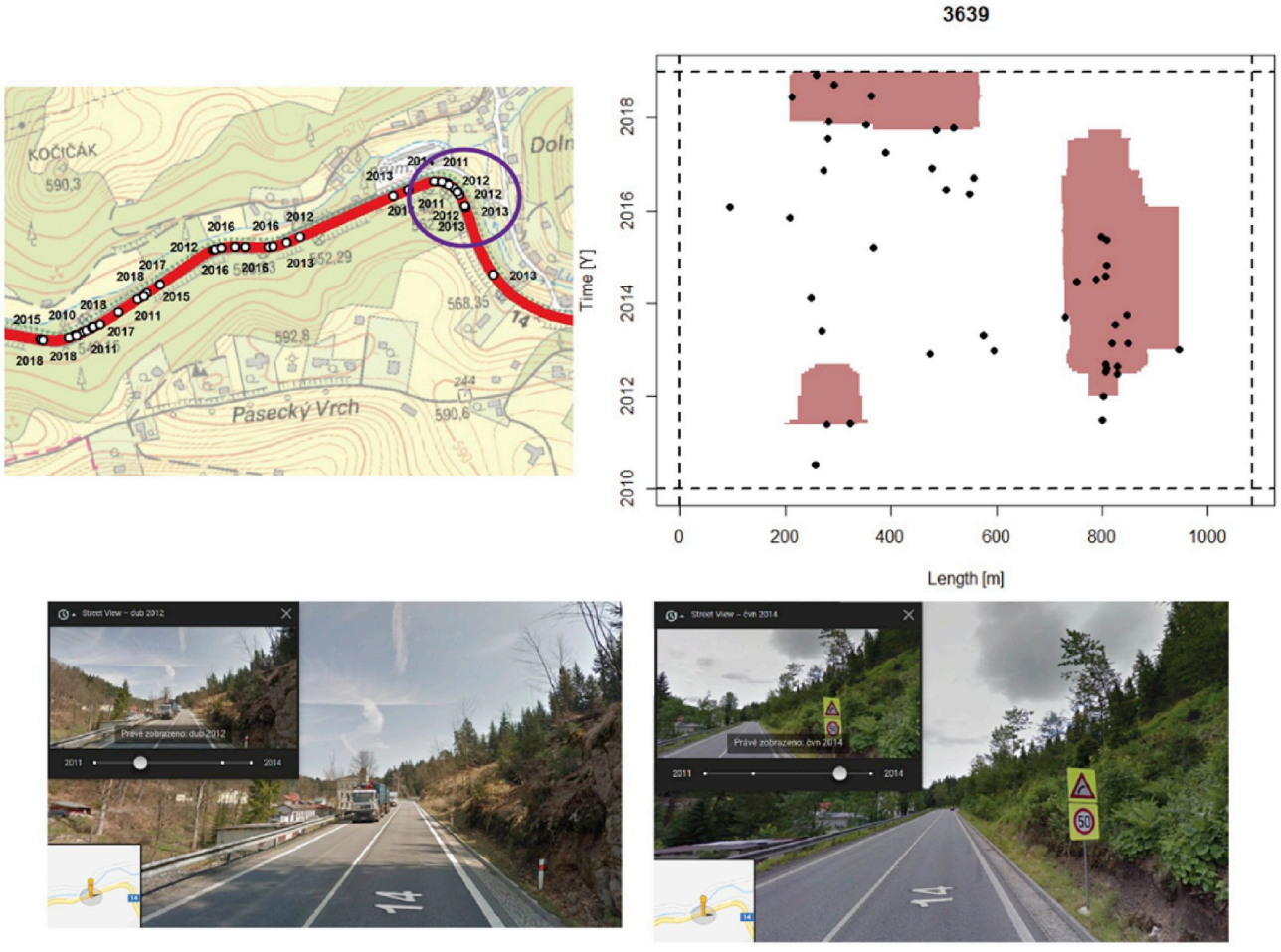

Fig. 7. A hotspot was detected on road segment no. 3639 between 2012 and 2016. It disappeared in all probability as a result of the installation of a warning sign.

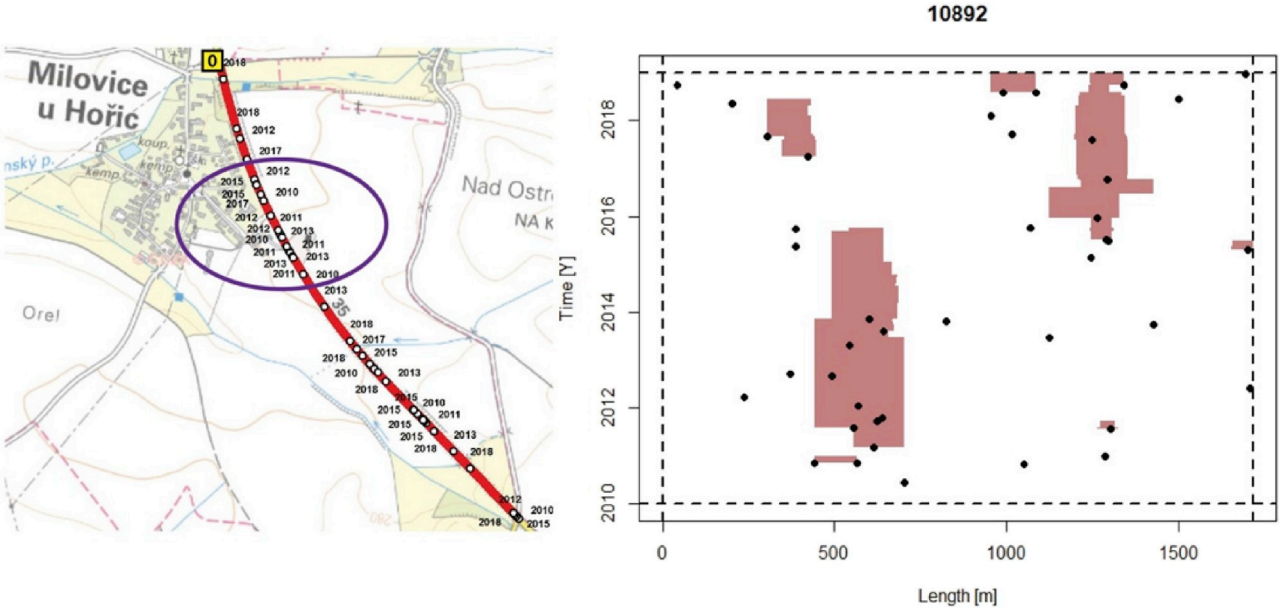

Fig. 8. Hotspot occurred at a place of parking for trucks and a gas station at road segment no. 10892 and was detected between 2010 and 2014. It disappeared after more complex safety measures: cancelation of the pedestrian crossing, new horizontal traffic sign, a new branch strip and reduction of speed.

built, creating, however, a dangerous place at the end of that road segment. Drivers were not expecting, due to limited visibility, a curve but a straight section. The hotspots (Fig. 9) occurred in 2012 when this road no. 6529 had been constructed. It is interesting that there were no crashes recorded on the rest of the new bypass.

Another case of hotspots emergence occurred when the road administrator upgraded the road pavement (see Fig. 10). This probably allowed cars to travel at higher speed within this segment.

The hotspot at road no. 16741 (Fig. 11) is located at a curve. Trees, which originally blocked visibility, were cut down in 2013, but a large concrete block (see the photo on Fig. 11) on a parcel, which is not owned by the road administrator, remained very close to the road. The road administrator stated that the curve had to be reconstructed as its radius was too small, but reconstruction work is currently blocked due to issues related to private land along that road.

4.3.3. Hotspots stability over time

The most interesting are hotspots which were stable over the entire period of time. These places are usually influenced by poor infrastructure, e.g. a dangerous curve as 83 out of 100 stable clusters occurred on curves, whereas the remaining 17 on tangents (straight road segments).

Fig. 12 presents an example of a temporally stable cluster over the entire period. This is a dangerous curve where 91 traffic crashes over 9

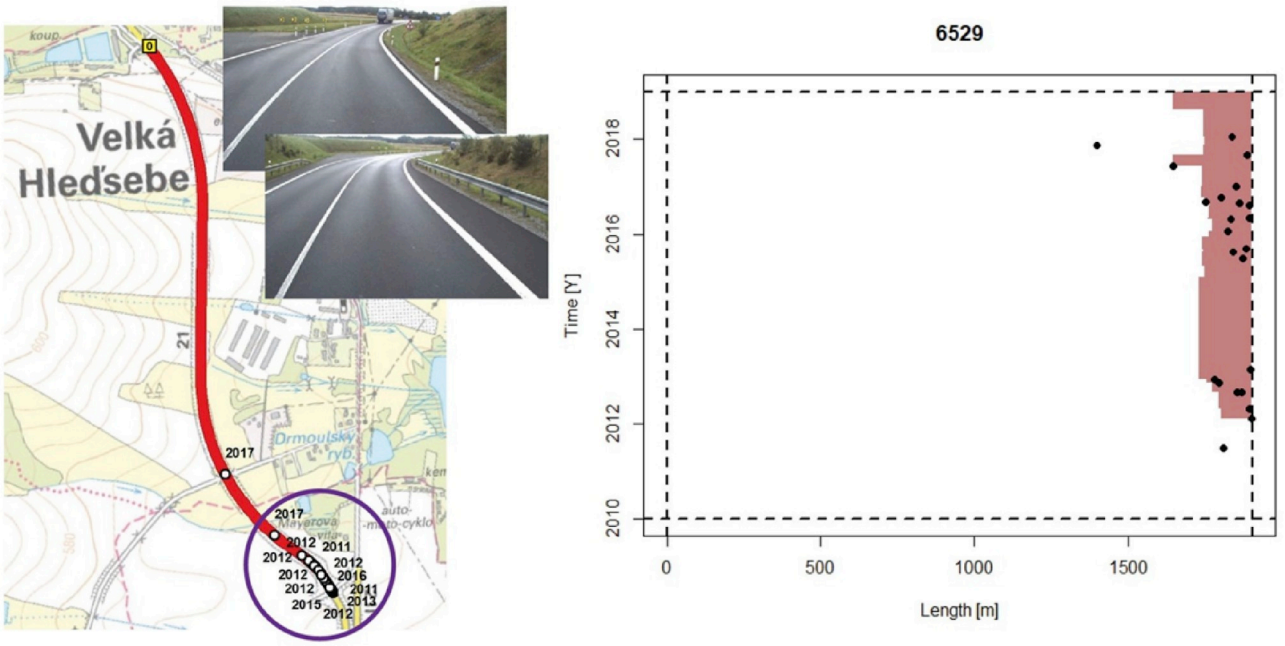

Fig. 9. Road segment no. 6529 represents a newly built bypass in 2012 when a dangerous place was established. Hotspots emergence is thus clearly visible from the spatiotemporal perspective.

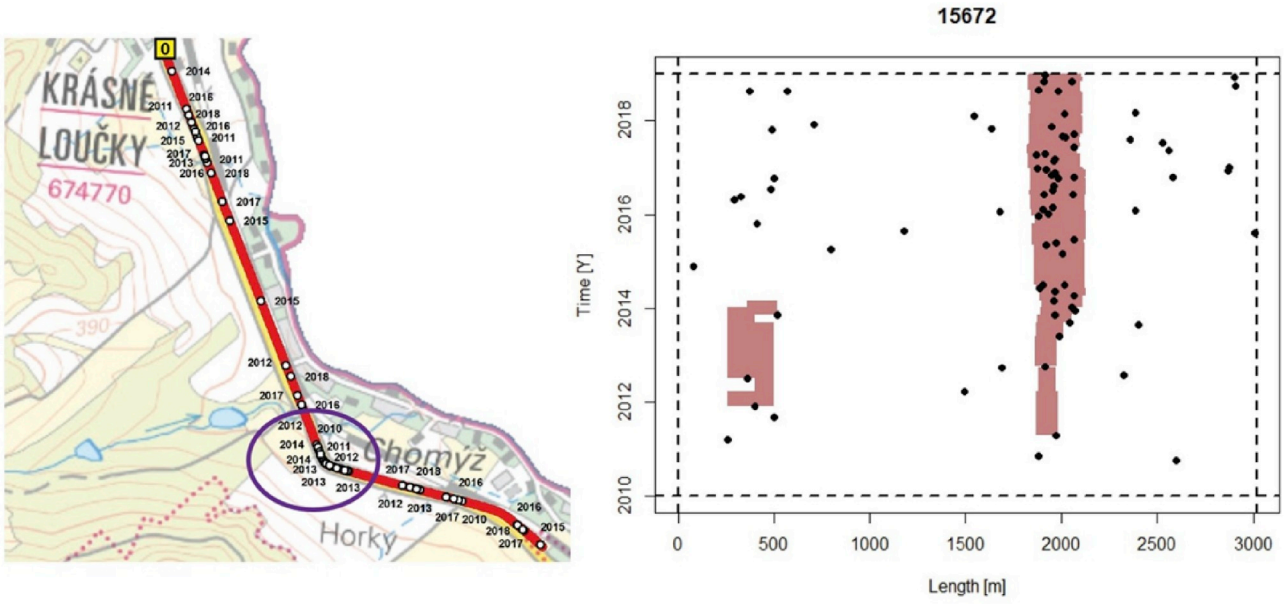

Fig. 10. Hotspots emerged at road segment no. 15672 as a result of increased speed of cars which followed a significant improvement of road surface quality after 2012.

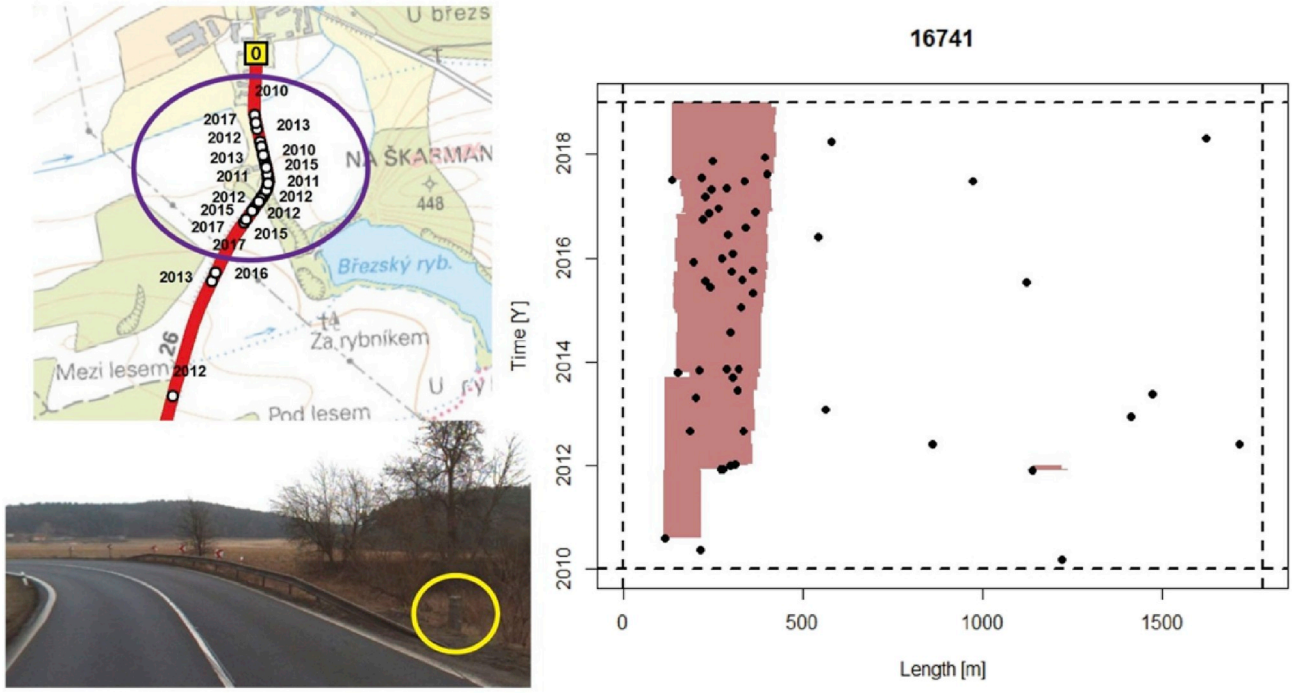

Fig. 11. The hotspot on road segment no. 16741 emerged as a result of increased speed of cars due to cutting of trees along the road. 37 crashes were recorded as of 2012, 30 of them caused, according to the Police crash data, by high speed of cars.

years occurred, whereas only 9 crashes took place on the rest of the road segment. Additional examples of dangerous curves with hotspots can be seen in Fig. 13.

5. Discussion

Spatiotemporal analysis of crash data is able to reveal changes in traffic crash patterns over time. The temporal and spatial evolution of hotspots can be investigated simultaneously when a clustering method is applied with a one day step. Practical application of this approach comprises, for example, evaluation of the effectiveness of traffic safety measures as it is usually known precisely when the measures were applied. This analysis can directly be applied to roads (i.e. their linear representation) when precise data on crashes are available (both position and time of crash).

The presented approach has certain advantages over other currently used approaches. Specifically, it does not segment roads into homogenous units (spatial dimension; e.g., one km long segments or other kind of segmentations) such as other approaches, nor time (temporal dimension; e.g., aggregated values for one year). Data on road network

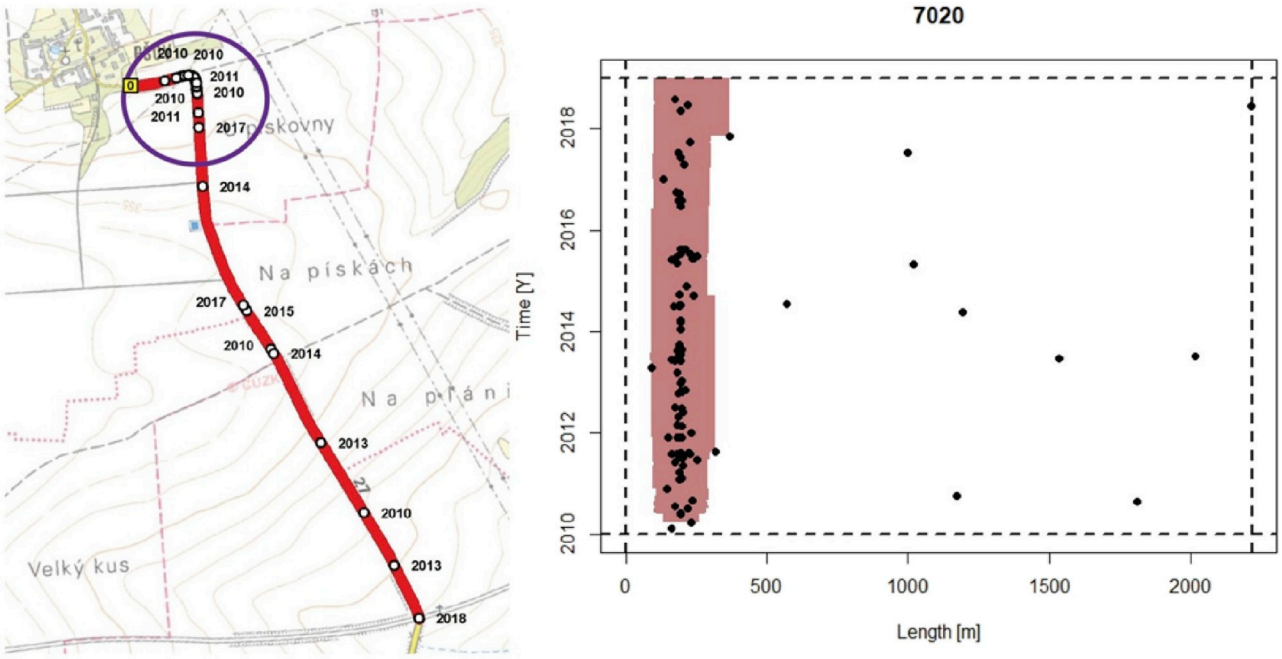

Fig. 12. A dangerous curve presents a stable hotspot on this road segment no. 7020, part of the I/27 primary road.

only has to be prepared in the form of independent *between-intersection* road segments (the first dataset) of whatever lengths. The segment lengths are only influenced by the distance between the two neighboring intersections. The second dataset and traffic crash data with GPS precision. The entire set of the resulting clusters can then be ranked according to cluster strength (see Bíl et al., 2013) to identify the most dangerous places.

The time window, for which the spatial clustering is computed, moves continuously over time and data within that window are analyzed immediately when the set of crashes changes. Spatiotemporal graphs can then be drawn together with statistically significant clusters (hotspots). Dates of applied measures can be incorporated into such a graph allowing the road administrator to visually evaluate the effects of the measures. The above-mentioned examples of the three elementary hotspot types only represent a small part of all possible types. Hotspots often emerge and disappear at one place or move across a road segment. These patterns cannot be, however, unveiled using standard approaches, when hotpots are only computed for respective (whole) years or a constant period of time (e.g., three years). The suggested causes of hotspots presence, shown on the concrete locations in this study, were provided by the road administrator. It was not, however, the aim of this work to verify these suggestions as other factors could also act in hotspots emergence or disappearance.

This analysis can be applied to the entire traffic crash database or to a predefined selection, such as crashes resulting in fatalities, animal-vehicle collisions, run-off-road accidents, etc. The selection is only influenced by the availability of the respective attributes in the data. The presented method is not able to predict, if hotspots will remain at the same place over the following years. It can be assumed, however, that with no positive changes on the respective roads (i.e., safety measures,

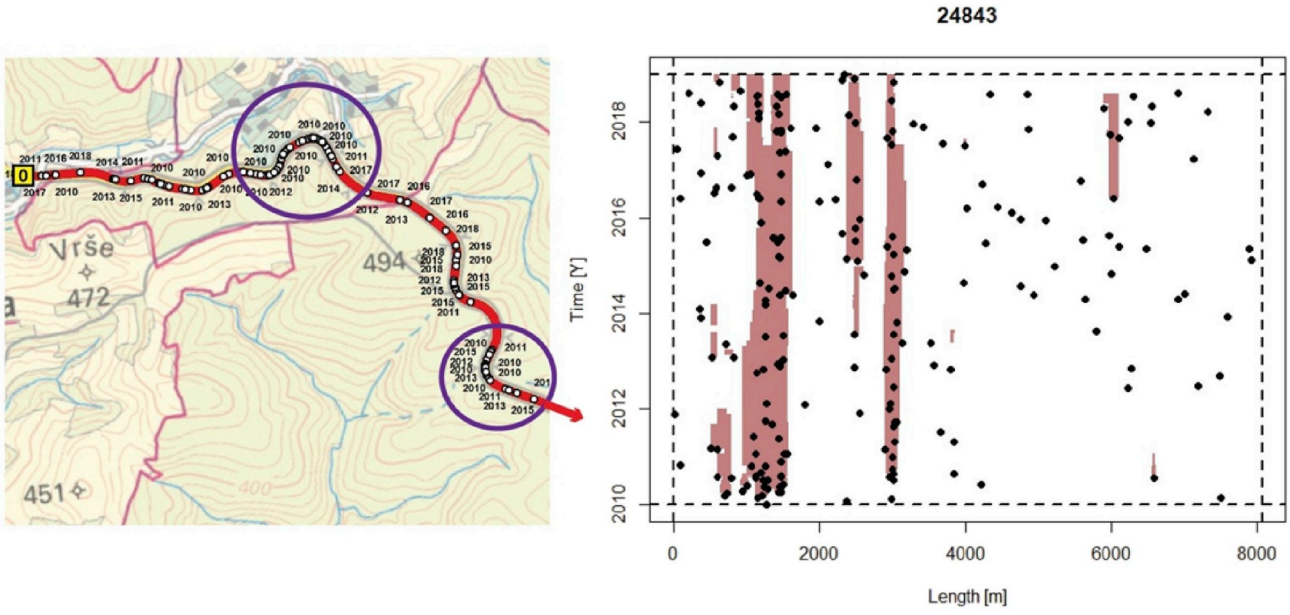

Fig. 13. Two stable hotspots on road segment no. 24843.

decrease in traffic flow, etc.), the hotspots will also be presented there. Long-lasting hotspots are dangerous places on road networks and should be preferably mitigated by road administrators.

6. Conclusions

We presented an approach which is capable of evaluating spatio-temporal behavior of traffic crash hotspots in high detail. This approach can be utilized in research focusing on the spatiotemporal evolution of crash patterns within a road network. Practitioners can use it as a tool allowing for a retrospective analysis of the efficiency of safety measures. The primary advantage of this approach is its rapidity and objectiveness as the KDE+ method only needs two parameters: the kernel bandwidth for the spatial and the width of the time window for temporal analysis.

The primary contribution of this work to the current knowledge and practice is the following:

- We demonstrated that hotspots (statistically significant traffic crash clusters, i.e. places with higher than expected number of traffic crashes) evolve over time.
- Certain hotspots diminish as a result of successfully applied safety measures, but others emerge due to other safety-related negative factors (e.g., a bad view due to overgrown trees; increasing speed, etc. …). A newly built road can also cause the emergence of hotspots.
- Road administrators can obtain a tool for monitoring of the countermeasures targeted to such places. Hotspot disappearance can thus be proof of successfully applied mitigation work.

Acknowledgments

This work was financed by the project VI20172019071 provided by the Ministry of the Interior of the Czech Republic. We would like to further thank Vlasta Michková from the Czech National Road Administrator for information about the road conditions in the respective hotspots and David Livingstone for help with the English editing. We would also like to thank the two anonymous reviewers whose comments and suggestions improved the clarity of the text.

Appendix A. Supplementary data

Supplementary data associated with this article can be found, in the online version, at https://doi.org/10.1016/j.apgeog.2019.04.008.

References

Alberta Wildlife Watch Program (2017). *Description of the AWW program.* onlinehttp://www.transportation.alberta.ca/Content/docType253/Production/AlbertaWildlifeWatchProgramPlan.pdf, Accessed date: 10 May 2018.

Anderson, T. K. (2009). Kernel density estimation and K-means clustering to profile road accident hotspots. *Accident Analysis & Prevention,* (41), 359–364.

Bartonička, T., Andrášik, R., Duľa, M., Sedoník, J., & Bíl, M. (2018). Identification of local factors causing clustering of animal-vehicle collisions. *Journal of Wildlife Management, 82*, 940–947.

Bíl, M., Andrášik, R., Duľa, M., & Sedoník, J. (2019). On reliable identification of factors influencing wildlife-vehicle collisions along roads. *Journal of Environmental Management, 237C*, 297–304.

Bíl, M., Andrášik, R., & Janoška, Z. (2013). Identification of hazardous road locations of traffic accidents by means of kernel density estimation and cluster significance evaluation. *Accident Analysis & Prevention, 55*, 265–273.

Bíl, M., Andrášik, R., Nezval, V., & Bílová, M. (2017). Identifying locations along railway networks with the highest tree fall hazard. *Applied Geography, 87*, 45–53.

Bíl, M., Andrášik, R., Svoboda, T., & Sedoník, J. (2016). The KDE+ software: A tool for effective identification and ranking of animal-vehicle collision hotspots along networks. *Landscape Ecology, 31*, 231–237.

Dai, D., & Jaworski, D. (2016). Influence of built environment on pedestrian crashes: A network-based GIS analysis. *Applied Geography, 73*, 53–61.

Elvik, R. (2008). A survey of operational definitions of hazardous road locations in some European countries. *Accident Analysis & Prevention, 40*, 1830–1835.

Erdogan, S., Yilmaz, I., Baybura, T., & Gullu, M. (2008). Geographical information systems aided traffic accident analysis system case study: City of Afyonkarahisar. *Accident Analysis & Prevention, 40*(1), 174–181.

Favilli, F., Bíl, M., Sedoník, J., Andrášik, R., Kasal, P., Agreiter, A., et al. (2018). Application of KDE+ software to identify collective risk hotspots of ungulate-vehicle collisions in South Tyrol, Northern Italy. *European Journal of Wildlife Research, 64*, 59.

Gundoglu, I. B. (2010). Applying linear analysis methods to GIS-supported procedures for preventing traffic accidents: Case study of Konya. *Safety Science, 48*, 763–769.

Heigl, F., Horvath, K., Laaha, G., & Zahler, J. G. (2017). Amphibian and reptile road-kills on tertiary roads in relation to landscape structure: Using a citizen science approach with open-access land cover data. *BMC Ecology, 17*(24), https://doi.org/10.1186/s12898-017-0134-z.

Kaygisiz, Ö., Düzgün, Ş., Yildiz, A., & Senbil, M. (2015). Spatio-temporal accident analysis for accident prevention in relation to behavioral factors in driving: The case of South Anatolian Motorway. *Transportation Research Part F, 33*, 128–140.

KDE+ Bíl, M., Andrášik, R., Svoboda, T., & Sedoník, J. (2018). *Computer software.* Olomouc: CDV - Transport Research Centre. www.kdeplus.cz, 3.0.

Kingham, S., Sabel, C. E., & Bartie, P. (2011). The impact of the 'school run' on road traffic accidents: A spatio-temporal analysis. *Journal of Transport Geography, 19*, 705–711.

Liu, C., & Sharma, A. (2017). Exploring spatio-temporal effects in traffic crash trend analysis. *Analytic Methods in Accident Research, 16*, 104–116.

Li, L., Zhu, L., & Sui, D. Z. (2007). A GIS-based Bayesian approach for analyzing spatial-temporal patters of intra-city motor vehicle crashes. *Journal of Transport Geography, 15*, 274–285.

Olsen, J. R., Mitchell, R., & Ogilvie, D. on behalf of the M74 study team. (2017). Effect of a new motorway on social-spatial patterning of road traffic accidents: A retrospective longitudinal natural experimental study. *PLoS One, 12*(9), e0184047. https://doi.org/10.1371/journal.pone.0184047.

Périquet, S., Roxburgh, L., le Roux, A., & Collinson, W. J. (2018). Testing the value of citizen science for roadkill studies: A case study from South Africa. *Frontiers in Ecology and Evolution, 6*. https://doi.org/10.3389/fevo.2018.00015.

Plug, C., Xia, J., & Caulfield, C. (2011). Spatial and temporal visualisation techniques for crash analysis. *Accident Analysis & Prevention, 43*(6), 1937–1946.

R Core Team (2014). *R: A language and environment for statistical computing.* Vienna, Austria: R Foundation for Statistical Computing.

Rodríguez-Morales, B., Díaz-Varela, E. R., & Marey-Pérez, M. F. (2013). Spatiotemporal analysis of vehicle collisions involving wild boar and roe deer in NW Spain. *Accident Analysis & Prevention, 60*, 121–133.

Silverman, B. W. (1986). *Density estimation for statistics and data analysis.* Chapman and Hall.

Sjölund, M. (2016). *Road and landscape features affecting the aggregation of ungulate vehicle collisions in southern Sweden. Second cycle, A2E.* Grimsö: SLU, Dept. of Ecology.

Steenberghen, T., Dufays, T., Thomas, I., & Flahaut, B. (2004). Intra-urban location and clustering of road accidents using GIS: A Belgian example. *International Journal of Geographical Information Science, 18*(2), 169–181.

World Health Organization (2015). *Global status report on road safety 2015*978 92 4 156506 6.

Xie, Z., & Yan, J. (2008). Kernel density estimation of traffic accidents in a network space. *Computers, Environment and Urban Systems, 32*, 396–406.

Optics and Laser Technology 124 (2020) 105965

Contents lists available at ScienceDirect

Optics and Laser Technology

journal homepage: www.elsevier.com/locate/optlastec

Indoor illumination imitating optical parameters of sunny summer daylight

Jan Vitasek*, Tomas Stratil, Jan Latal, Jakub Kolar, Zdenek Wilcek

Department of Telecommunications, Faculty of Electrical Engineering and Computer Science, VSB–Technical University of Ostrava, 17. listopadu 15, 708 00 Ostrava, Czech Republic

HIGHLIGHTS

- Optical parameters of a sunny summer day were measured.
- Obtained results were used for software simulations.
- Software simulations provided forward current settings of individual colour chips.
- Measurement of opt. parameters of light created according to the simulation results.
- Opt. parameters of an artificial white light is comparable with light of sunny day.

ARTICLE INFO

Keywords:
Colour coordinates
Correlated Colour Temperature
Indoor lighting
RGBA LED
Spectra
Sunny summer daylight

ABSTRACT

Natural daylight has an essential effect on the human organism. It affects mood, emotion or the ability to sleep. For most people, a sunny summer day is the most pleasant day. For this reason, we propose an indoor lighting source which imitates sunny summer daylight. We collected a series of experimental measurements of days during the summer of 2018. We chose the sunniest day (minimum cloud, high temperature, high total time of sunshine) and we used its optical parameters as an example. The obtained parameters (colour coordinates x and y) served as the input parameters for LightTools simulations. Simulations in LightTools enabled to obtain power settings of individual colour chips. The power values were transformed into forward current values of individual colour chips. Subsequent, laboratory measurements of the optical parameters according the forward current values were done with a tetrachromatic RGBA LED. Suitable setting of forward currents of the RGBA LED enables to create sunny daylight from sunrise to sunset. The laboratory measurement confirmed our assumptions, the imitation of daylight was successful.

1. Introduction

The technical literature speaks about the influence of daylight on psychological and biological states of humans [1–5]. Daylight affects human psyche and behaviour. The light perceived by the human visual system affects feelings and mood (psychological state). Receptors in the visual system perceive light, resulting in production of cortisol (stress hormone) and melatonin (sleeping hormone) [1,6–8]. These hormones affect the human's biological state, especially the circadian rhythm. This rhythm is influenced by light, especially blue light [9,10].

Several human biological rhythms are related to the alternation of day and night. The use of electric lighting has caused the intervention of this cycle. Since then, all human activities can be done at any time during the day or night. The electric lighting has significantly affected the work process by allowing three-shift operation and working at any time (morning, day, evening, night) [11].

Indoor lighting is designed to meet the visual requirements according to the standards and regulations and has as low energy consumption as possible. So far, appropriateness of the emitted spectrum at the right time regarding the circadian rhythm has not been considered [10].Daylight is something that human organism depends on and follows. We assume that light fitting imitating the course of light during the day can be useful for human body and its rhythms and an imitation of a sunny day can improve human mood. Incorrect illumination at the wrong time can lead to a circadian rhythm disturbance, which can cause poor sleep, mood disorders, depression, diabetes, obesity [1,8,10–12].

The mood of humans is also influenced by the weather itself [13–16]. Everyone feels a difference if it is a beautiful sunny day or if it is cloudy, rainy and with a cold wind. Most people prefer sunny days, so

* Corresponding author.
E-mail address: jan.vitasek@vsb.cz (J. Vitasek).

https://doi.org/10.1016/j.optlastec.2019.105965
Received 31 July 2019; Received in revised form 30 September 2019; Accepted 23 November 2019
Available online 10 December 2019
0030-3992/

we have come up with an idea of creating an indoor lighting emitting light imitating sunny daylight using a suitable illumination source.For this purpose, we wanted to obtain real optical parameters of sunny daylight. We performed long-term measurements of the sky in the summer of 2018. We used a spectrometer, which periodically saved selected optical parameters. The optical parameters were colour coordinates x and y, Correlated Colour Temperature CCT and spectra. Then we retroactively analysed the weather and we selected the sunniest day (minimum cloud, high temperature, high total time of sunshine). The optical parameters of the sunniest day were then used for LightTools software simulation. The simulation found the correct light outputs of the individual colour chips which together create light with desired optical parameters. The light outputs (optical power) were converted in forwards currents according to PI (power-current) characteristics. The values of the forward currents were used for a laboratory measurement. We set the forward currents and measured the optical parameters by the spectrometer. At the end, we compared the optical parameters obtained from the real measurement of the sky and the laboratory measurement. The aim was to create artificial daylight of a sunny day.

The imitating of daylight is also described in [17]. The authors used two types of fluorescent tubes. It was in pre-LED age. The tubes emitted white light with constant CCT, their spectra were not changed. Another article [18] describes lighting with 547 LEDs (32 different wavelengths) imitating daylight. The emitted powers of these LEDs were manually set. The authors of this work set the LEDs according to a spectrum of a day measured by a spectrometer. The disadvantage is a huge number of LEDs, moreover manually set. Daylight simulation is also described in article [19]. Their proposed system automatically tunes spectrum of an illumination source. The luminaire contains 24 monochromatic LEDs divided in 12 channels. Their system uses a low-cost spectrometer, which scans a spectrum of sky through a skylight in a roof. Measured data are transferred in computer, which calculates, and sets needed optical powers for the separated channels. The system so imitates outdoor light. The disadvantage of their system is measurement of daylight, computer evaluation and setting of all 12 channels. The system depends on actual outdoor conditions. The paper does not describe which light is emitted after sunset. Another article [20] describes a creating of an artificial daylight by OLED panels. Authors used two OLED panels (2100 K and 3400 K) to creating daylight. The changes of CCT during day (mainly at dawn and twilight) were not mentioned in this article.

Sunny days are characterized by white wide-spectrum light. This white light can be created in two ways, using a phosphor powder or colour mixing. The phosphor powder converts shorter wavelengths (blue) into longer wavelengths (yellow, green). The phosphor powder is most cases the Yttrium Aluminium Garnet doped by Cerium ($Y_3Al_5O_{12}$:Ce^{3+}), which is excited by a blue light emitting chip. A part of blue light is spectrally converted into yellow light. The resulting compound of blue and yellow light results in the occurrence of white light. The other way is called colour mixing. The LED is composed of three (red, green, blue) or more (orange or cyan or other) monochromatic emitting chips. Correct setting of power supply of chips creates white light. Increasing number of chips increases the Colour Rendering Index, but it reduces the luminous efficacy [21–24]. We used the tetrachromatic RGBA LED labelled as KW-4RGBW [25] for our purposes.

This paper deals with a description of the sky measurements, simulations and laboratory measurements of optical parameters of light. The following section describes the sky measurements of the optical parameters of the sunny day. Section 3 deals with the simulations of real measured optical values in LightTools software. Section 4 uses the results from the simulations and describes the creation of the sunny light in laboratory conditions. Section 5 compares the obtained results. Last section concludes this article.

2. Optical parameter measurement of the sky during the summer of 2018

We carried out several all-day measurements of the optical parameters during the summer of 2018. After each series of measurements, the weather of measured days was evaluated. We looked for the sunniest day. We chose the sunniest day as the 4th of July 2018. It was clear (cloudiness 1.7, <1.9 means clear), maximum temperature 28.8 °C, average temperature 20.9°C, total time of sunshine 14.6 h (more than 90% of possible astronomical sunshine) [26] - measured by the Czech Hydrometeorological Institute located in close proximity to the place of measurements. The measurements were carried out at the University campus of VSB–Technical University of Ostrava (49.8313469 N, 18.1586469E), in the Czech Republic. The measured parameters were the total spectra of the sunny day, colour coordinates x and y (CIE1931 diagram) and Correlated Colour Temperature (CCT). We used the Avantes HS2048XL spectrometer(model AvaSpec-HS2048XL-USB2, 2048 pixel back-thinned CCD detector, grating HS500-0.33-500 lines/mm, calibrated on 15.12.2016) together with an optical fibre. This spectrometer allows periodic storage of selected parameters in a file for further processing.

2.1. Measurement of spectra

The following Fig. 1 shows the optical spectra for each half hour from 4:30 (before sunrise) to 21:00 (after sunset). It is possible to observe the time evolution of the spectrum during the sunny day. Fig. 1 shows a gradual increase in the visible (VIS) and the near infrared (IR) part of the spectra. After midday the IR spectrum began to decrease, stabilized, and then it was almost constant up to the evening. The visible part of the spectra grew during the day up to the late afternoon, then decreased.

2.2. Correlated Colour Temperature

Next Fig. 2 shows the waveforms of the Correlated Colour Temperature (CCT) during the measured day. The chart shows values for the time period from 4:30 (before dawn) to 21:00 (after twilight). The sunrise at the place of measurements was at 4:43 on 4th of July, sunset at 20:58. These times are given in the Central European Summer Time (CEST). Therefore, the night is unequally distributed, as it is seen in Fig. 2. The CCT values significantly increase at sunrise and sunset, resulting in high peaks at the given times. The human organism is mainly sensitive to these peaks [9,10]. If we ignore the mentioned peaks at

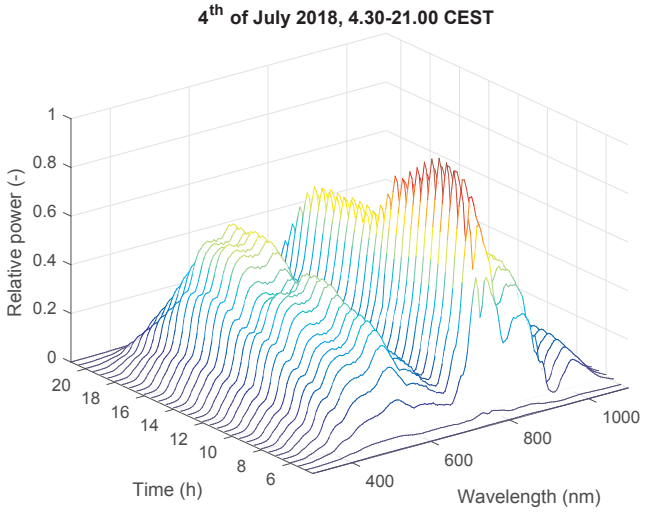

Fig. 1. Optical spectra from 4:30 to 21:00 in half-hour intervals on 4th of July 2018.

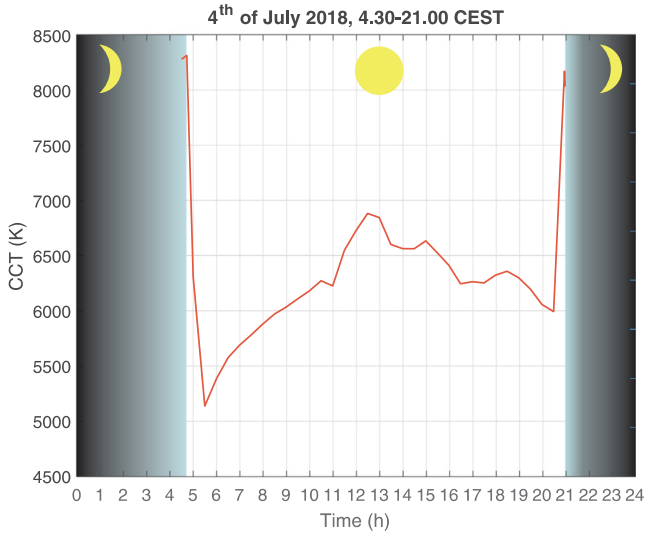

Fig. 2. CCT values from 4:30 to 21:00 in half-hour intervals on 4th of July 2018.

dawn and twilight, it is generally possible to say that the CCT values gradually increase during the day, with the maximum occurring around midday (in our case at 13:00 CEST) and then gradually decreasing, which also confirmed the measurements of other days.

2.3. Colour coordinates

The measured optical parameters were the colour coordinates x and y. Shown in Fig. 3 (below), there is the CIE1931 diagram which displays the colour coordinates of five significant points, sunrise (4:43), morning (9:00), noon (13:00), afternoon (17:00), and sunset (20:58). The times are valid for the CEST time zone. It is seen from the CIE1931 diagram, that the sunrise and sunset points are almost at the same position in the diagram.

The following Table 1 shows the measured optical parameters (CCT and colour coordinates x and y) during the 4th of July 2018. The CCT values from this table are plotted in Fig. 2 and some colour coordinates in Fig. 3.

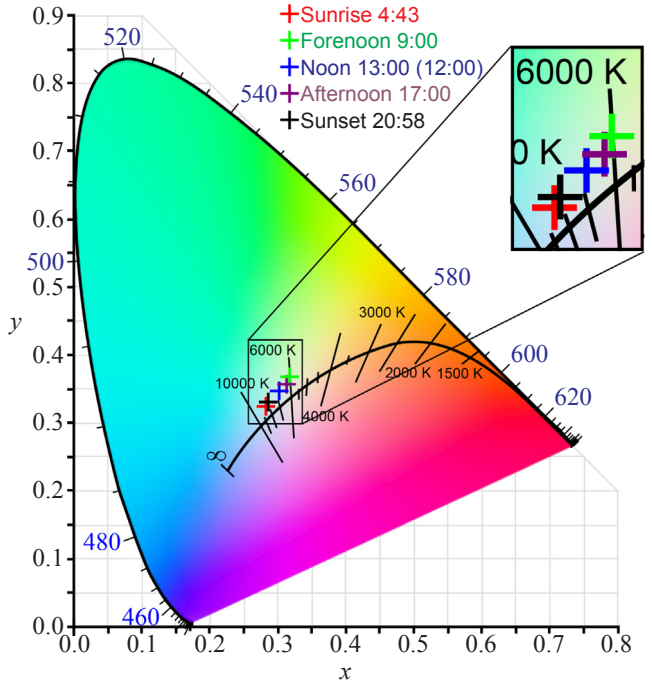

Fig. 3. Colour coordinates of five chosen points on 4th of July 2018.

Table 1
Measured optical parameters of sky on 4th of July 2018.

time	CCT	x	y	time	CCT	x	y
4:30	8280.7	0.2835	0.3258	13:00	6844.0	0.3031	0.3487
4:43	8314.4	0.2860	0.3189	13:30	6600.2	0.3076	0.3513
5:00	6304.6	0.3127	0.3652	14:00	6562.4	0.3084	0.3518
5:30	5134.2	0.3444	0.3949	14:30	6560.4	0.3080	0.3521
6:00	5383.4	0.3360	0.3911	15:00	6632.9	0.3077	0.3520
6:30	5573.1	0.3306	0.3861	15:30	6523.8	0.3090	0.3531
7:00	5688.2	0.3271	0.3819	16:00	6410.2	0.3114	0.3554
7:30	5780.7	0.3248	0.3785	16:30	6242.9	0.3147	0.3581
8:00	5879.2	0.3225	0.3757	17:00	6261.4	0.3142	0.3586
8:30	5969.8	0.3201	0.3722	17:30	6250.9	0.3144	0.3594
9:00	6032.8	0.3186	0.3697	18:00	6321.1	0.3129	0.3581
9:30	6107.7	0.3171	0.3669	18:30	6357.6	0.3121	0.3576
10:00	6179.6	0.3155	0.3644	19:00	6297.6	0.3134	0.3590
10:30	6271.2	0.3136	0.3617	19:30	6194.7	0.3154	0.3615
11:00	6223.4	0.3148	0.3607	20:00	6054.8	0.3185	0.3660
11:30	6546.2	0.3082	0.3555	20:30	5991.6	0.3199	0.3657
12:00	6725.0	0.3048	0.3520	20:58	8170.8	0.2871	0.3219
12:30	6880.5	0.3023	0.3491	21:00	8033.0	0.2869	0.3323

3. Simulation in LightTools software

LightTools is optical design software that enables virtual prototyping, optimization, simulation, rendering, visualization and ray-tracing of optical systems. Designed illumination systems are modelled according to defined specifications thanks to the possibility to set many optical and mechanical properties. LightTools works with 3D models, which are drawn in this software or imported from another 3D CAD software. LightTools offers a large component library including optical sources, optical materials, lenses etc. LightTools calculates photometric and radiometric values needed for analyses of illumination, luminance, angular and spatial luminance display and further analysis tools [27]. In this software, the RGBA LED with four emitting chips was created. A central emitted wavelength including FWHM and transmitted power can be set to each emitting chip. Alternatively, we can import the spectrum measured by the spectrometer and adjust the transmitted power. In order to create the most reliable model of this LED, the emitted spectra of the individual chips (Fig. 4) and the emitted optical power were measured in the laboratory by the spectrometer Avantes. The real measured spectra were then imported into LightTools to the

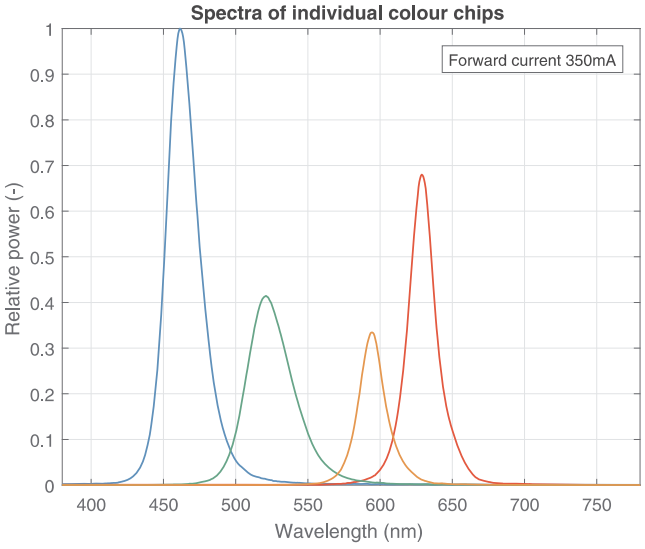

Fig. 4. Spectra of individual chips.

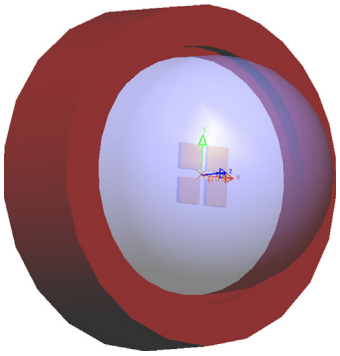

Fig. 5. LED RGBA model in LightTools.

individual chips, where the optical power levels were set according to the measured data in the laboratory.It has been written, the RGBA LED composes of four colour chips. A red chip emits light with a wavelength of 628.8 nm, FWHM 20.7 nm, optical power 113.2 mW at a forward current of 350 mA. A green chip emits light with a wavelength of 521.3 nm, FWHM 34.6 nm, optical power 81 mW at a forward current of 350 mA. A blue chip emits light with a wavelength of 461.4 nm, FWHM 24.8 nm, optical power 149 mW for a forward current of 350 mA. An amber chip emits light with a wavelength of 594.6 nm, FWHM 20.6 nm, optical power 51.7 mW for a forward current of 350 mA. The RGBA LED model created in LightTools is in Fig. 5. The individual chips are easily visible.

As mentioned above, LightTools software which was used for this experiment, allows the user to optimize the selected parameters. The variable parameter was the emitted power of the individual LED colour chips. The optimization found these settings of the optical powers that the colour coordinates x and y match as much as possible with the values in Table 1 at given times (sky measurements). The results of the simulations are the optical power values emitted by given chips, it is seen in Table 2.

The optimization criteria were the colour coordinates x and y for a higher accuracy. The CCT value as the criterion is not appropriate because for one CCT value there may be several points in the CIE1931 diagram whose colour coordinates x and y are different but the CCT is the same.

The next step was to convert the obtained optical powers to the forward currents, because LightTools provides only optical powers, not

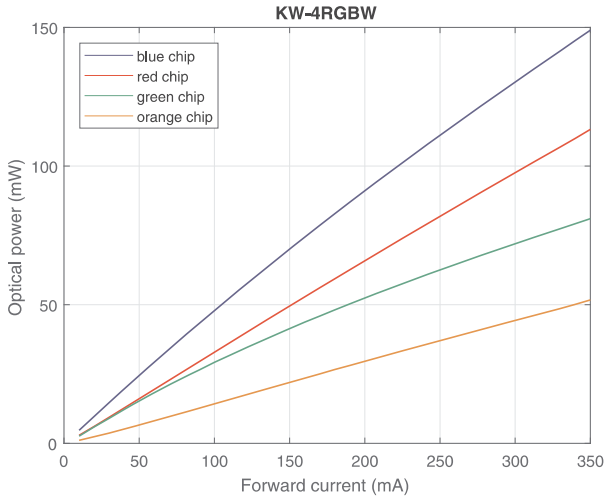

Fig. 6. PI characteristics of individual chips of RGBA LED.

forward currents. The optical power values from the simulations (shown in Table 2) were converted to the equivalent forward currents according to the PI (power-current) characteristics measured in the laboratory. The measured PI characteristics, Fig. 6, were interpolated with a second order polynomial ($y = a{\cdot}x^2 + b{\cdot}x + c$). Using Matlab (the solve command: looking for an unknown x while y is known), these polynomials were solved, and the resulting values were recorded as the forward currents. By supplying these forward currents, the chips emit the given optical powers. The results of the conversions are in Table 3.

4. Experimental measurement in laboratory

The measurement was carried out in a dark laboratory with obscured windows. Each individual colour chip of the RGBA LED was separately supplied by laboratory sourcesDIAMETRAL L240R51D (2 channels, 0–30 V, 0.1–4.0 A); the amounts of the forward currents were monitored by ammetersUNI-T UT70A (bought in 2018). The same spectrometer, Avantes HS2048XL, together with the optical fibre measured the optical parameters (colour coordinates x and y, CCT, spectra).The RGBA LED was mounted on a cooler and fixed to the optical table. Also, the optical fibre was fixed to the table, therefore the measurement conditions were constant. The forward currents of the

Table 2
Optical powers of individual colour chips.

	Optical power (mW)		Optical power (mW)			Optical power (mW)		Optical power (mW)	
time	blue	green	red	orange	time	blue	green	red	orange
4:00	71.5	71.6	46.6	51.7	13:00	66.2	79.4	25.3	41.7
4:30	79.9	81.0	24.8	38.3	13:30	63.5	77.6	24.6	42.8
4:43	82.3	78.5	31.1	35.6	14:00	64.6	79.5	26.5	43.0
5:00	55.6	79.3	32.2	35.1	14:30	64.5	79.5	26.3	42.9
5:30	41.9	79.1	35.2	41.0	15:00	63.0	77.0	24.1	42.6
6:00	43.5	78.9	34.2	38.1	15:30	63.9	79.6	26.4	43.1
6:30	45.6	78.7	33.5	37.0	16:00	62.7	79.5	26.7	43.5
7:00	46.9	77.4	31.5	37.2	16:30	62.4	79.7	23.2	48.0
7:30	48.8	78.6	33.3	26.3	17:00	62.1	79.6	22.7	47.9
8:00	50.0	78.5	33.2	35.9	17:30	62.5	80.3	23.3	48.1
8:30	47.0	68.2	20.0	39.4	18:00	63.5	80.6	22.9	48.2
9:00	47.9	67.9	20.0	39.3	18:30	58.0	76.8	31.3	36.4
9:30	54.7	79.3	33.4	36.1	19:00	62.8	80.4	22.7	48.1
10:00	56.2	79.6	33.4	36.0	19:30	61.0	79.8	22.8	48.0
10:30	60.9	79.6	21.4	47.8	20:00	55.4	79.6	34.5	36.7
11:00	61.5	80.0	22.8	48.0	20:30	55.2	79.4	35.6	36.5
11:30	64.4	80.0	20.3	47.7	20:58	78.8	77.9	32.3	33.3
12:00	64.3	79.4	25.0	41.8	21:00	75.1	78.2	21.4	39.8
12:30	65.9	79.5	24.9	41.4	21:30	73.8	71.9	42.6	50.6

Table 3
Forward currents of individual monochromatic chips to emit needed optical powers.

time	Forward current (mA)				time	Forward current (mA)			
	blue	green	red	orange		blue	green	red	orange
4:30	80.72	143.50	69.27	109.11	13:00	73.64	143.50	35.13	193.01
4:43	85.69	143.50	77.27	109.11	13:30	71.71	143.50	38.35	193.01
5:00	63.62	143.50	35.42	193.01	14:00	71.28	143.50	38.94	193.01
5:30	46.34	143.50	50.39	193.01	14:30	71.28	143.50	38.35	193.01
6:00	48.85	143.50	44.22	193.01	15:00	71.28	143.50	38.06	193.01
6:30	51.79	143.50	41.58	193.01	15:30	70.43	143.50	38.94	193.01
7:00	53.89	143.50	40.40	193.01	16:00	69.15	143.50	40.11	193.01
7:30	55.79	143.50	40.11	193.01	16:30	67.23	143.50	42.16	193.01
8:00	57.26	143.50	39.52	193.01	17:00	67.02	143.50	41.28	193.01
8:30	59.38	143.50	38.94	193.01	17:30	66.59	143.50	40.99	193.01
9:00	60.65	143.50	38.94	193.01	18:00	67.44	143.50	40.11	193.01
9:30	62.34	143.50	38.94	193.01	18:30	67.87	143.50	39.52	193.01
10:00	63.83	143.50	38.94	193.01	19:00	66.80	143.50	40.11	193.01
10:30	65.32	143.50	38.64	193.01	19:30	65.32	143.50	40.70	193.01
11:00	65.74	143.50	40.40	193.01	20:00	62.56	143.50	41.28	193.01
11:30	69.15	143.50	36.30	193.01	20:30	62.77	143.50	43.04	193.01
12:00	71.07	143.50	34.83	193.01	20:58	92.63	143.50	34.25	193.01
12:30	73.42	143.50	33.96	193.01	21:00	76.42	143.50	68.97	193.01

Table 4
Forward currents of individual chips for emitted white light (according colour coordinates x and y).

time	Forward current (mA)		Forward current (mA)		time	Forward current (mA)		Forward current (mA)	
	blue	green	red	orange		blue	green	red	orange
4:30	85.2	141.5	85.7	107.1	13:00	80.4	142.3	40.0	193.4
4:43	90.1	141.6	89.2	107.3	13:30	78.4	142.3	44.5	193.4
5:00	70.4	142.0	39.0	193.0	14:00	77.8	142.3	44.5	193.4
5:30	54.2	142.1	56.8	193.0	14:30	77.8	142.3	44.1	193.3
6:00	56.7	142.0	49.6	193.0	15:00	77.8	142.3	44.1	193.3
6:30	59.1	142.1	45.2	193.0	15:30	77.2	142.2	45.1	193.1
7:00	61.7	142.1	45.0	193.2	16:00	75.6	142.2	46.1	193.1
7:30	63.6	142.2	45.7	193.3	16:30	74.1	142.3	49.0	193.1
8:00	64.9	142.2	44.1	193.3	17:00	73.6	142.3	47.5	193.1
8:30	66.3	142.2	43.0	193.3	17:30	73.4	142.3	47.3	193.1
9:00	68.1	142.2	43.6	193.3	18:00	74.2	142.3	46.4	193.1
9:30	69.5	142.2	44.7	193.4	18:30	74.0	142.3	45.1	193.1
10:00	70.7	142.3	44.5	193.3	19:00	73.6	142.3	46.1	193.3
10:30	72.4	142.3	44.5	193.3	19:30	72.2	142.2	46.4	193.4
11:00	72.8	142.3	46.2	193.3	20:00	69.8	142.2	46.9	193.4
11:30	75.6	142.3	40.8	193.3	20:30	69.7	142.2	49.3	193.4
12:00	77.8	142.3	38.9	193.3	20:58	97.6	142.4	39.9	193.6
12:30	79.9	142.3	37.6	193.4	21:00	90.3	142.3	28.8	193.5

individual colour chips were set according to Table 3. However, it emerged, that the supply currents had to be adjusted and thus they did not correspond to the values obtained from optimization in LightTools (Table 3). During the laboratory measurement, the calculated forward currents were corrected so that the created light had the required colour coordinates x and y. The values of the forward currents obtained in the laboratory are in Table 4.

The following Fig. 7 shows the waveforms of the forward currents of individual RGBA LED colour chips. The full lines show the values from Table 3 (optimization results in LightTools), and the dashed lines represent the values from Table 4 (laboratory measurements). From the results in Table 3 and Table 4 and mainly from Fig. 7, it is obvious that there is not complete agreement, as mentioned above. The forward currents of the orange chip almost correspond to the values obtained in the laboratory. The same can be said about the forward currents of the green chip. The laboratory measurements proved that the forward current of the blue chip must be about 7 mA greater than the simulations calculated. However, the forward current curves of the blue chip are very similar in shape, only shifted. The same is true for the forward

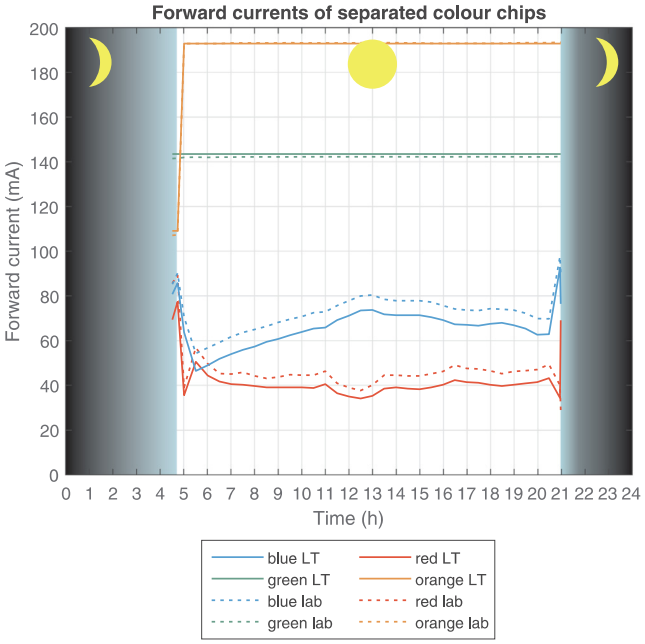

Fig. 7. Needed forward currents and their waveforms.

current curves of the red chip. Measurement in the laboratory required the forward current of the red chip about 5.8 mA greater than the simulation. We attribute this inaccuracy to the fact that the PI characteristics of the individual colour chips are not linear (Fig. 6), whereas LightTools software considers them to be linear. This nonlinearity cannot be applied toLightTools. However, we consider these deviations important. The real measurement is more important than the simulation.

5. Results

During the all-day measurements, the colour coordinates (and other parameters) of the sunny day were obtained. These coordinates were the basis for simulation in LightTools software, which resulted in the finding of suitable forward currents of individual colour chips. Fig. 8 shows and compares the CCT values. The blue line shows the CCT values of the sky. The red crosses show the CCT values obtained in LightTools software. The black circles show the CCT values measured in

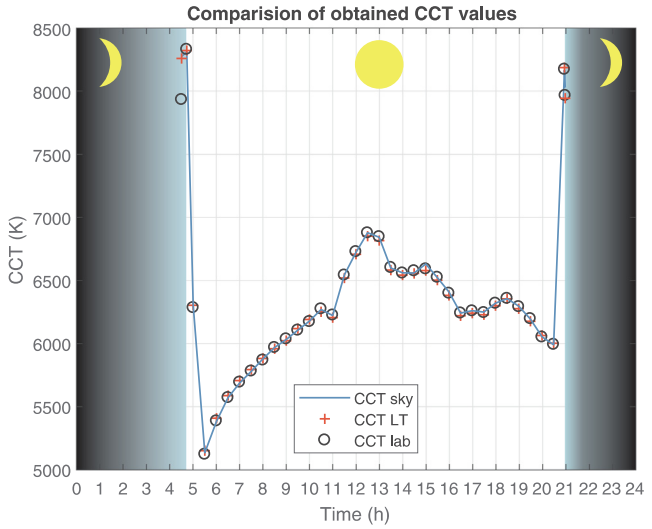

Fig. 8. Comparison of the CCT values: real-measured (sky), simulated in LightTools (LT) and created in laboratory (LED).

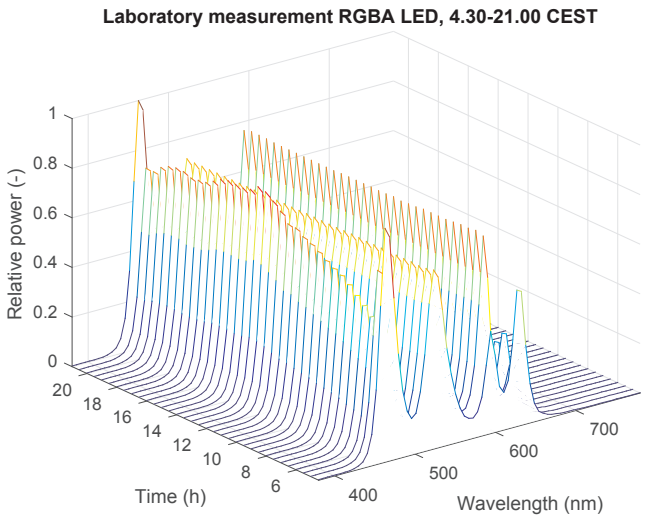

Fig. 9. Optical spectra of RGBA LED from 4:30 to 21:00 in half-hour intervals.

the laboratory with the RGBA LED. It is clearly obvious from Fig. 8, that the CCT values of the sunny day were successfully imitated in the laboratory.

Mathematically, the obtained values can be compared according to the Eq. (1), which is derived from the relative error [28]

$$\Delta(\%) = \left| \frac{CCT_{lab} - CCT_{sky}}{CCT_{sky}} \right| \cdot 100, \tag{1}$$

where the CCT_{lab} is the value measured in the laboratory, and the CCT_{sky} is the value of the sunny day for given times.

We can also compare the results according to the Standard Deviation Colour Matching (SDCM) [29]. The SDCM has the same meaning as a MacAdam ellipse. SDCM defines numbers. If white light falls within 1 SDCM, most people would fail to see any difference in colour. If light falls in 2 SDCM (or a 2-step MacAdam ellipse), people will start to see some colour difference [29].The greatest difference Δ of CCT, calculated according to Eq. (1), was found in time 4:30 (before sunrise ⇒ it is night). Also, the SDCM value at this time was very high, specifically Δ was 4.15 % and SDCM was 3. Then the difference Δ decreased under value <0.3 % and SDCM was 1 during the day. The difference Δ then increased in time 21:00 (after sunset), the Δ was 0.79 % and SDCM was again 1.

We also compared the colour coordinates x and y of the sunny sky and measurements in the laboratoryaccording to the Eq. (1). The largest deviation Δ of the colour coordinates x was 1.7% (at 4:30), the mean deviation of the colour coordinate x was less than a tenth of a percent (< 0.1%). The largest deviation Δ of the colour coordinates y was 0.9% (again at 4:30), the mean deviation of the colour coordinate y was also less than a tenth of a percent (< 0.1%). Generally, we can say that the greatest differences occured before sunrise and after sunset.

The last Fig. 9 shows the optical spectra of the RGBA LED for every half hour obtained from the laboratory measurement.Every half hour has its forward current setting of the individual chips. These settings reflect in emitted spectra. The shown waveforms do not reflect the gradual increase in optical power from dawn to noon and then decline to twilight. This was not the goal. The settings of the forward currents (emitted spectra) should be used for the indoor light fitting, where constant emitted optical power is assumed throughout the illumination in order to meet the lighting conditions for the space.

6. Discussion and conclusion

The aim of this work was to measure the optical parameters of the sunny summer day. These parameters were used for the simulation of the sunny day, using the tetrachromatic RGBA LED. The sunlight has a significant effect on the human organism and its physiological and biological state. Not every day can be sunny, so it was attempted to simulate it. The main measured parameters were the colour coordinates x and y and CCT values of the sunny day. The aim of simulation and subsequent laboratory measurement with the RGBA LED was to create white light with the same colour coordinates x and y as the sunny day, which was successful. The result is the waveforms of the forward currents from sunrise to sunset. These waveforms can be certainly adjusted (accelerated or slowed down) as needed. If a light fitting is made up of the RGBA LEDs with time-controlled supply sources, it will be possible to create sunny daylight indoor.

The correct spectrum of emitted light helps the human body control its circadian rhythm. The body then knows when it is day and when it is night. During the day the body is active, while it regenerates at night [30]. An increased amount of blue light (increase in CCT values) is used to detect day and night [31–34]. Incorrect spectrum at the wrong time will cause circadian rhythm disruption, which can lead to the health problems mentioned in the introductory chapter.

The RGBA light fitting can be used in any living room to improve mood (not only in the autumn or winter) or in hospitals for therapeutic purposes [35]. In our opinion, the proposed light fitting can also be used in plants during night shifts. Appropriate setting of this light fitting enables the end of a night shift to be accompanied by the end of ”sun” activity, and the body is prepared for the necessary sleep and regeneration. The aim of this article is not to consider the effect of the proposed light fitting on the human body. The aim was to try to design a light source imitating the sunny summer day, as measured.

We would like to continue in our work and our aim is to create a light fitting with the RGBA LEDs. The proposed light fitting will change emitted light according to the obtained results. Furthermore, we want to cooperate with some experts who will be able to evaluate the influence of this light fitting on humans.

Acknowledgment

The authors would like to acknowledge the financial support of the Ministry of Education, Youth and Sports of the Czech Republic under Projects No. SP2019/80 and SP2019/143 of VSB–Technical University of Ostrava, Czech Republic. Our research was also supported by Projects No. VI20172019071, VI20152020008, TA04021263, TK01020162 and TK01020178. The work has been partially supported by Projects No. CZ.1.07/2.3.00/20.0217 and CZ.02.1.01/0.0/0.0/

16_019/0000867.

Appendix A. Supplementary material

Supplementary data associated with this article can be found, in the online version, at https://doi.org/10.1016/j.optlastec.2019.105965.

References

[1] M.G. Figueiro, B. Steverson, J. Heerwagen, K. Kampschroer, C.M. Hunter, K. Gonzales, B. Plitnick, M.S. Rea, The impact of daytime light exposures on sleep and mood in office workers, Sleep Health 3 (2017) 204–215, https://doi.org/10.1016/j.sleh.2017.03.005.

[2] M.B.C. Aries, M.P.J. Aarts, J. van Hoof, Daylight and health: a review of the evidence and consequences for the built environment, Light Res. Technol. 47 (2013) 6–27, https://doi.org/10.1177/1477153513509258.

[3] S.H.A. Begemann, G.J. van den Beld, A.D. Tenner, Daylight, artificial light and people in an office environment, overview of visual and biological responses, Int. J. Ind. Ergon. 20 (1997) 231–239, https://doi.org/10.1016/S0169-8141(96)00053-4.

[4] O. Howlett, L. Heschong, L. McHugh, Scoping study for daylight metrics from luminance maps, LEUKOS 3 (2013) 201–215, https://doi.org/10.1582/LEUKOS.2007.03.03.003.

[5] J.B. O'Hagan, M. Khazova, L.L.A. Price, Low-energy light bulbs, computers, tablets and the blue light hazard, Eye 30 (2016) 230–233, https://doi.org/10.1038/eye.2015.261.

[6] W.O. Popoola, Impact of VLC on light emission quality of white LEDs, J. Light. Technol. 34 (2016) 2526–2532, https://doi.org/10.1109/JLT.2016.2542110.

[7] L. Sahin, M.G. Figueiro, Alerting effects of short-wavelength (blue) and long-wavelength (red) lights in the afternoon, Physiol. Behav. 116 (2013) 1–7, https://doi.org/10.1016/j.physbeh.2013.03.014.

[8] M.A. Bonmati-Carrion, K. Hild, V. Isherwood, S.J. Sweeney, V.L. Revell, J.A. Madrid, M.A. Rol, D.J. Skene, Effect of single and combined monochromatic light on the human pupillary light response, Front. Neurol. 9 (2018) 1–15, https://doi.org/10.3389/fneur.2018.01019.

[9] Scientific Committee on Emerging and Newly Identified Health Risks, Health Effects of Artificial Light; 2012. http://ec.europa.eu/health/scientific_committees/emerging/docs/scenihr_o_035.pdf [accessed 21 Dec 2018].

[10] J.P. Hanifin, S.W. Lockley, K. Cecil, K. West, M. Jablonski, B. Warfield, M. James, M. Ayers, B. Byrne, E. Gerner, C. Pineda, M. Rollag, G.C. Brainard, Randomized trial of polychromatic blue-enriched light for circadian phase shifting, melatonin suppression, and alerting responses, Physiol. Behav. 198 (2019) 57–66, https://doi.org/10.1016/j.physbeh.2018.10.004.

[11] R.M. Lunn, D.E. Blask, A.N. Coogan, M.G. Figueiro, M.R. Gorman, J.E. Hall, J. Hansen, R.J. Nelson, S. Panda, M.H. Smolensky, R.G. Stevens, F.W. Turek, R. Vermeulen, T. Carreon, C.C. Caruso, C.C. Lawson, K.A. Thayer, M.J. Twery, A.D. Ewens, S.C. Garner, P.J. Schwingl, W.A. Boyd, Health consequences of electric lighting practices in the modernworld: a report on the National Toxicology Program's workshop on shift work at night, artificial light at night, and circadian disruption, Sci. Total Environ. 607–608 (2017) 1073–1084, https://doi.org/10.1016/j.scitotenv.2017.07.056.

[12] V. Benard, B. Etain, G. Vaiva, C. Boudebesse, S. Yeim, C. Benizri, H. Brochard, F. Bellivier, P.A. Geoffroy, Sleep and circadian rhythms as possible trait markers of suicide attempt in bipolar disorders: an actigraphy study, J. Affect. Disord. 244 (2019) 1–8, https://doi.org/10.1016/j.jad.2018.09.054.

[13] S. Leppamaki, T. Partonen, I. Vakkuri, J. Lonnqvist, M. Partinen, M. Laudon, Effect of controlled-release melatonin on sleep quality, mood, and quality of life in subjects with seasonal or weather-associated changes in mood and behaviour, Eur. Neuropsychopharmacol. 13 (2003) 137–145, https://doi.org/10.1016/S0924-977X(02)00175-X.

[14] J.J.A. Denissen, L. Butalid, L. Penke, M.A.G. van Aken, The effects of weather on daily mood: a multilevel approach, Emotion 8 (2008) 662–667, https://doi.org/10.1037/a0013497.

[15] M.J.H. Huibers, L.E. de Graaf, F.P.M.L. Peeters, A. Arntz, Does the weather make us sad? Meteorological determinants of mood and depression in the general population, Psychiatry Res. 180 (2010) 143–146, https://doi.org/10.1016/j.psychres.2009.09.016.

[16] T.A. Klimstra, T. Frijns, L. Keijsers, J.J.A. Denissen, Q.A.W. Raaijmakers, M.A.G. van Aken, H.M. Koot, P.A.C. van Lier, W.H.J. Meeus, Come rain or come shine: individual differences in how weather affects mood, Emotion 11 (2011) 1495–1499, https://doi.org/10.1037/a0024649.

[17] R. Kuller, L. Wetterberg, Melatonin, cortisol, EEG, ECG and subjective comfort in healthy humans: impact of two fluorescent lamp types at two light intensities, Light. Res. Technol. 25 (1993) 71–80, https://doi.org/10.1177/096032719302500203.

[18] K. Fujiwara, A. Yano, Controllable spectrum artificial sunlight source system using LEDs with 32 different peak wavelengths of 385–910 nm, Bioelectromagnetics 32 (2010) 243–252, https://doi.org/10.1002/bem.20637.

[19] W. Hertog, A. Llenas, J. Carreras, Optimizing indoor illumination quality and energy efficiency using a spectrally tunable lighting system to augment natural daylight, Opt. Express 23 (2015) A1564–A1574, https://doi.org/10.1364/OE.23.0A1564.

[20] J.-H. Jou, T.-C. Tai, S.-H. Liu, Z.-K. He, C.-L. Chen, S.D. Chavhan, Y.-H. Chen, C.-C. Chen, M.-T. Lee, J.-R. Lee, Pseudo-sunlight organic light-emitting diodes, Opt. Laser Technol. 112 (2019) 494–499, https://doi.org/10.1016/j.optlastec.2018.11.046.

[21] E.F. Schubert, Light-Emitting Diodes, second ed., Cambridge University Press, Cambridge, 2006.

[22] G. Held, Introduction to Light Emitting Diode Technology and Applications, first ed., CRC Press, Boca Raton, 2009.

[23] V.A.G. Rivera, F.A. Ferri, L.A.O. Nunes, E. Marega, White light generation via upconversion and blue tone in Er3+/Tm3+/Yb3+-doped zinc-tellurite glasses, Opt. Mater 67 (2017) 25–31, https://doi.org/10.1016/j.optmat.2017.03.028.

[24] N.D.Q. Anh, T.H.Q. Minh, N.H.K. Nhan, Enhancing lighting performance of white LED lamps by green emitting Ce, Tb phosphor, Adv. Electr. Electron. Eng. 16 (2016) 609–614, https://doi.org/10.15598/aeee.v14i5.1795.

[25] TopLedLight, KW-4RGBW, 2019. http://www.topledlight.com/4W-RGBW-RGB-White-High-Power-LED-Bead-4-Watt-Red-Green-Blue-White-Light_p1945.html (accessed 9 July 2018).

[26] Czech Hydrometeorological Institute, CHMI report no. 7, 2018. http://portal.chmi.cz/files/portal/docs/poboc/OS/zpravodaj/archiv/2018/zpravodaj-1807.pdf (accessed 12 Sept 2018).

[27] LightTools Illumination Design Software, Synopsys, 2019. https://optics.synopsys.com/lighttools/ (accessed 14 January 2019).

[28] R.S. Witte, J.S. Witte, Statistics, ninth ed., Wiley, Hoboken, 2009.

[29] Photometric & Optical Testing, LED Colour Difference Metrics: SDCM & MacAdam Ellipses, 2017. http://www.photometrictesting.co.uk/File/blog_LED_colour_difference.php (accessed 18 Sept 2018).

[30] R.J. Nelson, S. Chbeir, Dark matters: effects of light at night on metabolism, Proc. Nutr. Soc. 77 (2018) 223–229, https://doi.org/10.1017/S0029665118000198.

[31] K. Weissova, J. Skrabalova, K. Skalova, K. Cervena, Z. Bendova, E. Miletinova, J. Koprivova, K. Sonka, D. Dudysova, A. Bartos, J. Buskova, Circadian rhythms of melatonin and peripheral clock gene expression in idiopathic REM sleep behavior disorder, Sleep Med. 52 (2018) 1–6, https://doi.org/10.1016/j.sleep.2018.07.019.

[32] P. Studer, J.M. Brucker, C. Haag, J. van Doren, G.H. Moll, H. Heinrich, O. Kratz, Effects of blue- and red-enriched light on attention and sleep in typically developing adolescents, Physiol. Behav. 199 (2018) 11–19, https://doi.org/10.1016/j.physbeh.2018.10.015.

[33] M. Bauer, T. Glenn, S. Monteith, J.F. Gottlieb, P.S. Ritter, J. Geddes, P.C. Whybrow, The potential influence of LED lighting on mental illness, World J. Biol. Psychiatry 19 (2017) 59–73, https://doi.org/10.1080/15622975.2017.1417639.

[34] Y. Touitou, A. Reinberg, D. Touitou, Association between light at night, melatonin secretion, sleep deprivation, and the internal clock: health impacts and mechanisms of circadian disruption, Life Sci. 173 (2017) 94–106, https://doi.org/10.1016/j.lfs.2017.02.008.

[35] A. Wagdy, A. Sherif, H. Sabry, R. Arafa, I. Mashaly, Daylighting simulation for the configuration of external sun-breakers on south oriented windows of hospital patient rooms under a clear desert sky, Sol. Energy 149 (2017) 164–175, https://doi.org/10.1016/j.solener.2017.04.009.